Non-Contact Ultrasound

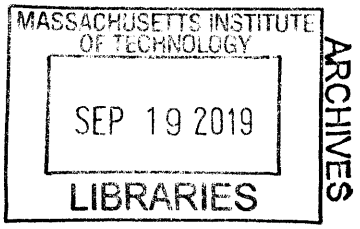

by

Xiang Zhang

B.S. University of Maryland - College Park (2013)
S.M. Massachusetts Institute of Technology (2015)

Submitted to the Department of Mechanical Engineering
in partial fulfillment of the requirements for the degree of

Doctor of Philosophy in Mechanical Engineering

at the

MASSACHUSETTS INSTITUTE OF TECHNOLOGY

September 2019

Signature redacted

Author .....
Department of Mechanical Engineering
July 3, 2019

Signature redacted

Certified by .....
Brian W. Anthony
Principal Research Scientist, Department of Mechanical Engineering
Signature redacted Thesis Supervisor

Accepted by .....
Nicolas Hadjiconstantinou
Graduate Officer, Department of Mechanical Engineering

Non-Contact Ultrasound

by

Xiang Zhang

Submitted to the Department of Mechanical Engineering
on July 3, 2019, in partial fulfillment of the
requirements for the degree of
Doctor of Philosophy in Mechanical Engineering

Abstract

This thesis explores the design, development, and evaluation of two novel non-contact ultrasound imaging methods: immersion ultrasound and optical ultrasound. Immersion ultrasound utilizes traditional piezoelectric elements in a tomographic framework to develop new algorithms and acquisition methods for quantification of tissue geometry and properties in human proximal limbs. Bone is uniquely challenging for ultrasound due to the high impedance mismatch between bone and soft-tissue in the imaging domain. New imaging algorithms are necessary for both geometric and quantitative reconstruction of subjects with bone. Multiple immersion systems were designed and constructed using the framework presented in this thesis. Mechanical systems include a 4 degrees of freedom single element system and a fully flexible 36 degrees of freedom robotic system abbreviated MEDUSA (Mechanically Discrete Ultrasound Scanning Apparatus). An adaptive beamforming algorithm addressing specularity of bone in pulse-echo imaging and a Full Waveform Inversion algorithm for quantitative imaging with bone are discussed, with imaging results on tissue mimicking phantoms, excised animal tissue, and human subjects. Furthermore, a laser ultrasound (LUS) system was developed for full non-contact ultrasound imaging. LUS completely replaces conventional piezoelectric elements for generation and detection of ultrasound in biological tissue. LUS generates ultrasonic waves at the tissue surface via rapid transduction of optical energy to acoustic energy through thermomechanical coupling on the tissue surface and detects returning ultrasonic waves on the tissue surface using laser interferometry. In combination, LUS can utilize any tissue surface as a viable acoustic transmitter or detector. Analysis of light and tissue interactions presented in this thesis identifies the critical process parameters for soft-tissue imaging at eye and skin safe optical exposure levels. LUS system design methods and imaging results on tissue mimicking phantoms, excised tissue, and humans subjects are presented. Human LUS results marks the first instance of full non-contact optical ultrasound imaging of *in-vivo* human subjects. All systems presented in this thesis were calibrated to ensure safe optical and acoustic exposure levels for human subjects. Approval was obtained from the MIT Committee on the Use of Humans as Experimental Subjects (COUHES) prior to any human experimentation.

Thesis Supervisor: Brian W. Anthony
Title: Principal Research Scientist, Department of Mechanical Engineering

Acknowledgments

I would like to thank my advisor Dr. Brian Anthony for his unwavering support and guidance during my time at MIT. Despite changes in projects, funding, or collaborations, Brian has always been supportive of me personally in pursuing my interests while pushing the thesis forward. Brian broadened my research experience by pushing me outside of my area of expertise, while allowing me the freedom to explore and balance my research with my extracurricular interests for a well rounded graduate education.

I would like to thank my committee members Professor Marty Culpepper and Professor Peter So for their time and guidance throughout my thesis research. Marty's feedback was integral in refining the importance and impact of this thesis while Professor So's expertise in optics and imaging supported me through unfamiliar research areas. Furthermore, I'd like to thank Marty for giving me the opportunity to be a mentor at MIT MakerWorkshop, which supported both my research and my passion for hands-on learning.

I would like to thank my colleagues and friends in the Device Realization Lab, in particular, Jonathan Fincke, Gregory Ely, and Bruce Shin for their feedback and acoustics expertise in algorithm development. Jon, who I worked with throughout my time at MIT, was a great teammate that went through the highs a lows of many projects with me. Thank you to Bryan Ranger who provided deeper insights for prosthetic fitting. Thank you to Robert Haupt, Chuck Wynn, and Matthew Johnson from MIT Lincoln Labs who provided funding and hardware resources for the laser ultrasound research.

I would like to thank my friends, family, and the MIT community: Rebecca Zubajlo, for her support throughout my PhD both in and out of lab; the MIT Hyperloop team, for the experience and camaraderie in tackling a monumental engineering challenge; and the MIT MakerWorkshop, for building and being a part of a broad community of makers and tinkerers at MIT. Lastly, thank you to my parents for supporting and motivating me to push myself forward beyond what I thought I could achieve.

Contents

List of Figures

List of Tables

Chapter 1

Introduction

Globally, the annual medical imaging device market totals $34.1 billion [3]. The breakdown of the market for each imaging modality is shown in Figure 1-1. Ultrasound is the second largest segment, consisting of 20% of the total, only second to X-ray imaging. In comparison, the primary application of ultrasound is for soft-tissue imaging, while X-ray imaging is focused on bone. For soft-tissue, applicable imaging methods are predominately ultrasound (US), computed tomography (CT), and magnetic resonance imaging (MRI).

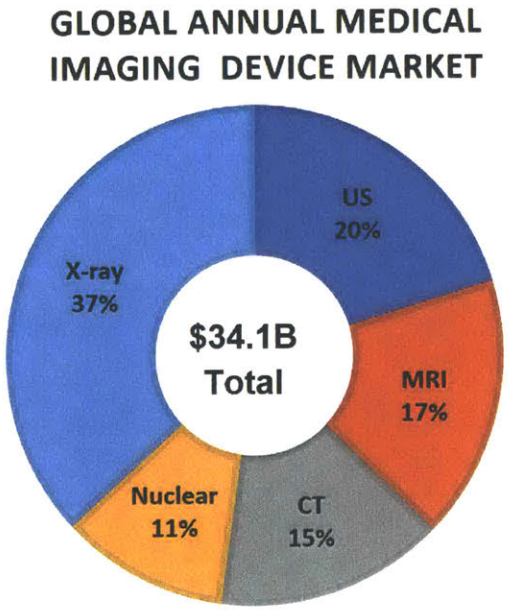

Figure 1-1: Global annual medical imaging device market

1.1 Medical Ultrasound

Presently, medical ultrasound is the most extensively used imaging modality for soft-tissue imaging. Preferred over other imaging modalities (X-ray, MRI, CT) for its non-ionizing physics, lower costs, and portability; use of medical ultrasound has grown by more than an order or magnitude over the last decade [4]. Recent reports have shown that diagnostic imaging is one of the main contributors to total healthcare costs in the U.S.[5]. Comparing US, MRI, and CT in Table 1.1, the total healthcare burden in the U.S. for diagnostic imaging is comparable between the three soft-tissue imaging modalities. However, ultrasound has an order of magnitude higher patient throughput, with lower costs and broader accessibility [4].

	Ultrasound	MRI	CT
Annual Device Market	\$6.9B	\$5.8B	\$5.1B
Cost per scan (U.S.)	\$100-300	~\$2000	\$800-1200
Annual number of scans	445M	39M	81M
Annual healthcare cost	\$89B	\$78B	\$81B
Contrandication	None	No metals	Radiation
Real-time Imaging	Yes	No	No
Accessibility	High	Low	Low
Portability	High	None	None

Table 1.1: Comparison of soft-tissue imaging modalities

In the U.S., MRI and CT are an order of magnitude more expensive than ultrasound but with an order of magnitude lower patient throughput. There is significant cost saving opportunities if ultrasound can replace MRI or CT for feasible diagnostic imaging applications.

1.1.1 Case Study - Musculoskeletal Imaging

Specifically for musculoskeletal (MSK) imaging, there is significant interest in replacing diagnostic MRI with ultrasound [6,7]. In the U.S., annual healthcare burden due to musculoskeletal diseases was estimated to be up to \$850 billion, 8% of the U.S. GDP [7]. Medical imaging can be up to 50% of the overhead in these healthcare costs [8]. Typically, patients will undergo multiple imaging instances for diagnosis or

post operation follow-up. In MSK imaging, there is significant interest in substituting MRI with ultrasound for diagnosis. To quantify possible cot savigns, Parker *et al.* compared diagnostic outcomes using ultrasound against those of MRI in multiple body regions, summarized findings are tabulated in Table 1.2 [6].

Body Part	Cases per Year	% Substitute	Savings (M)
Wrist/hand	294	77.2	\$101.5
Elbow	99	56.6	\$25.1
Ankle/foot	669	40.1	\$120.0
Shoulder	878	37.7	\$148.1
Lower extremity	109	31.2	\$15.2
Upper extremity	19	21.1	\$1.8
Hip	218	18.8	\$18.3
Knee	1335	10.9	\$65.1
Total	3621	30.6	\$495.2

Table 1.2: Substitution of MRI with ultrasound for MSK imaging

Parker *et al.* quantified the number of cases for which the primary and secondary diagnostic outcomes using ultrasound were in agreement with those using MRI. The cost savings were calculated using the average healthcare reimbursements reported by healthcare providers for each exam type [6, 8]. Parker *et al.* concluded that a 1% substitution of MRI for ultrasound in MSK imaging can save approximately \$16.2 million annually. In aggregate, ~\$500 million in healthcare expenditure can be saved annually if all feasible substitutions are made [6]. However, more detailed evaluation of ultrasound and MRI in the context of current healthcare profit and cost models must be made to determine more accurate savings estimates. For-profit over-prescription of drugs and diagnostics has been attributed to the rising healthcare costs in the U.S. [5]. While replacing MRI diagnostics with ultrasound has significant cost saving potential and expands diagnostic accessibility, care must be taken to avoid over-prescription.

1.2 Ultrasound Basics

Current embodiments of ultrasound technology range from cart-based bedside systems to portable hand held devices [4]. Conventional medical ultrasound requires placement of a piezoelectric element or an array of elements in contact with the patient to transmit and detect acoustic waves in the tissue. As the transmitted waves interact with tissue, varying tissue features generate echoes that are detected by the acoustic transducers. The generated echoes encode information about the tissue through which it has propagated; with sufficient sensing and computation, parameters about the tissue can be extracted from the spatial and temporal signature of the detected acoustic signals. The transmitting and receiving element may be the same physical element (pulse-echo/mono-static) or different elements (bi-static). Different transmit/receive configurations can capture different information about the tissue. Configuring the transmit and receive patterns is known as beamforming. Optimizing beamforming techniques to maximize image quality in each imaging application is an active research area [4]. A basic schematic of ultrasound propagation is shown in Figure 1-2, with typical fetal B-mode imaging results.

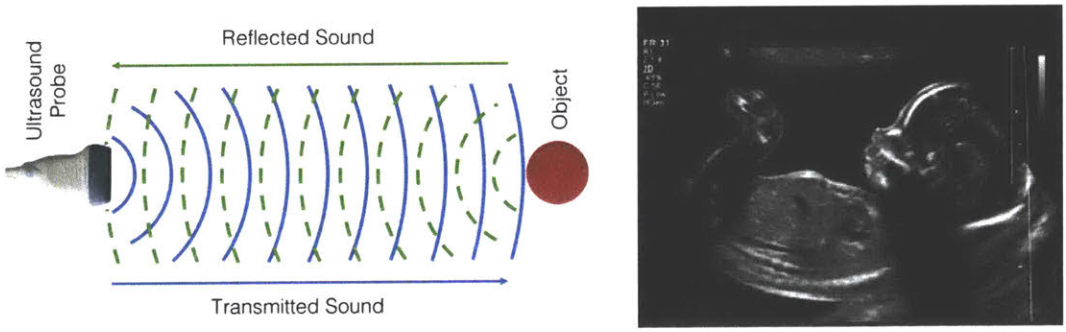

(a) Basic ultrasound

(b) Fetal B-mode image

Figure 1-2: Basic operation of conventional ultrasound

With advances in microelectronics and increases in computational power, modern ultrasound systems are able of generating real-time, quantitative, and 3D images. Imaging results using shear wave elastography, color flow Doppler, 3D fetal imaging, and cardiac motion imaging (M-mode) are shown in Figure 1-3.

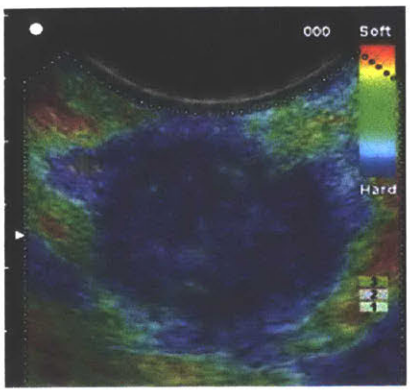

(a) Shear wave elastography

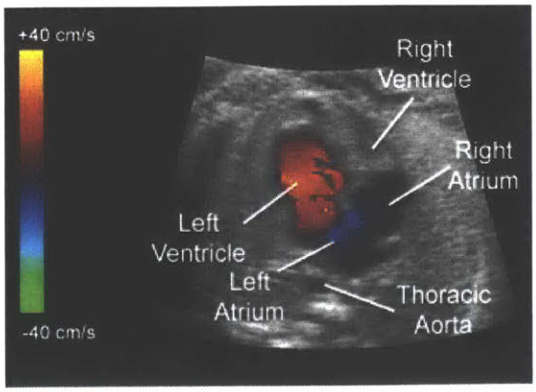

(b) Color Doppler

(c) Fetal 3D

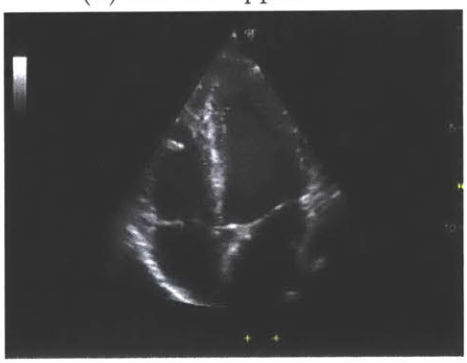

(d) Cardiac M-mode

Figure 1-3: Various ultrasound imaging modes

Shear wave elastography, shown in Figure 1-3a, quantifies tissue stiffness by measuring the spatial propagation speed of shear waves ($\sim$1-3 m/s) in the tissue, which is much slower than the longitudinal waves ($\sim$1500 m/s). Typically, a mechanical push pulse (a spatially focused acoustic pulse) is used to generate the shear wave; mechanical palpation device can also be used. As the shear wave propagates, pulses of longitudinal waves tracks the movements of the shear wave by measuring echoes from traveling shear wave. Shear wave speed correlated with tissue elasticity, thus the imaging technique is named shear wave elastography. In Figure 1-3a, areas of faster shear wave speed are in blue (higher stiffness) while areas of lower shear wave speed are in red (lower stiffness). In color Doppler, shown in 1-3b, blood flow velocity is quantified by measuring the Doppler shift of the transmit signal. Blood flow moving toward or away from the direction of wave propagation generates time or phase shifts proportional to the flow velocity. In practice, commercial system use

pulse-wave-Doppler to generate spatially resolved Doppler images. Unlike continuous wave (CW) Doppler which has no range resolution; in pulse-wave-Doppler, a series of pulses are transmitted at known time intervals and the reflected (Doppler shifted) pulses are quantified against the known transmit pulses to quantify flow velocity with discretized range resolution. For 3D ultrasound imaging, shown in Figure 1-3c, a 2D ultrasound array or a mechanically scanned linear array is used to generate the 3D image. 2D arrays captures true 3D acoustic propagation but is expensive due to the high number of piezoelectric elements in the array and the corresponding transmit and receive electronics. To save cost, a mechanically scanned linear array captures multiple 2D B-mode slices and stitches the data in post processing to generate a 3D image. Lastly, motion ultrasound (M-mode), shown in Figure 1-3d, is simply tracking moving features in a B-mode image. If a transducer is held stationary, pixel motion can be tracked in the B-mode image to generate a time vs position waveform, typically used when estimating heart motions.

1.3 Current Ultrasound Challenges

In comparison to other medical imaging modalities, patient contact is a unique requirement specific to ultrasound. During an ultrasound scan, the sonographer is in the imaging loop as shown in Figure 1-4. The acquired image is subject to manipulation (position and applied load) of the probe by the clinician during imaging.

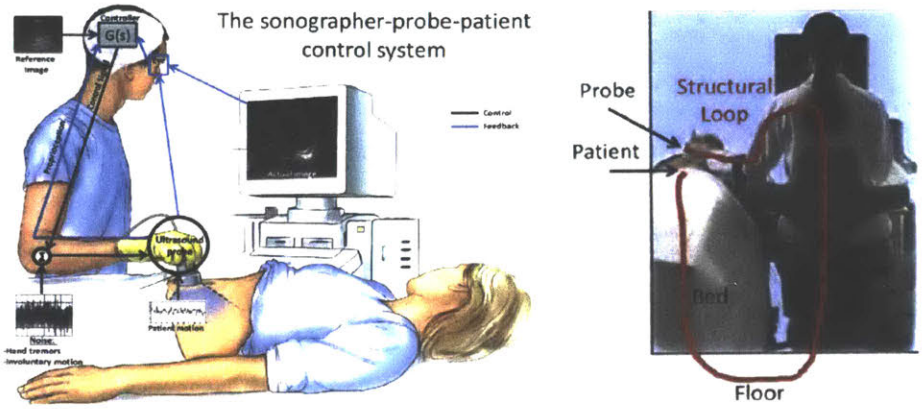

Figure 1-4: Typical ultrasound exam and the structural loop that includes the sonographer.

Patient contact gives rise to ultrasound image variability and is the dominant cause of work-related musculoskeletal disorder (WRMSD) [9–13]. Furthermore, the freehand reference frame, the cross-sectional nature of conventional ultrasound also generates orientation sensitive images. While sonographers have visual feedback to orient the probe and obtain the desired cross-sectional image, there is no feedback on the contact force. Orientation and contact force induced image variability restrict longitudinal tracking (monitoring over time) of tissue morphology using ultrasound [14–16]. In comparison, MRI and CT have gantry fixed reference frames and generates volumetric images without patient contact. However, frequent imaging for continuous patient monitoring using MRI or CT is prohibitively expensive or would expose patients to significant ionizing radiation. To the best of the author's knowledge, there is currently no FDA approved ultrasound based method for tracking tissue change or disease progression.

Image variability in ultrasound — Sonographers consecutively imaging the

same region of interest on the same patient generates different images due to variability in probe positioning/orientation and probe-patient contact forces. As shown in Figure 1-5, US imaging of the same location generates different images depending on the applied contact force [16–18]. Gilbertson reported contact forces up to 36.5 N during abdominal exams during 53 imaging instances; the average force was 8.3 N with standard deviation of 4.2 N [17]. Based on literature, a compressive force of 0.5 to 5 N can compresses abdominal tissue between 1 to 10 mm [16, 19]. To a first order approximation, soft-tissue bulk stiffness can be estimated as $\sim 0.5\ N/mm$. Functional change in muscle quality exists for 0.3-0.5 mm changes in muscle thickness [14]. Quantifying and tracking muscle morphology over time would require control of the contact force within 0.5 N, well beyond the physical control capabilities of any human operator. Tracking of muscle quality requires active force control during imaging or complete removal of tissue contact [17]. Furthermore, biological tissue exhibits strain-stiffening non-linear behavior as it is compressed. Quantitative methods measuring tissue elasticity such as shear wave elastography has been shown to be directly sensitive to the amount tissue compression [20–22]. As shown in Figure 1-6, measure of tissue elasticity from shear wave elastography is dependent on the applied contact force [17, 18].

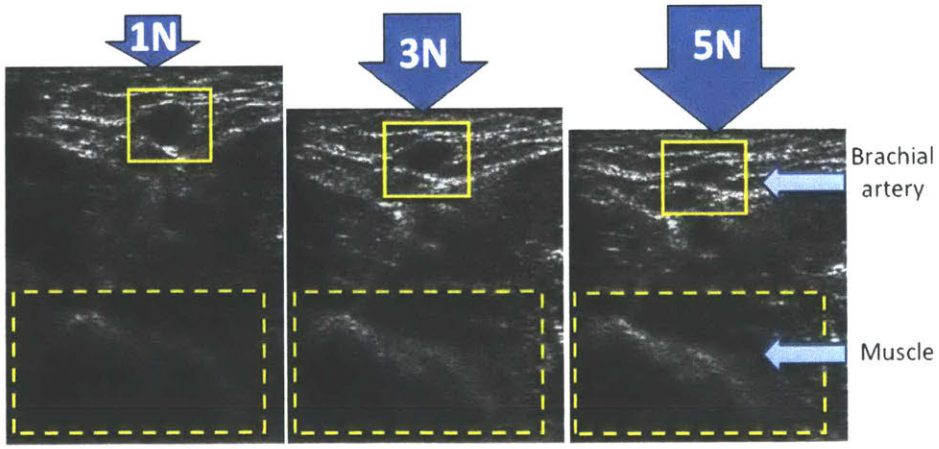

Figure 1-5: Ultrasound image variability

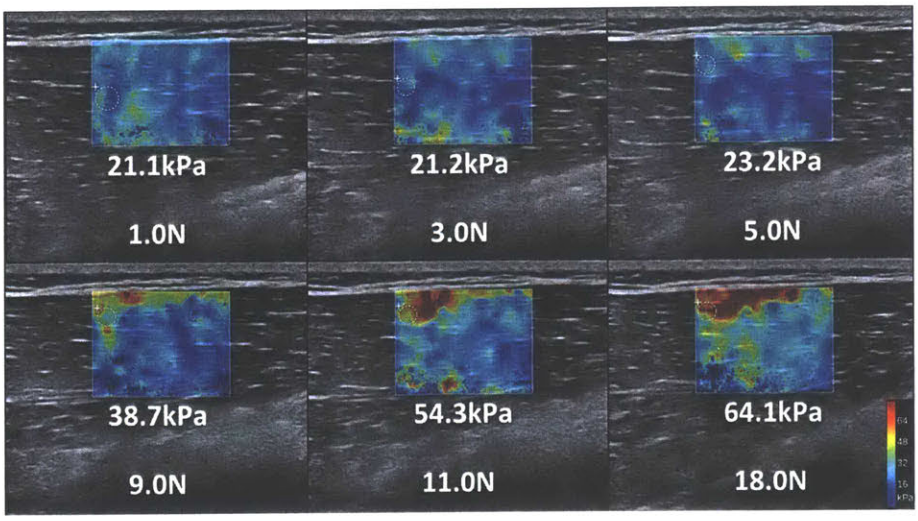

Figure 1-6: Elastography variability due to compression force

Sonographer Injury — As of 2016, there were 122,300 sonographers in the U.S. and the occupation is predicted to increase 17% over the following decade (much faster than average) as the baby-boom population ages and the need for diagnostic medical imaging increases [11]. Practicing sonographers are at significant risk for WRMSD with reported incidence up to 90%; one out of five sonographers will experience a career-ending injury within 5 years of practice [9, 23]. WRMSD has been attributed to physical manipulation of the ultrasound probe during imaging and poor exam room ergonomics [9, 10, 12, 13, 23–25]. If patient contact could be eliminated from ultrasound imaging, WRMSD for sonographers could be significantly reduced.

1.3.1 Prior Solutions

Recent research to account for variability in acquisition have be focused on instrumenting clinical ultrasound probes such as: adding camera and Simultaneous Localization and Mapping (SLAM) algorithms for repeatable probe positioning, or measuring and regulating probe contact forces during imaging [17, 26–28]. While compact, these add-on devices only quantify the variability between imaging instances rather than removing the source of image variability - the patient contact. MRI and CT enable large area quantitative imaging by providing a known spatial reference point on the gantry, thus, removing patient contact and the operator from the imaging loop.

With a known fixed reference frame, quantitative physiological parameters within the target can be extracted from the imaging sequence in MRI and CT. These methodologies enable CT and MRI to reliably track and image large tissue volumes to monitor tissue morphology over time. By removing patient contact, ultrasound image variability induced by tissue compression and probe orientation can be eliminated, greatly expanding the usability of ultrasound for broader clinical applications. For the two non-contact ultrasound methods explored in this thesis: immersion and optical; the proposed clinical applications are identified in the following sections.

1.4 Immersion Ultrasound

Immersion ultrasound systems emulates MRI and CT by establishing a fixed reference frame on a gantry. Immersion ultrasound systems typically consist of ultrasonic transducers positioned around an imaging target. The imaging target and transducers are both immersed in a fluid tank (typically water) to acoustically couple the transducer to the imaging target without physical contact. All transducer locations are known relative to the gantry, enabling reconstruction of the image target using a fixed reference frame. Immersion systems eliminates contact and removes the operator from the imaging loop. Prior work implementing the immersion system framework have primarily focused on breast cancer detection using ultrasound [29–39]. These breast imaging systems circumferentially surround an imaging target and implement ultrasound tomography (UST) to quantitatively differentiate regions of high and low tissue stiffness to identify cancerous tissue. UST systems have produced images comparable to those of MRI or CT and is a significant step forward in quantitative ultrasound imaging [38–40]. Clinically, there is interest in extending ultrasound toward quantitative musculoskeletal imaging to reduce cost, improve longitudinal tracking, and enable volumetric imaging [41, 42]. While UST results are promising in soft-tissue imaging, new systems and algorithms are necessary for musculoskeletal imaging due to the presence of bone.

Using ultrasound to image bone and the surrounding tissue results in strong re-

fraction, attenuation, and scattering of the transmitted acoustic waves. Typical assumptions made in soft-tissue imaging do not hold with the presence of bone. In this regard, imaging of soft-tissue with bone presents an new set of challenges and applications [43–45]. Accurate quantitative characterization of bone and surrounding soft-tissues has potential in several motivating clinical needs: (1) improve prosthetic fittings by integrating internal tissue and bone structural information into the socket design process [46,47], (2) monitor bone density deterioration for osteoporosis progression and diagnosis [48–59], and (3) better quantify neuromuscular disease progression such as Duchenne's muscular dystrophy [60,61].

1.4.1 Clinical Application of Immersion Ultrasound

Prosthetic Fitting — The current plaster casting method for prosthetic fitting is a largely subjective process [47,62]. Typical fittings require several iteration to achieve a desirable fit. Improper fittings at the limb-socket interface can cause neuromas, inflammation, soft-tissue calcifications, and pressure sores [47,62]. Any of these pain inducing pathologies can force the wearer into a wheelchair or crutches, reducing their mobility and quality of life. The prosthetic fitting challenge hinges on the identification of properties within the residual limb. A system capable of quantifying soft-tissue and bone properties, with integration into a prosthetic CAD modeling system, will substantially improve the socket design process [47,63]. MRI and CT of residual limbs have been used to design personalized prosthetic sockets for lower limb amputees [47]. However, both MRI and CT require large dedicated clinical spaces and are prohibitively expensive for most prosthetic clinics, thus, there is significant interest to leverage ultrasound for prosthetic design [46,47,62,64–66].

Bone Mineral Density Monitoring — Osteoporosis (a condition under which the bone mineral density (BMD) is substantially reduced) is a condition affecting a significant part (>50% in the US) of the population aged 50 and above [67]. Osteoporosis greatly increases the risk of fractures, which can be particularly debilitating for the elderly. Early diagnosis, quantitative measurement, and monitoring are important

to manage the progression of the condition, but also to assess the efficacy of new treatments. Currently, X-ray is the predominant imaging modality for such diagnosis and monitoring. However, it is estimated that one must lose ~30% of BMD to be noted on X-rays [67]. A more sensitive testing modality could provide earlier osteoporosis diagnosis and improve BMD measurement accuracy. The clinical potential of ultrasound to study bone fractures was first explored for monitoring of fracture healing [68]. Variation in the transmission of ultrasound through the heel can be used to classify patients with and without osteoporosis [48]. Immersion ultrasound imaging through a distal limb could be used to map the speed of sound and attenuation inside the bone, providing a richer set of measurements of bone mineral density.

Muscle Deterioration Monitoring — Characterized by progressive disability leading to death, Duchenne muscular dystrophy (DMD) remains one of the most common and devastating neuromuscular disorders of childhood [69]. It is caused by a genetic mutation which generates a complex sequence of events in muscle cells which eventually undergo fibrosis and are replaced by adipose and connective tissue. Average survival of DMD patients is to the age of 25, although in some cases patients have survived into their forties. Though a variety of promising new treatment strategies are in development, quantitative measures for clinical trials outcomes remain limited. Presently, functional measures such as the six-minute walk test - where a child is evaluated based on ambulatory capabilities - is the standard to track disease progression and treatment effectiveness [60]. While clearly useful, such tests are impacted by unrelated factors, such as mood and effort, and have limited repeatability. To address this and other limitations, MRI is now being investigated as a surrogate measure. Comparing to MRI, a more cost-effective and portable surrogate measure that provides high repeatability and sensitivity while strongly correlating to disease status would find broad use in Phase II and possibly in Phase III clinical trials for DMD. A ultrasound system capable of providing quantitative measurements of the muscle deterioration can serve as a convenient and non-invasive method to track DMD disease progression that surpasses the functional measures currently in use.

1.5 Laser Ultrasound

Laser ultrasound (LUS) aims to completely replace conventional piezoelectric elements with light. Traditionally, piezoelectric elements are brought in contact with the target surface with a coupling agent (gel or water) to generate and detect acoustic signals. However, both the generation and detection of acoustic signals can be achieved respectively by the photoacoustic effect and laser interferometry. The photoacoustic effect converts optical energy to acoustic energy via thermomechanical coupling within the irradiated target [70]. Typically, a pulsed laser source hits a target which absorbs the pulse of optical energy and rapidly heats and expands. The rapid mechanical expansion and relaxation generates an acoustic source within the target which can be used to acoustically image the target. In combination with optical detection of the transmitted acoustic wave, any target can be remotely imaged optically. A fully optical ultrasound system eliminates traditional piezoelectric transducers and is fully non-contact and coupling agent free. LUS could be a replacement of conventional ultrasound. Previously mentioned clinical applications for immersion ultrasound are also applicable for LUS. In addition, a fully optical non-contact ultrasound system is also clinically applicable for remote patient or neonatal monitoring and contact sensitive applications such as intraoperative imaging and imaging of sensitive/painful tissue regions. Removal of tissue contact using LUS reduces WRMSD risk for sonographers and removal of ultrasound gel eliminates infection risk while imaging sensitive areas.

1.6 Thesis Scope

This thesis explores methods to remove patient contact from ultrasound imaging. Two proposed methods are presented here: immersion systems - using conventional ultrasonic components in a fixed frame gantry system - and laser ultrasound - removing patient contact by using optical methods to induce and detect ultrasound on the tissue surface. Immersion systems are presented in Chapter 2 to 3 and laser ultra-

sound is presented in Chapter 4 to 6. Relevant prior art, system design, and imaging results are presented on each proposed method within the respective chapters.

Chapter 2

Immersion Ultrasound

Unlike soft-tissue imaging of the breast, limb imaging gives rise to complex propagation modes, mode conversion, and multiple paths due to the presence of bone [4]. At typical medical ultrasound frequencies (1-5 MHz), bones cause shadowing within the image. However, transmission of ultrasound through the bone is possible at lower frequencies (0.5-1 MHz) and have been used to classify patients with and without osteoporosis in the heel [48]. However, full quantitative limb imaging using ultrasound has not been presented. To develop a UST system for volumetric limb imaging, innovations in both hardware and software are necessary. Novel scanning systems are needed, including custom transducers, mechanical positioning structures, and data acquisition setups. The scanning system must be capable of recording both reflected and transmitted waves inside the appropriate scan volume. New algorithms accounting for the complex propagation of sound waves in bone are necessary to accurately reconstruct captured data. The developed hardware must be sufficiently flexible to support rapid and iterative development of various complex algorithms and support use of various transducers.

2.1 Soft Tissue Ultrasound Tomography Systems

The kinematics of current ultrasound tomography (UST) systems for soft-tissue imaging vary greatly in their respective transducer architectures. Transducer architectures include: ring arrays, conical arrays, and array probes with reflectors [1, 37, 71].

2.1.1 Ring Arrays

Ring transducer systems typically consists of a rigid ring transducer (256-2048 elements) scanning in one axis along the target, reconstructing 2D slices of the object. Such systems were the first to demonstrate clinically relevant data and obtain FDA approval for quantitative breasting imaging using ultrasound [37]. The first Computed Ultrasound Risk Evaluation prototype (CURE) developed by Duric *et al.* used a 20 *cm* diameter ring transducer consisting of 256 elements [37]. The system produced compounded breast ultrasound images of quality rivaling those of MRI [39]. A denser ring transducer (15 *cm* 2048 elements) system was designed by Waag and Fedewa, but has not been used for clinical imaging [71]. The two systems shown in Figure 2-1, enable reflective imaging with attenuation and sound speed mapping within the circular aperture. Due to the high number of transducers, complex data acquisition (DAQ) hardware is necessary for parallel sampling of the numerous receive channels. Custom sampling and multiplexing hardware were developed for each scan system. Custom ring transducers are costly when compared to commercial hand held probes and are not easily exchangeable.

Ring transducers provide great image quality within the horizontal (in-plane) circular aperture (Figure 2-1c), but the slice thickness (out-of-plane) is limited (12 *mm* in the CURE system) [37]. The difference in in-plane and out-of-plane resolution creates an anisotropic voxel sizes in the volumetric reconstructions, limiting imaging to coronal breast slices.

(a) CURE system by Duric *et al.* [37].

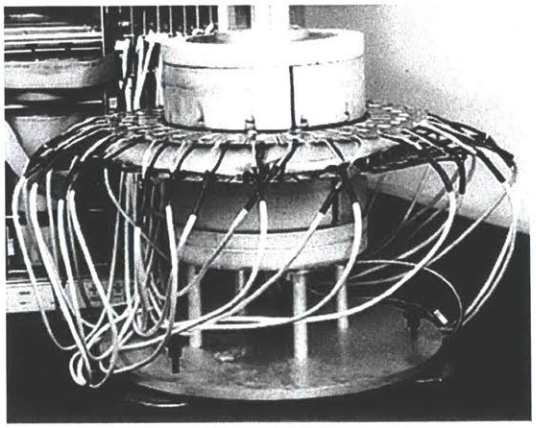

(b) Ring array system by Waag and Fedewa [71].

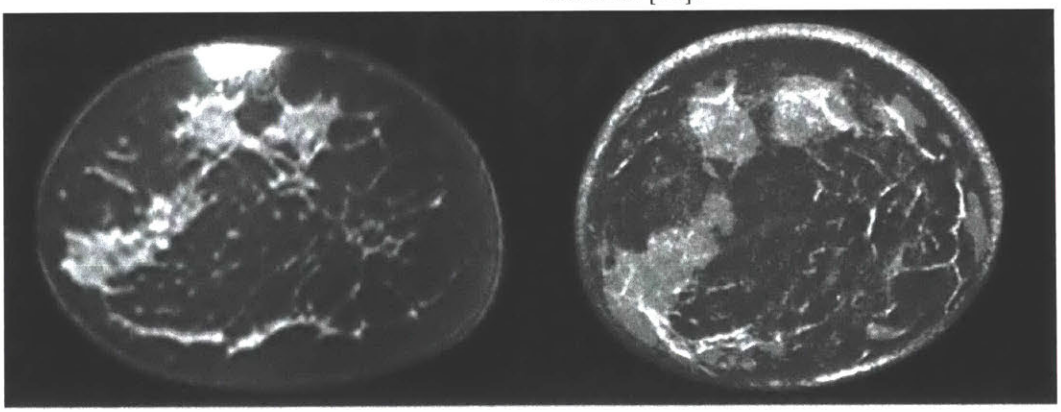

(c) Coronal breast slice from MRI (left) compared to compounded UST slice (right) [37].

Figure 2-1: Ring array UST systems and images with comparison to MRI

2.1.2 Conical Arrays

To correct the anisotropic resolution in ring transducer systems and enable non-sliced 3D tomography, a conical array system for breast imaging was developed by Hopp *et al.* [40]. The conical system consist of 628 transmitters and 1413 receivers forming a 26 *cm* diameter 18 *cm* height semi-ellipsoidal aperture around the breast. Producing up to 80GB of data per scan on a FPGA-based sampling system, reflection, attenuation, and sound speed mapping is possible in spherical 3D coordinates [40]. The conical array is shown in Figure 2-2a.

(a) Conical transducer array

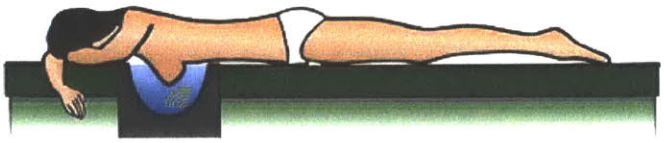

(b) Conical array system by Hopp *et al.* [40].

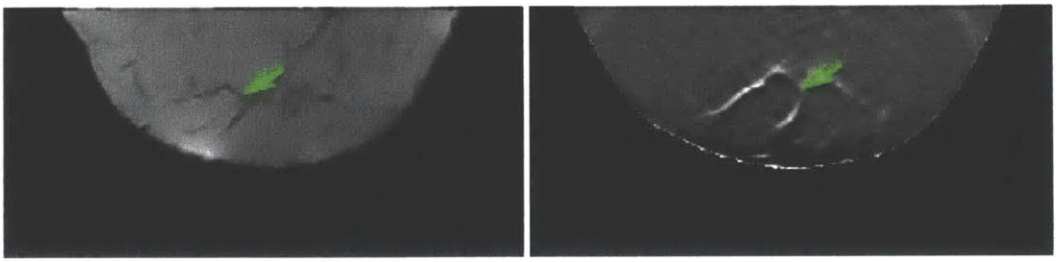

(c) Sagittal breast slice from MRI image (left) with comparison to compounded UST image from the conical array [40].

Figure 2-2: Conical array UST systems and images with comparison to MRI

With out of plane receivers, the conical array system can produce isotropic voxels in volumetric imaging. This enables extraction of transverse and sagittal slices shown in Figure 2-2c, which is not possible in ring array systems. Relative to ring transducers, conical arrays have significantly more transducer elements. Data acquisition and processing systems for the conical array are as complex, if not more complex, than the systems for ring arrays, but recent implementation of FPGAs and GPU processing has helped improve data throughput and processing [72]. The manufac-

turing complexity and cost of a conical array does not enable geometric flexibility in the system. Despite the transducer density, both the ring and conical arrays are still undersampling the slice or volume, respectively [73].

2.1.3 Array Probe Scanner

Mechanical scanning with an array probe provides added system flexibility at the cost of scanning speed. Mechanical scanning with commercial array probes has been used for boundary detection for improving prosthetic fittings [46]. Commercially available probes do not support tomographic scanning and require an additional receiver to capture transmission data. Hansen *et al.* bypassed this limitation by adding an acoustic mirror opposing the transmitter [1]. Shown in Figure 2-3, the stainless steel acoustic mirror reflects the incident wave back to the transmitter, providing through transmission data without an opposing receiver. Ray tracing based on the arrival time of the reflected wave enables sound speed and attenuation mapping within the image slice. Images (Figure 2-4) are produced on the reflector system with as few as 3 insonifying angles (60°, 140°, 260°). Higher quality images are produced with 36 insonifying angles at 10° increments at multiple heights (Figure 2-5) [29].

The reflector tomography system suffers from the same slice thickness limitation as with the ring transducer system. The inability to capture off angle reflections limits imaging to coronal breast slices. From the cost perspective, commercial ultrasound probe and system costs ~$5,000-$10,000 per probe and ~$100,000 to ~$250,000 per system. Though likely cheaper than custom ring array or conical array systems (pricing unavailable) $10,000 to exchange a transducer for testing and development is still non-trivial.

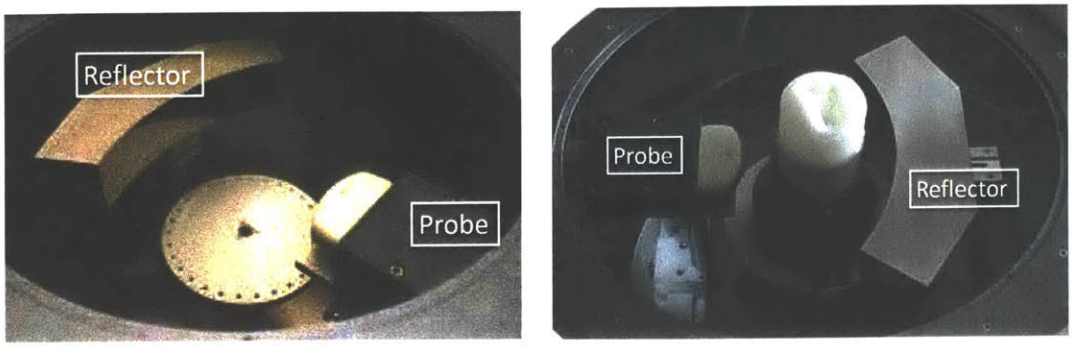

(a) Array probe with mirror (b) System with phantom target

Figure 2-3: Reflection tomography system [1]

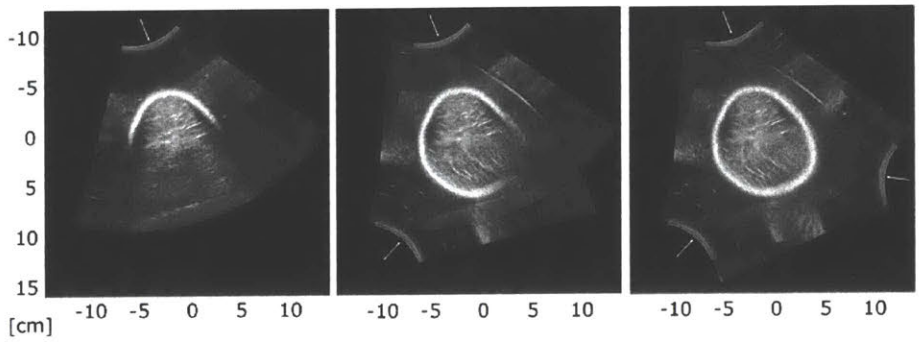

Figure 2-4: Reflection tomography at 60°, 140°, 260° views

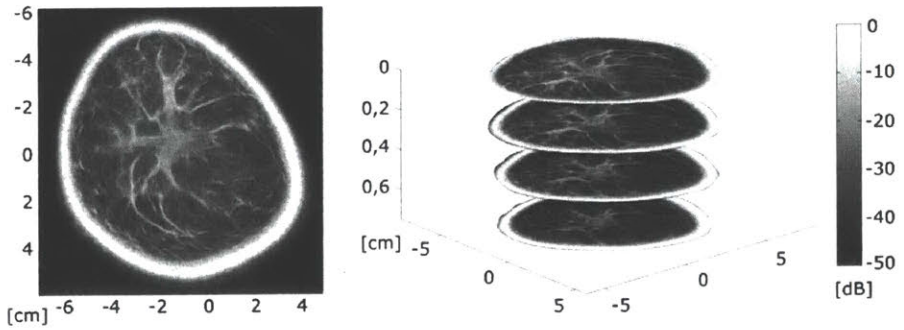

Figure 2-5: Single 36 angle compounded reflection tomography image (left) and compounded slices at multiple heights (right)

2.2 Designing UST for Limb Imaging

For iterative algorithm development, a flexible UST system architecture is required. The system should provide exchangeable transducer configurations (frequency/beam geometry) in conjunction with arbitrary transducer positioning to support novel reconstruction methods. With high production cost and system complexity, ring and conical arrays are unsuitable for iterative development. Array probes do provide more flexibility but is still costly per probe exchange and data acquisition flexibility is dependent on the corresponding imaging system. To understand the landscape of existing ultrasound technology to design a new limb imaging system, a survey of existing ultrasound technology ranging from single element non-destructive testing (NDT) systems to fully populated hemispherical arrays is presented in Figure 2-6.

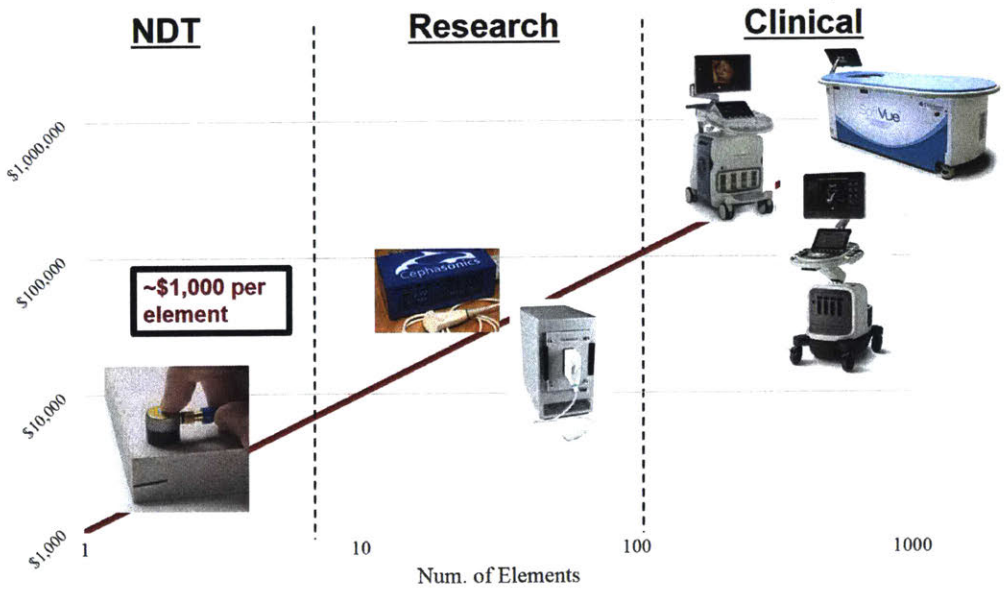

Figure 2-6: Cost of various ultrasound systems against the number of independent transducer channels.

The product space of current ultrasound devices range from single element systems used for NDT to the UST systems mentioned in Section 2.1. In industrial NDT systems, the single element probe transmits and receives an acoustic wave and performs a binary fault detection from the presence of echos (from cracks or voids) within the scan subject, typically for welds or material verification. The probe is moved across

the measurement area by the operator to find faults in the region. NDT systems are generally compact and portable, costing from ~$1,000-$10,000 depending on the level of sophistication in data processing and storage. In the next cost tier, research ultrasound systems with programmable operations straddle both NDT and medical imaging uses. These research systems range from ~$30,000-$200,000 depending on the number of transducers channels and the operating frequency. Research systems allow attachment of different transducers depending on the application (NDT/medical); multiplexing transducer channels to accommodate larger arrays is commonplace. Research systems are typically not subject to FDA approval since each programmable setting would require safety verification. The highest tier includes clinical ultrasound systems and ring/conical arrays, costing from ~$200,000 to more than $1,000,000. Clinical ultrasound systems are approved for diagnostic/therapeutic use by the FDA and can have similar number of transducer channels compared to research systems. Cost of FDA approval is passed to the consumer and the rigidity in diagnostic safety restricts the flexibility of clinical systems for research. Commercial system costs for ring array and conical arrays are not publicly available, but extrapolating cost per independent channel from single element to array systems approximates multiple millions.

Plotting each system cost versus the number of elements, an approximation of ~$1,000 per independently sampled transducer element can be deduced. While Figure 2-6 is grossly estimated based on commercial pricing, a linear approximation of cost per independent transducer element is still valid. Furthermore, as the number of transducer elements increases, the feasible subject size being imaged is also increasing. In ultrasound, the necessary transducer coverage is dictated by the characteristic dimension of the scanned subject. Shown in an overlay of Figure 2-7, for NDT, a single trace is sufficient for fault detection. For conventional ultrasound, a linear transducer array is sufficient for a 2D slice. In UST imaging, as the characteristic diameter D of the subject (breast or limb) increases, the necessary transducer coverage scales with D^2. If volumetric imaging is desired, another dimension of scaling must be added. Fully populating the necessary transducer coverage for volumetric imaging with in-

dependent transducer channels would scale costs exponentially as the characteristic diameter of the subject increases.

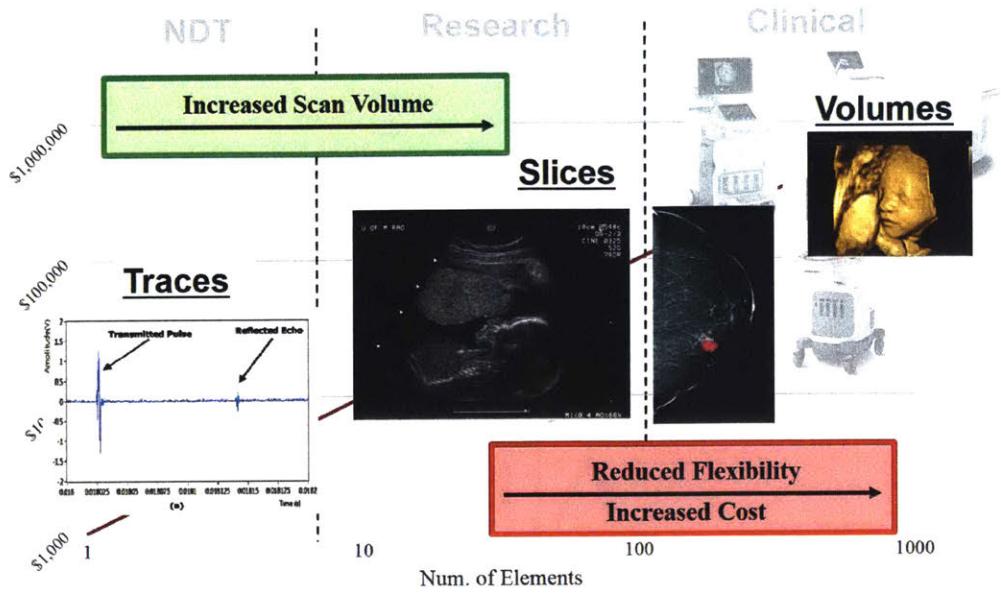

Figure 2-7: Scaling of ultrasound system in subject size against flexibility and cost.

To bypass this exponential cost scaling for volumetric imaging, commercial ultrasound systems implement two approaches: mechanical scanning and multiplexing. Seen in commercial 3D ultrasound probes shown in Figure 2-8, a linear transducer is motorized in the transverse axis to increase coverage without adding more transducers channels.

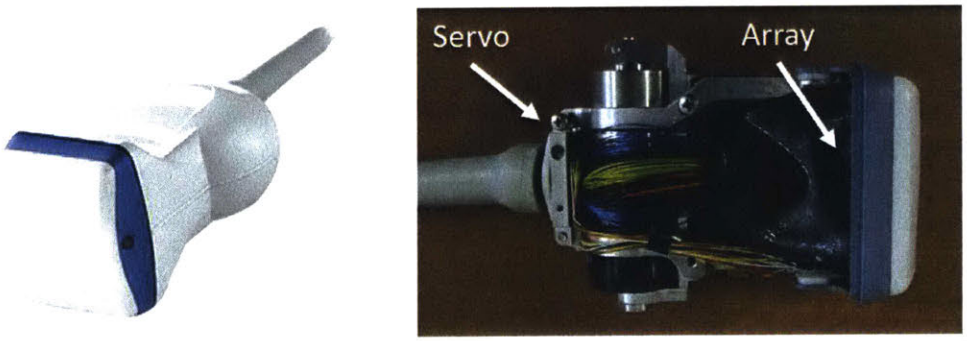

Figure 2-8: 3D ultrasound probe opened to show the mechanical actuation on the array.

Alternatively, multiplexing a single channel to multiple transducer elements is another method of reducing system costs. Multiplexing can be viewed as the electronic

equivalent of mechanically scanning a transducer. Instead of costs associated with motorizing one axis, multiplexing requires physical elements at each scan position. Depending on the size of the target subject and the corresponding required number of transducers, mechanical scanning may be more cost effective than electronic multiplexing, or both are required. The ring array and hemispherical array systems shown in Figure 2-2 both include some mechanical scanning to sufficiently image the target subjects.

As number of transducer elements increases, ultrasound systems also become more application specific. Typical clinical ultrasound systems allow attachment of different probes depending on the type of examination. However, exchanging a ring array or hemispherical array for developmental purposes would be prohibitive costly. For a developmental platform for limb imaging, where tests with variation in transducers, algorithms, and scan apertures is common. Fixed geometry arrays are too restrictive for efficient iterative development. To limit costs and maximize flexibility, a mechanical scanning system using single element transducers was developed.

2.3 Single Element UST

Single element scanning with one transmit and one receive channel is well suited at the developmental stages. Exchangeable transducers and single channel data acquisition significantly reduces cost and system complexity, while maintaining flexibility and low-level control of the system. However, flexibility and simplicity of a single element scanning system sacrifices scanning speed. The transmit and receive transducers must be mechanically placed at each sampling locations around the aperture to complete a scan. Mechanical positioning will always be slower than electronic switching but does allow for custom sampling resolution around the aperture. In reference to prosthetic fitting, as discussed by Mak *et al.* [62], patient movement during a scan heavily affects the resulting image. Motion compensation or tracking may be necessary at lower scanning speeds to correct for patient motion [74].

For algorithm development, a single element system with two independently mov-

ing transducers in a cylindrical reference frame was designed and built, shown in Figure 2-9. Details on the system design and calibration is presented by Zhang in reference [75, 76]. New imaging techniques specifically for limb imaging are presented in the following sections. Pulse-echo imaging on excised bovine shanks using echo flow migration shows dynamic range comparable to clinical ultrasound systems. Tomographic imaging of the same tissue and inversion using Full Waveform Tomography (FWI) quantifies tissue properties in both bone and soft-tissue.

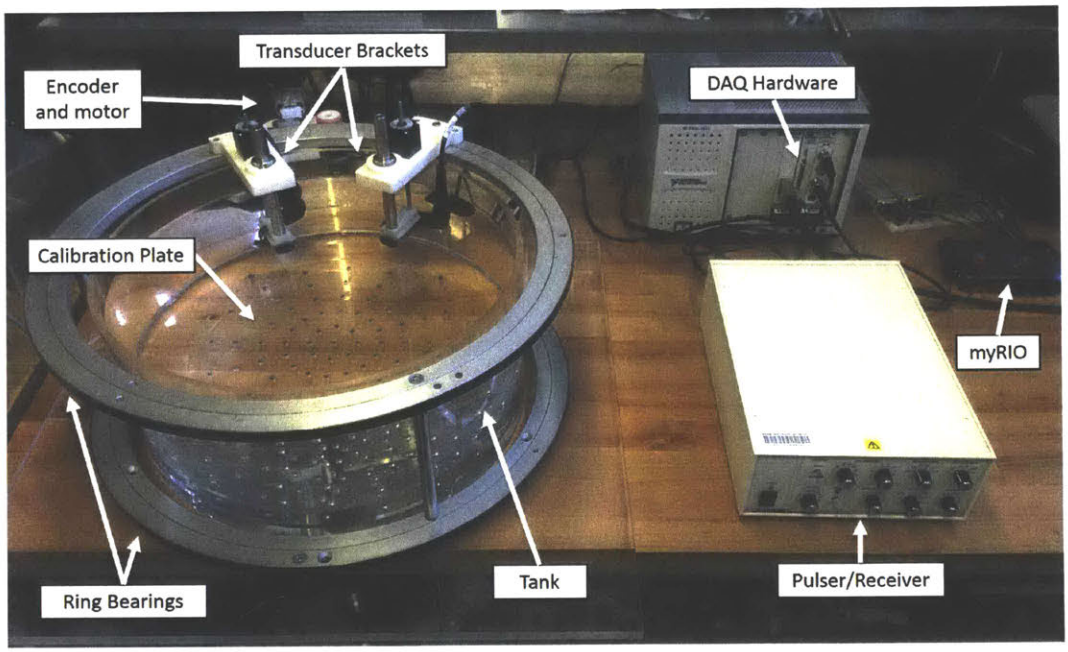

Figure 2-9: Single element tomography system.

2.4 Migration and Echo Flow Migration in Pulse-Echo Limb Imaging

2.4.1 Migration

In the single element system, transducers with a wide beamwidth is used to fully insonify the entire target to maximize reflection data. Consequently, a wide beamwidth transducer (like a point source) cannot determine the direction of arrival of a returning echo. For imaging, a migration algorithm that focuses energy from coherent echos while penalizing incoherent echoes is necessary to accurately reconstruct the target subject [76]. In array imaging, migration is analogous to receive beamforming on all points within the image domain [4].

Migration uses the Born approximation, assuming that each reflector in the image domain is a point source. This however is not true when bone is present. Bone surfaces breaks the Born approximation and behave like a specular reflector rather than a point source. Furthermore, echoes from bone boundaries can be two orders of magnitude larger than soft-tissue echoes. Blindly implementing migration for bone imaging significantly degrades the dynamic range and migration artifacts from bone boundaries can shadow weaker soft-tissue features in the image.

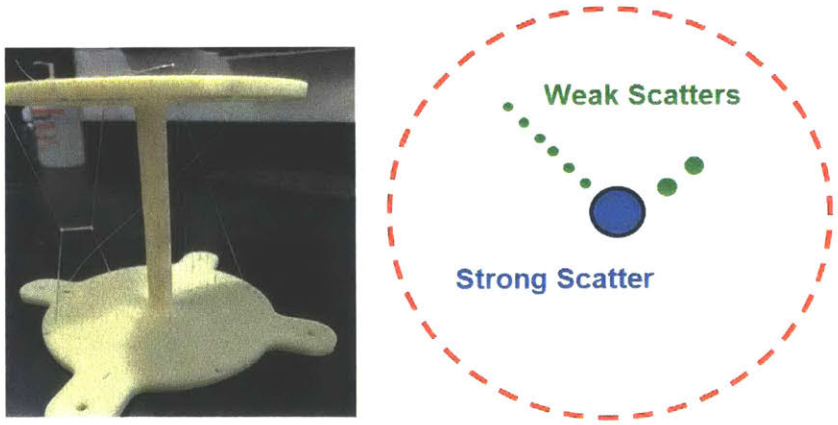

(a) Thread phantom

(b) Cross section schematic of the thread phantom

Figure 2-10: Thread phantom modeling strong and weak scattering in limbs

A phantom (shown in Figure 2-10) with varying size nylon threads and a central ABS plastic post was built to mimic features typical of limb imaging. The central ABS post is a strong reflector similar to bone while the nylon treads mimic soft-tissue reflectors at various radii from the center. A photograph of the phantom is shown in Figure 2-10a. In diameter, the central post is 12 mm, the two larger nylon treads are 0.3 mm, and the 7 smaller threads are 0.076 mm at 6 mm apart. The phantom was imaged in the single element system with a 2.25 MHz 60° beamwidth transducer. Raw data and reconstructed image using conventional migration is shown in Figure 2-11a and 2-11b, respectively.

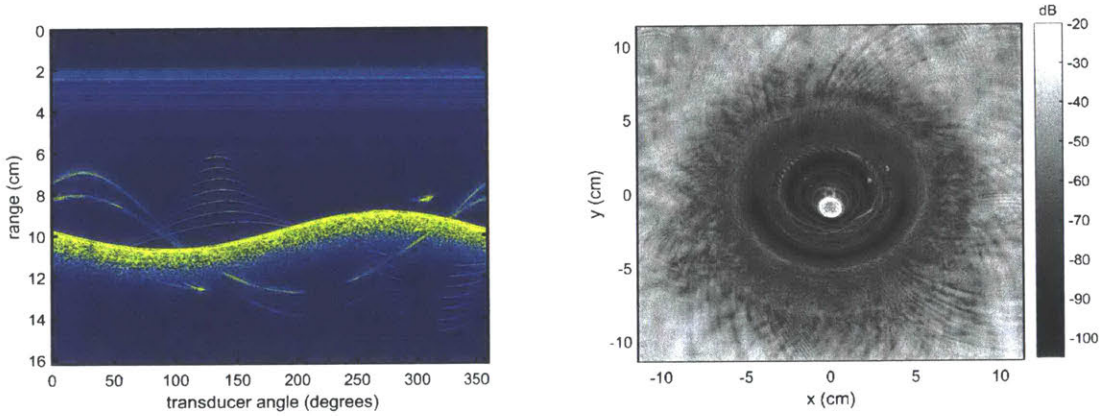

(a) Raw data (b) Migrated

Figure 2-11: Raw and migrated thread phantom data taken in the single element system.

In the raw data, echos from individual threads can be seen with a strong reflection coming from the central post. When migrated, the strong reflection from the central post is distributed across the entirety of the image and weaker reflections from the threads are completely shadowed. To correct for this, a novel echo flow migration was developed and is presented in Section 2.4.2

2.4.2 Echo Flow Migration

Conventional migration evenly distributes energy for all received echos across the entire transducer beamwidth. For a single pulse-echo instance (one pixel column in the raw data in Figure 2-11a), angular direction of arrival of an echo is indistinguishable within the beamwidth. However, the motion path of the transducer during scanning is known. By incorporating multiple scan instances and tracking how each reflection moves as the transducer is moving, an estimate of the angle of arrival of each reflection can be computed. The angle of arrival estimation is completed using the canny edge detector [77] and the Hough transform [78]. The canny edge detector finds line segments in a rolling 11x11 pixel window (7 pixel overlap) in the raw data, corresponding to reflections from a point scatterer as the transducer is moving. The Hough transform then estimates the angle of the line segment relative to the transducer which is the estimate of the angle of arrival to the transducer. Figure 2-12a shows the estimated angle of arrival for the raw data presented in Figure 2-11a. For each point in the raw data, the measured angle of arrival estimate is compared against the expected angle of arrival (if a point scatterer is present at that point). Each point in the raw data is then weighted by $W_{i,j}(n)$, the degree by which the measured and the expected angles match, as described in Equation 2.1.

$$W_{i,j}(n) = e^{\frac{-(\theta(D)-\phi_{i,j})^2}{2A(D)}} \tag{2.1}$$

where $\theta(D)$ is the estimated angle of arrival of raw data set D, ϕ is the expected angle of arrival, and $A(D)$ is the Hilbert transform of the raw data for envelope detection.

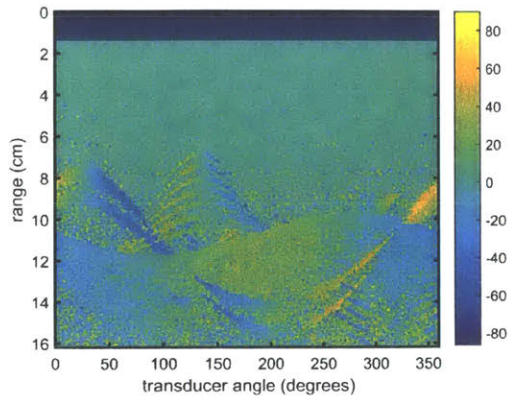

(a) Direction of arrival computed for raw data from Figure 2-11a.

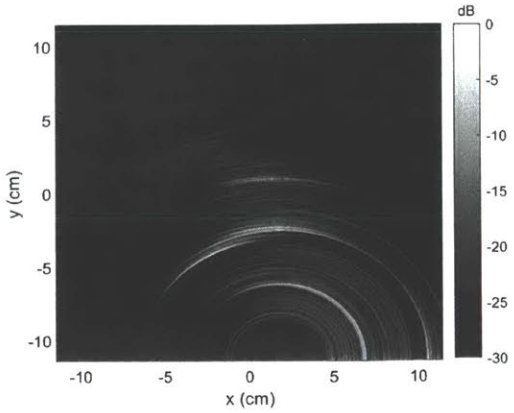

(b) Migration of a single trace with direction of arrival estimate.

Figure 2-12: Direction of arrival estimate and resulting migration.

Shown in Figure 2-12a, by estimating the angle of arrival, reflected energy from each pulse-echo instance can be distributed with angular discrepancy. Echo flow migration (EFM) using the angle of arrival estimates restricts strong reflections to limited spatial locations within the image and prevents strong reflections from shadowing weaker reflections. Shown in Figure 2-13, using EFM on the phantom data successfully recovers the weaker reflections from the nylon threads. Conventional migration is copied from Figure 2-11b to Figure 2-13a for direct comparison.

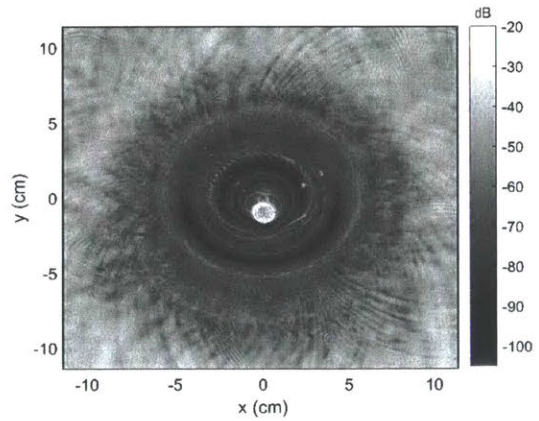

(a) Conventional Migration

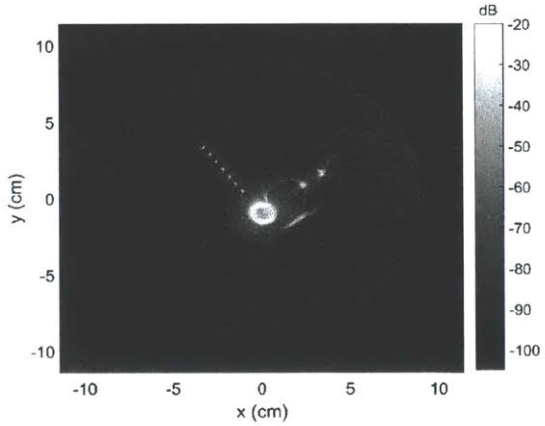

(b) EFM Migrated

Figure 2-13: Echo flow migration compared to conventional migration.

Following imaging on phantoms, EFM was evaluated on excised bovine tissue as

the human limb analog. Pulse-echo imaging using migration compared to EFM are presented in Figure 2-14.

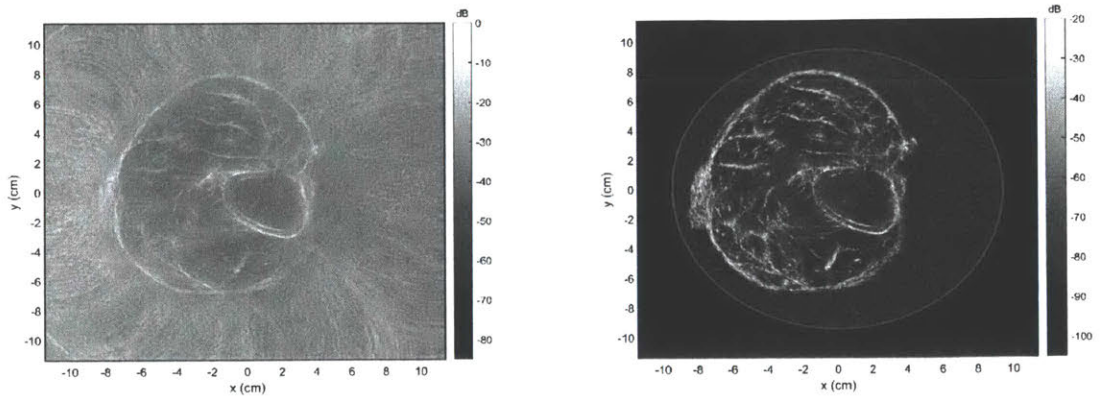

(a) Conventional Migration

(b) EFM Migrated

(c) Bovine Shank Photo

Figure 2-14: Echo flow migration on bovine shank.

The dynamic range of the EFM image is comparable to the dynamic range of clinical ultrasound images [4]. Contrast is significantly improved using EFM and artifacts near the bone surfaces are significantly reduced. Soft tissue features are enhanced by EFM and weaker reflecting features can be seen. By inspection, similar tissue features can be seen in the photograph of the shank's top surface in Figure 2-14c. The measured ultrasound slice is at the mid section of the shank and cannot be directly seen via photography. For limb imaging, EFM will be necessary to recover soft-tissue features surrounding the bone.

2.4.3 Volumetric Imaging

Using EFM, multiple pulse-echo image slices were captured and reconstructed on the bovine shank tissue to generate volumetric images. Both pulse-echo and tomographic data were taken on the bovine shank to evaluate EFM and quantitative algorithms, respectively. Quantitative imaging using Full Waveform Inversion is discussed later in Section 2.5. To generate volumetric images, 22 slices at 3.18 *mm* separation were stacked to generate the 3D volume of the bovine shank in Figure 2-15d.

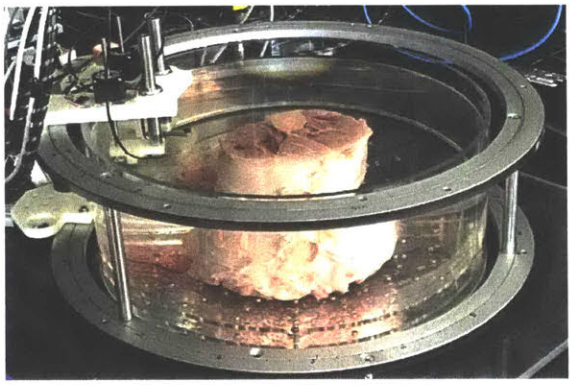

(a) Shank during imaging

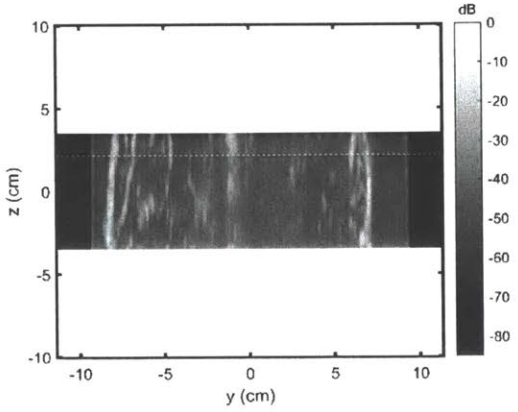

(b) Y-Z Slice

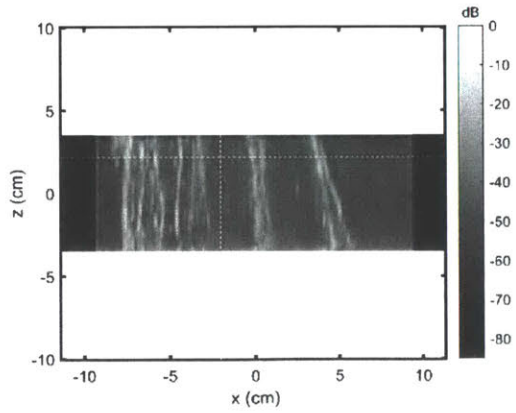

(c) X-Z Slice

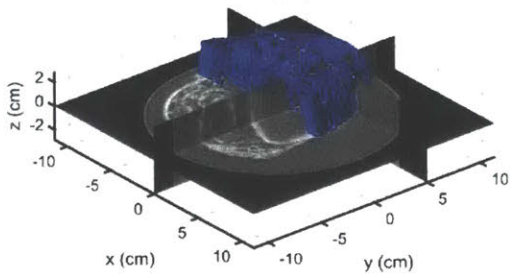

(d) Isometric View with segmentation

Figure 2-15: Volumetric imaging with EFM slices.

With increased contrast from EFM, tissue boundaries can be segmented in bovine tissue to capture tissue volumes in 3D images. Preliminary segmentation of the bone volume is shown in Figure 2-15; robust segmentation of pulse-echo ultrasound volumes is a challenge and an active research area but is outside the scope of this thesis.

2.5 Tomographic Imaging using Full Waveform Inversion

For limb imaging using ultrasound, the primary challenge for pulse-echo is the bone; the same challenge is true for tomography. Previous UST systems discussed in 2.1 assumes small changes in speed of sound (SoS) which is true for breast imaging. Ray tracing inversion methods used in quantitative breast imaging cannot quantify tissue properties when bone is present. In soft-tissue, acoustic waves can propagate through without encountering significant acoustic impedance change. Acoustic impedance (Z) is defined as the product of density ρ and speed of sound c. In soft-tissue, density and SoS is approximately that of water 1000 kg/m^3 and 1500 m/s, respectively. Within the body, there is very little change in acoustic impedance in soft-tissue. The largest impedance change ($\sim$10%) in soft-tissue is in the lungs, due to air presence. In bone, density and SoS are $\sim$1900 kg/m^3 and $\sim$3000 m/s, respectively [4]. Impedance change due to bone reflects 100 times more acoustic energy than soft-tissue. Strong refraction from bone surfaces break assumptions made in ray tracing methods in soft-tissue UST [79]. Furthermore, acoustic propagation across a bone boundary is complex, producing mode conversions that generate shear waves from longitudinal waves and vice-versa [4]. Conventional medical ultrasound does not typically encounter high impedance during imaging. However, high impedance changes is typical in seismic applications where large variations in SoS between geological features such as water, rock, salt, oil, is commonplace. Techniques developed in seismology to quantify SoS in the Earth can be leveraged for quantitative SoS in limb imaging [79].

Full Waveform Inversion (FWI) is an non-linear optimization method that quantifies features by iteratively comparing the measured wavefield against a modeled wavefield. Unlike ray tracing, where the time of flight of acoustic rays estimates the SoS in the domain, FWI uses a estimated forward model of the domain and simulates the entire acoustic propagation. The forward simulation results are compared against the measured waveforms and the model is improved iteratively. The FWI algorithm and data presented here was developed jointly with Jonathan Fincke. Detailed discus-

sions of the FWI algorithm used here is presented in the Doctorate thesis by Fincke [79]. An outline of the FWI algorithm is presented in Figure 2-16.

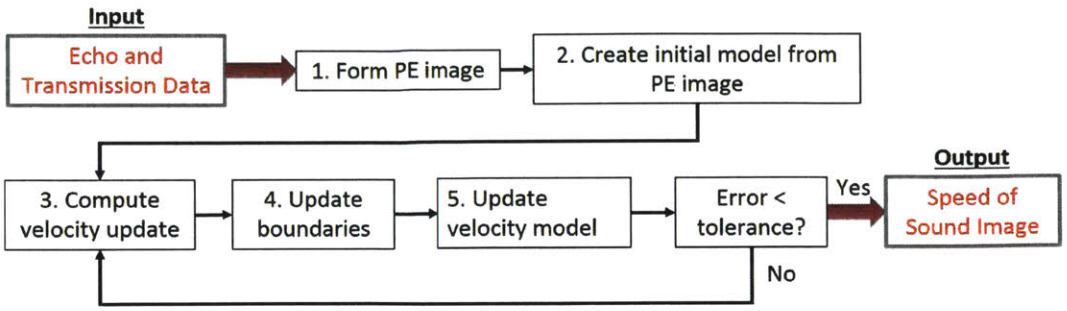

Figure 2-16: Full Waveform Inversion Block Diagram

Unlike FWI in seismic, the algorithm presented in Figure 2-16, uses an initial SoS model informed by segmenting an iso-velocity pulse-echo image. This initial guess helps to spatially constrain SoS updates during optimization and initiates the model closer to realistic tissue values. Quantifiable parameters using FWI are dictated by the complexity of the forward acoustic simulation. Typically, SoS is the parameter of interest as an indicator of tissue stiffness. Other parameters, such as attenuation and density can computed but is not the focus of the current FWI algorithm. For the FWI algorithm presented here, SoS in the muscle, fat, and bone are identified in the imaged domain. FWI was first evaluated in simulation then applied in excised bovine tissue imaging.

2.5.1 FWI - Simulated

Synthetic observation data for FWI was simulated in k-wave, a MATLAB based acosutic simulation toolbox [80, 81]. The cross-sectional model simulating a human long bone surrounded by soft-tissue was taken from the Visible Human Project [82]. Virtual transducer transmit and receive patterns follow that of the data acquisition in the single element system discussed in Section 2.5.2. SoS, attenuation, and density values labeled based on prior literature values [83, 84]. True SoS values from the model and FWI inverted values are presented in Figure 2-17a and 2-17b; absolute difference between the true and inverted model is shown in Figure 2-17c.

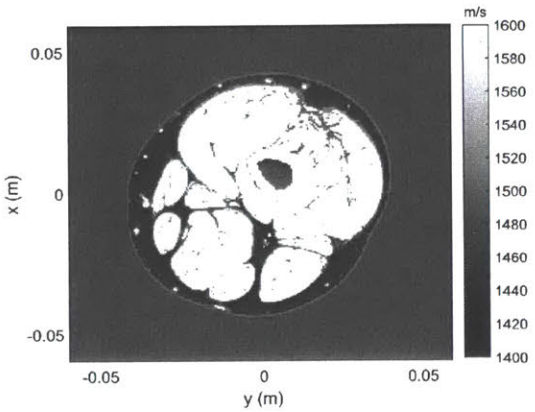

(a) True SoS

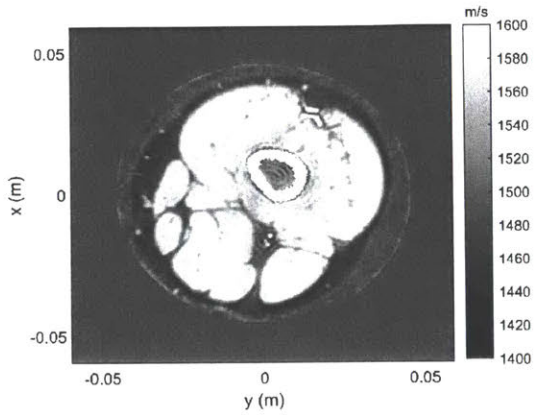

(b) FWI SoS

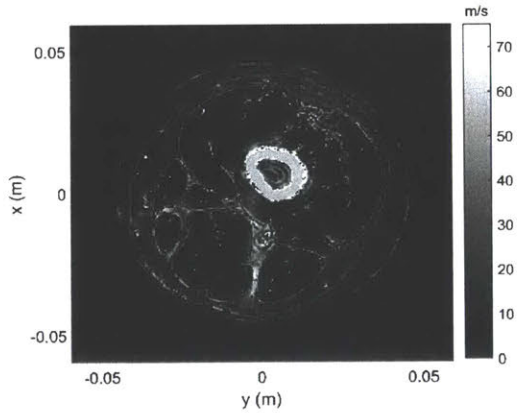

(c) Absolute SoS Error

Figure 2-17: Full waveform inversion on simulated data.

Material	True (m/s)	Inverted (m/s)	Error (m/s)	Error (%)
Bone	3200	3140	-60	1.9
Soft-Tissue	1540	1546	6	0.4
Water	1480	1480	<1	<0.1

Table 2.1: FWI error on simulated data

Inverted bone SoS error was 60 m/s and average SoS error in soft tissue was 6 m/s, corresponding to 1.9% and 0.4% respectively. Inverted feature boundaries are within one pixel value. Simulated FWI indicates the technique is feasible for bone quantitative imaging.

2.5.2 FWI - Bovine Tissue

Data for FWI on excised tissue was taken on the single element system. Beef shank from a local butcher was centered in the single element system fill with de-ionized water. The shank contained one bovine long-bone surrounded with muscle and fat tissue. Tomographic transmit apertures used 72 transmit locations equally spaced at 5° around the tank each with 1533 receive locations at 0.2345° increments. For each transmit location, the total receive aperture was 313° to prevent physical collision of the transmitter and receiver bracketing during scanning. All transducers were operating at 0.5 *MHz*. The transmit transducer had 65° beamwidth while the receive transducer was a point receiver. All scans were approved by the MIT Committee for Animal Care and all acoustic exposure levels were all within FDA safety limits as verified in the acoustic calibrations in Section 3.6. Ground truth SoS in the bovine tissue was measured by placing tissue sample between a transmitter and a receiver at a known distance (measured by a micrometer) and measuring the travel time; SoS was computed by dividing the measured micrometer distance by the measured travel time. Photograph of the bovine tissue and the inverted FWI image is shown in Figure 2-18b. An MRI cross-section of the shank is shown in Figure 2-18a for geometric feature comparison. Absolute error in SoS compared to the measured ground truth is tabulated in Table 2.2.

The FWI inverted models show broad feature agreement with the MRI cross-

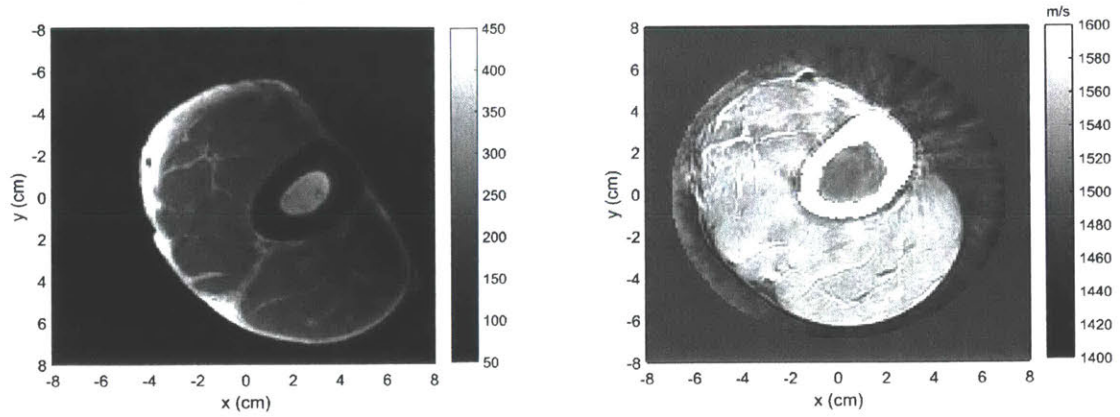

(a) MRI (b) FWI SoS

Figure 2-18: Full waveform inversion of experimental data on bovine shank .

Material	**True** (m/s)	**Inverted** (m/s)	**Error** (m/s)	**Error** (%)
Bone	3359	3029	-330	9.82
Muscle	1556	1565	9	0.58
Fat	1481	1467	-14	0.95
Water	1484	1482	-2	0.13

Table 2.2: FWI error on bovine shank

section. Exact geometric comparison is not feasible due to gravitational load changes in soft-tissue when the shank is oriented differently between ultrasound and MRI scanning; shank is upright in US scanning and laid on its side in MRI scanning. Regardless, similar soft-tissue features are visible in both imaging modalities. Quantitative measures of the SoS in soft-tissue using FWI is within 1% of the ground truth values. Bone SoS is up to 10% in error and is likely due to poor segmentation of the bone boundary and non-orthogonality of the bone surface relative to the transducers during data acquisition, causing strong out of plane reflections. Despite the challenges of bone, the FWI algorithm developed here successfully recovers quantitative SoS values within the tissue at clinically acceptable error levels [4].

2.6 Summary

Limb imaging using ultrasound is challenging due to the high impedance difference between bone and soft-tissue. Bone generates strong specular reflections, high attenuation, and complex acoustic propagation modes. Previous methods relevant for soft-tissue imaging are not applicable for limb imaging. New techniques and systems for pulse-echo imaging and tomographic imaging are necessary to develop methods to accommodate the presence of bone. The single element system presented here demonstrates capability and flexibility of low-cost mechanically scanned UST systems to iteratively and cost-effectively develop and test new algorithms for limb imaging.

New EFM and FWI algorithms evaluated on simulation, phantoms, and excised animal tissue data using the single element system generated promising geometric and quantitative images. EFM corrects for the strong specular reflections of bone and recovers soft-tissue features surrounding the bone. EFM images presented here has dynamic range comparable to that of clinical ultrasound images. Imaging using FWI quantified soft-tissue SoS with 1% error and bone SoS with 10% error. FWI results on excised bovine shank tissue is the first step in applying quantitative ultrasound techniques to identify limb properties. Use of low frequency transducers to transmit through the bone in conjunction with computations algorithms inspired by related techniques from seismology identified quantitative tissue parameters with remarkable accuracy.

Improvements in system design are necessary to apply EFM and FWI for human imaging. Imaging speed need to be reduced to acquire data on human subjects without significant motion artifacts. A simple yet effective to reduce scan time is to add more transducers in the system. For each added transducer, the total scan time is reduced by 1 divided by the total number of transducers in the system (1/X). However, independent mechanical actuators must be added for each transducer per degree of freedom, increasing total hardware cost of the system. The 1/X reduction in scan time is effective until approximately 6 transducers before reaching exponentially diminishing returns. Furthermore, actuation requirements for more than 6 sets of

independent mechanical positioners may be more complex and less cost effective than building a fixed ring/conical array system. The single element platform was valuable in developing and testing new algorithms for limb imaging. Results presented in this chapter motivates further development of the system for human subject testing. The next chapter discusses development and initial testing of a multi-transducer multi-DOF system motivated by results from the single element system.

Chapter 3

MEDUSA

Motivated by the promising imaging results on tissue mimicking phantoms and excised animal tissue, the next iteration of flexible ultrasound tomography system is described in this chapter. MEchanically Discretized Ultrasound Scanning Apparatus (MEDUSA) is a 36 degrees of freedom positioning system using 6 robotic arms, each holding a ultrasonic transmitter and receiver pair. Ultrasonic imaging using MEDUSA is driven by a Cephasonics Cicada system, a programmable ultrasonic imaging system. Full 6 degrees of freedom free space positioning of each transducer allows evaluation of new imaging methods to further improve limb imaging. This chapter presents the MEDUSA design methodology, detailed system design and controls, calibration, and preliminary imaging results.

3.1 High Level System Design

3.1.1 Functional Requirements

The high-level functional requirements for designing MEDUSA is primarily derived from requirements to safely and quantitatively image a human distal limb *in-vivo* using ultrasound. Secondarily, the system must have sufficient flexibility for development of new imaging methods. The high-level functional requirements for MEDUSA are summarized as follows:

- ***Size*** — The system size must accommodate an average human distal limb (forearm/lower leg).
- ***Speed*** — The system must be able to acquire data at a sufficient rate for *in-vivo* human imaging in a reasonable amount of time.
- ***Safety*** — The system must be safe for human subjects. Both mechanical positioning systems and acoustic energy output must be safe for human subjects.
- ***Imaging*** — The system must obtain quantitative data from the imaging target.
- ***Flexibility*** — For iterative development of new algorithms, the acoustic aperture should be flexible and various transducers should be able to be tested on the system.

3.1.2 Design Parameters

From the functional requirements, specific numerical design parameters were defined based on average human anthropometric measurements from the National Aeronautics and Space Administration (NASA), prior scan data, and the relevant safety restrictions as dictated by the FDA [85–87].

Physical Dimensions — The system size must accommodate an average human distal limb (forearm/lower leg) which is 4-6 *in* in diameter and ~12 *in* in length.

Speed — All scans shall take less that 10 minutes to minimize motion artifacts.

Transducer Degrees of Freedom — Each transducer should have 6 degrees of freedom within the imaging aperture.

Transducer frequency — For quantitative imaging through bone, the transducers should have 0.5 *MHz* center frequency.

Positioning Repeatability — Positioning repeatability must be within 1 wavelength of the transducer center frequency (<3 *mm* at 0.5 *MHz*).

Safety — *Acoustic*: Maximum acoustic exposure shall be within the FDA limits for peripheral vessel imaging (<720 mW/cm^2). *Mechanical*: Mechanical system should not make contact with the subject during imaging.

3.2 Detailed Mechanical System Design

Based on the 60 minute tomographic scan time of the previous single element system, at least 6 transducers are necessary to reduce the total scan time to less than 10 minutes. All transducers share identical degrees of freedom requirements, workspace size, and accuracy requirements, replicated circumferentially around the imaging target. Modularity in designing each mechanical positioner for each transducer is greatly beneficial in reducing overall system complexity.

Each transducer must have 6 degrees of freedom in the workspace. Traditional Cartesian positioning systems can satisfy translation positioning (XYZ) but are generally bulky linear stages that do not include full roll-pitch-raw movement at the endpoint. Full 6-DOF positioning systems are either robotic manipulators or Steward Platforms. Each system is shown in Figure 3-1 for comparison.

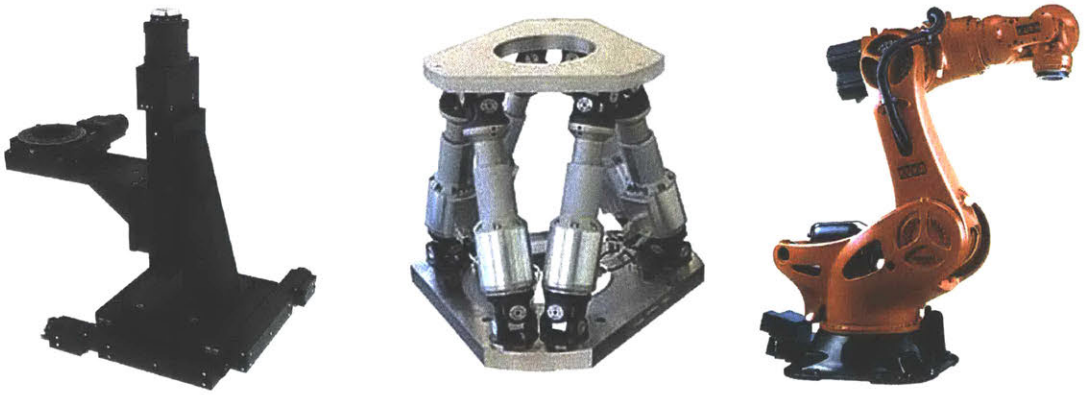

(a) XYZ Positioner (b) Steward Platform (c) Robotic Manipulator

Figure 3-1: Optical source and detector selected for LUS imaging

Based on the required DOF and large motion ranges, robotic manipulators with 6-DOF end-effector positioning are ideal for satisfying the design requirements. Robotic manipulators are complex mechanical systems but the literature field is well developed. Use of robotic manipulators range from simple pick-and-place, manufacturing, to rehabilitation, the broad flexibility of these system is ideal for use in a developmental platform.

3.2.1 Individual Arm

Servo Selection — A plethora of commercial robotic manipulators exist but careful consideration must be given to the workspace size, positioning feedback, and cost. Robotic manipulators range from hobby to industrial level designs depending on the use case. Capabilities of each manipulator design is largely dictated by the servo motors used in each joint. Whereas hobby level manipulators generally focus on the average consumer market by minimizing cost by sacrificing servo performance (accuracy, speed, maximum load, feedback), industrial manipulators must satisfy higher performance standards for manufacturing or research. Various robotic arms with differing servo capabilities are shown in Figure 3-2.

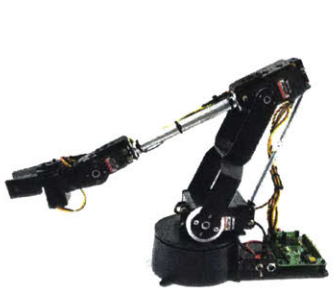

(a) Hobby Arm

(b) Research Arm

(c) Industrial Arm

(d) Hobby Servo

(e) "Smart" Servo

(f) Harmonic Drive

Figure 3-2: Survey of robotic arm kits and servos

For designing MEDUSA, positional feedback is most critical for ultrasound image reconstruction. Based on the design parameters, positioning repeatability must be <3 mm to satisfy the imaging requirements at 500 kHZ. In image reconstruction, having

positional knowledge of the transducer is more important than accurately following a given command trajectory. In addition, individual MEDUSA arms will operate in close proximity to human subjects, high torque capabilities of industrial servos (typically harmonic drives) may pose a significant safety hazard in case of human contact. Using a weighted Pugh chart to compare the servos types in Table 3.1, smart servos used in robotic/research applications are the ideal candidate for MEDUSA. The Pugh chart is weighted 1-3 for each criteria and each rating is between 1-5, with the hobby servo as the reference for comparison. Dynamixel smart servos, pictured in Figure 3-2e, have the desired feedback, programmable controls, low weight, and cost effectiveness. More specifically, the MX-64 and MX-28's were tested and selected to design the arms for MEDUSA.

Criteria	Weight	Hobby	Smart	Industrial
Max Load	2	3	4	5
Weight	2	3	4	1
Accuracy	2	3	4	5
Repeatability	3	3	4	4
Resolution	2	3	4	5
Speed	1	3	4	4
Multi-turn	2	3	4	4
Feedback	3	3	5	5
Programmable	3	3	5	5
Safety	3	3	4	1
	Total	69	98	89

Table 3.1: Pugh chart comparing servos

Servo Layout and Arm Dimensions — For full 6-DOF actuation, the servos are laid out in the anthropomorphic arm with a spherical wrist configuration, shown in Figure 3-3. This configuration combines the Cartesian positioning capabilities of the anthropomorphic arm with the rotation capabilities of the spherical wrist. Since this configuration satisfies the kinematics conditions listed in Section 3.2.2, the inverse kinematic problem is directly solvable [2].

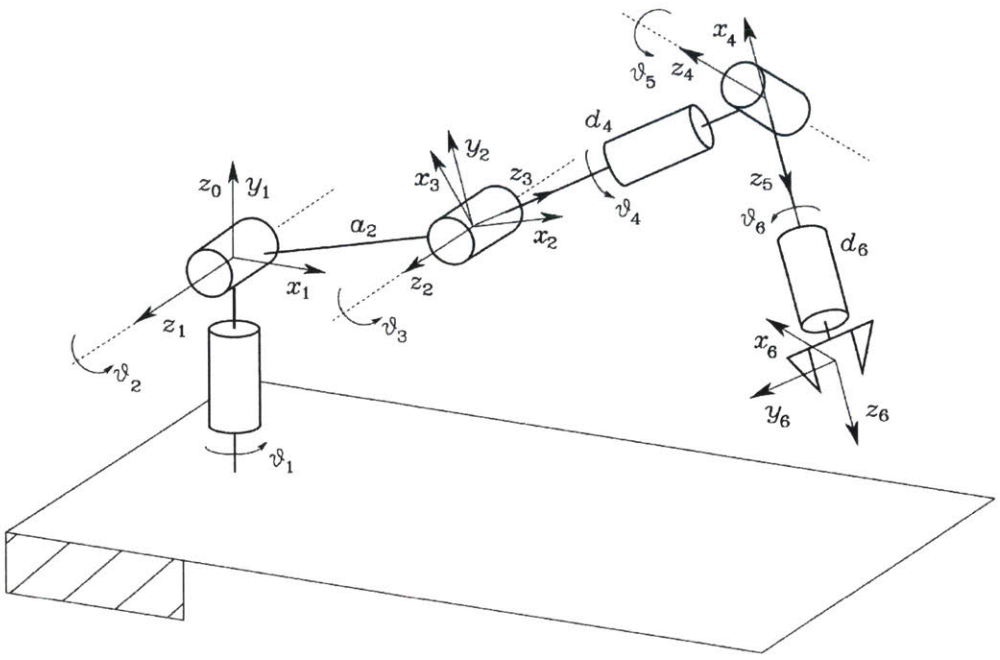

Figure 3-3: Anthropomorphic arm with spherical wrist [2]

Arm Dimensions — Based on the servo layout, the minimum parameters to describe the arm can be reduced to the Denavit-Hartenberg parameters shown in Table 3.2. To reach the extremities of the desired workspace, the actual dimensions of the arm are listed in parentheses.

Link	a_i (m)	α_i (rad)	d_i (m)	ϑ_i (rad)
1	0	$\pi/2$	0	ϑ_1
2	a_2 (5.25 in)	0	0	ϑ_2
3	0	$\pi/2$	0	ϑ_3
4	0	-$\pi/2$	d_4 (5.25 in)	ϑ_4
5	0	$\pi/2$	0	ϑ_5
6	0	0	d_6 (9.70 in)	ϑ_6

Table 3.2: Denavit-Hartenberg parameters and physical dimensions describing the anthropomorphic arm with spherical wrist

3.2.2 Kinematics

For control of the end-effector to a desired imaging position, the forward and inverse kinematics are directly calculated. Forward kinematics takes joint positions (q) and computes the end-effector position and orientation (p). Inverse kinematics takes a desired end-effector position and orientation (p) and computes the necessary joint positions (q). The forward calculation is a linear transformation while the inverse kinematic calculation is non-linear with multiple solutions . This is due to the fact that multiple joint positions can reach the same end-effector position and orientation. The direction and frames for the forward and inverse kinematics is shown in Figure 3-4. Origin of the base and end-effector frames are highlighted in yellow; red, green, blue axes correspond to XYZ and nsa axes for the base and end-effector, respectively.

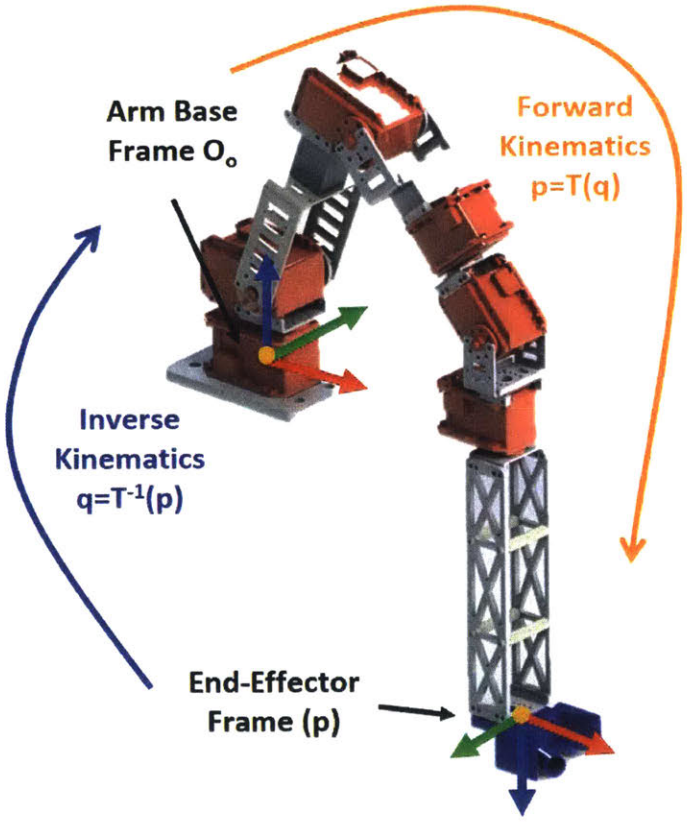

Figure 3-4: Forward and inverse kinematics for a single arm

Forward Kinematics — The position and orientation of the end-effector relative to the arm base frame O_0 can be described by a (4×4) matrix shown in Equation 3.1, which is computed by the homogeneous transformation $\mathbf{T}_6^0(q)$ [2].

$$p = \mathbf{T}_6^0(q) = \begin{bmatrix} \mathbf{n}(q) & \mathbf{s}(q) & \mathbf{a}(q) & \mathbf{p}(q) \\ 0 & 0 & 0 & 1 \end{bmatrix} \tag{3.1}$$

where $\mathbf{n}$, $\mathbf{s}$, and $\mathbf{a}$ are (3×1) unit vectors describing the end-effector orientation and $\mathbf{p}$ is the (3×1) vector describing end-effector position, both relative to the base frame O_0. q is the (6×1) vector of joint angles ϑ_1, ϑ_2 ... ϑ_6

The forward kinematic computation to find $\mathbf{n}$, $\mathbf{s}$, $\mathbf{a}$, and $\mathbf{p}$ is shown in Equation 3.2 - 3.5, where $s_n = \sin(\vartheta_n)$, $c_n = \cos(\vartheta_n)$, $s_{nm} = \sin(\vartheta_n + \vartheta_m)$, and $c_{nm} = \cos(\vartheta_n + \vartheta_m)$

$$\mathbf{p}(q) = \begin{bmatrix} a_2 c_1 c_2 + d_4 c_1 s_{23} + d_6(c_1(c_{23}c_4 s_5 + s_{23}c_5) + s_1 s_4 s_5) \\ a_2 s_1 c_2 + d_4 s_1 s_{23} + d_6(s_1(c_{23}c_4 s_5 + s_{23}c_5) - c_1 s_4 s_5) \\ a_2 s_2 - d_4 c_{23} + d_6(s_{23}c_4 s_5 - c_{23}c_5) \end{bmatrix} \tag{3.2}$$

$$\mathbf{n}(q) = \begin{bmatrix} c_1(c_{23}(c_4 c_5 c_6 - s_4 s_6) - s_{23}s_5 c_6) + s_1(s_4 c_5 c_6 + c_4 s_6) \\ s_1(c_{23}(c_4 c_5 c_6 - s_4 s_6) - s_{23}s_5 c_6) - c_1(s_4 c_5 c_6 + c_4 s_6) \\ s_{23}(c_4 c_5 c_6 - s_4 s_6) + c_{23}s_5 c_6 \end{bmatrix} \tag{3.3}$$

$$\mathbf{s}(q) = \begin{bmatrix} c_1(-c_{23}(c_4 c_5 s_6 + s_4 c_6) + s_{23}s_5 s_6) + s_1(-s_4 c_5 s_6 + c_4 c_6) \\ s_1(-c_{23}(c_4 c_5 s_6 + s_4 c_6) + s_{23}s_5 s_6) - c_1(-s_4 c_5 s_6 + c_4 c_6) \\ -s_{23}(c_4 c_5 s_6 + s_4 c_6) - c_{23}s_5 s_6 \end{bmatrix} \tag{3.4}$$

$$\mathbf{a}(q) = \begin{bmatrix} c_1(c_{23}c_4 s_5 + s_{23}c_5) + s_1 s_4 s_5 \\ s_1(c_{23}c_4 s_5 + s_{23}c_5) - c_1 s_4 s_5 \\ s_{23}c_4 s_5 - c_{23}c_5 \end{bmatrix} \tag{3.5}$$

Inverse Kinematics — The inverse kinematics for the anthropomorphic arm with a spherical wrist are described from Equation 3.6 - 3.36. In most cases, a closed-form inverse kinematic solution for an arbitrary multi-DOF layout is difficult to find or may not exist, due to the multiplicity or lack of solutions in the joint space. However, a closed-form solution does exist for a 6-DOF (non-redundant) kinematic structure if two conditions are satisfied:

- three consecutive revolute joint axes intersect at a common point, like for the spherical wrist;
- three consecutive revolute joint axes are parallel.

These conditions are satisfied by the anthropomorphic arm with a spherical wrist and is the reason why most robotic manipulators involve some combination of the arm or wrist. The two conditions mentioned equates to decoupling the orientation and position inverse computations. A point p_W at the center of rotation of the spherical wrist can be identified to separate the arm joints from the wrist joints. p_W, p_e, and R_e are diagrammed in Figure 3-5.

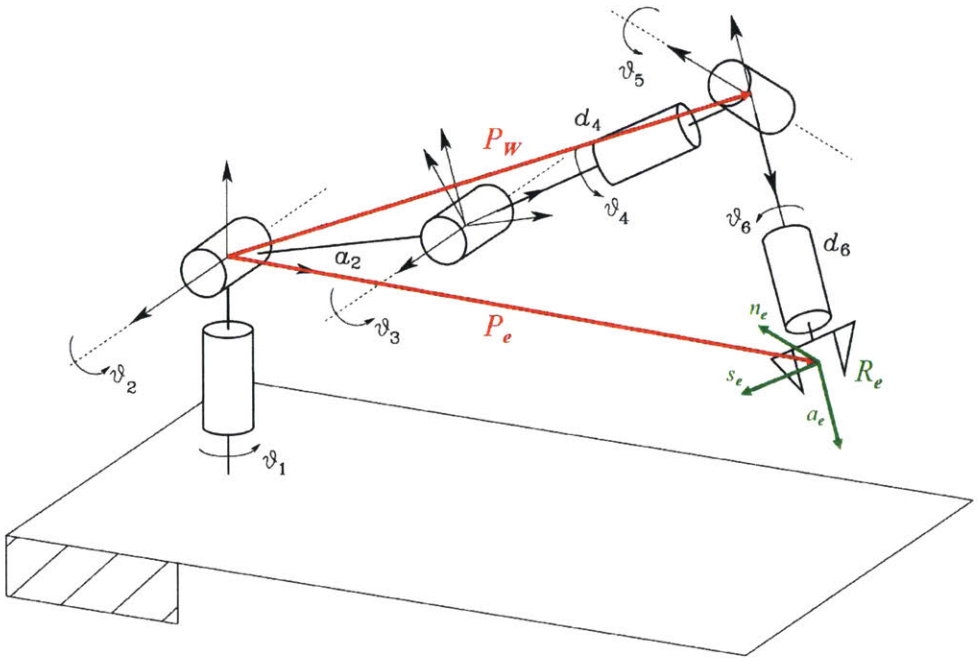

Figure 3-5: Decoupling of arm and wrist for inverse kinematic calculations.

$$p = \begin{bmatrix} R_e & p_e \\ 0 & 1 \end{bmatrix} ; p_W = \begin{bmatrix} p_{Wx} \\ p_{Wy} \\ p_{Wz} \end{bmatrix} \tag{3.6}$$

$$R_e = \begin{bmatrix} n_{ex} & s_{ex} & a_{ex} \\ n_{ey} & s_{ey} & a_{ey} \\ n_{ez} & s_{ez} & a_{ez} \end{bmatrix} ; p_e = \begin{bmatrix} p_{ex} \\ p_{ey} \\ p_{ez} \end{bmatrix} \tag{3.7}$$

If the position p_e and orientation R_e of the end-effector are given, the closed-form solutions for joint angles ϑ_1, ϑ_2 ... ϑ_6 can be computed following the steps below. Again, $s_n = \sin(\vartheta_n)$, $c_n = \cos(\vartheta_n)$, $s_{nm} = \sin(\vartheta_n+\vartheta_m)$, and $c_{nm} = \cos(\vartheta_n+\vartheta_m)$.

1. Compute the wrist position p_W where

$$p_W = p_e - d_6 a_e \tag{3.8}$$

2. Solve inverse kinematics for (ϑ_1, ϑ_2, ϑ_3)

   For ϑ_3 find

$$c_3 = \frac{{p_{Wx}}^2 + {p_{Wy}}^2 + {p_{Wz}}^2 - {a_2}^2 - {d_4}^2}{2{a_2}^2{d_4}^2} \tag{3.9}$$

$$s_3 = \pm\sqrt{1 - {c_3}^2} \tag{3.10}$$

   From Equation 3.9 and 3.10, compute

$$\vartheta_3 = Atan2(s_3, c_3) \tag{3.11}$$

   Equation 3.11 yields 2 solutions depending on the sign of s_3

$$\vartheta_{3,I} \in [-\pi, \pi] \tag{3.12}$$

$$\vartheta_{3,II} = -\vartheta_{3,I} \tag{3.13}$$

For ϑ_2 find

$$c_2 = \frac{\pm\sqrt{{p_{Wx}}^2 + {p_{Wy}}^2}(a_2 + a_3 c_3) + p_{Wz} a_3 s_3}{{a_2}^2 + {a_3}^2 + 2 a_2 a_3 c_3} \tag{3.14}$$

$$s_2 = \frac{p_{Wz}(a_2 + a_3 c_3) \mp \sqrt{{p_{Wx}}^2 + {p_{Wy}}^2} a_3 s_3}{{a_2}^2 + {a_3}^2 + 2 a_2 a_3 c_3} \tag{3.15}$$

From Equation 3.14 and 3.15 compute

$$\vartheta_2 = Atan2(s_2, c_2) \tag{3.16}$$

which gives 4 solutions to Equation 3.16 depending on the sign of s_3 from Equation 3.10.

For ${s_3}^+ = \sqrt{1 - {c_3}^2}$

$$\begin{aligned} \vartheta_{2,I} = Atan2((a_2 + a_3 c_3) p_{Wz} - a_3 {s_3}^+ \sqrt{{p_{Wx}}^2 + {p_{Wy}}^2}, \\ (a_2 + a_3 c_3)\sqrt{{p_{Wx}}^2 + {p_{Wy}}^2} + a_3 {s_3}^+ p_{Wz}) \end{aligned} \tag{3.17}$$

$$\begin{aligned} \vartheta_{2,II} = Atan2((a_2 + a_3 c_3) p_{Wz} + a_3 {s_3}^+ \sqrt{{p_{Wx}}^2 + {p_{Wy}}^2}, \\ -(a_2 + a_3 c_3)\sqrt{{p_{Wx}}^2 + {p_{Wy}}^2} + a_3 {s_3}^+ p_{Wz}) \end{aligned} \tag{3.18}$$

For ${s_3}^- = -\sqrt{1 - {c_3}^2}$

$$\begin{aligned} \vartheta_{2,III} = Atan2((a_2 + a_3 c_3) p_{Wz} - a_3 {s_3}^- \sqrt{{p_{Wx}}^2 + {p_{Wy}}^2}, \\ (a_2 + a_3 c_3)\sqrt{{p_{Wx}}^2 + {p_{Wy}}^2} + a_3 {s_3}^- p_{Wz}) \end{aligned} \tag{3.19}$$

$$\begin{aligned} \vartheta_{2,IV} = Atan2((a_2 + a_3 c_3) p_{Wz} + a_3 {s_3}^- \sqrt{{p_{Wx}}^2 + {p_{Wy}}^2}, \\ -(a_2 + a_3 c_3)\sqrt{{p_{Wx}}^2 + {p_{Wy}}^2} + a_3 {s_3}^- p_{Wz}) \end{aligned} \tag{3.20}$$

For ϑ_1, rewrite p_{Wx} and p_{Wy} as

$$p_{Wx} = \pm c_1 \sqrt{{p_{Wx}}^2 + {p_{Wy}}^2} \tag{3.21}$$

$$p_{Wy} = \pm s_1 \sqrt{{p_{Wx}}^2 + {p_{Wy}}^2} \tag{3.22}$$

Equation 3.21 and 3.22 gives two solutions for ϑ_1

$$\vartheta_{1,I} = Atan2(p_{Wy}, p_{Wx}) \tag{3.23}$$

$$\vartheta_{1,II} = Atan2(-p_{Wy}, -p_{Wx}) \tag{3.24}$$

In summary there exists four solution sets according to the values of ϑ_3, ϑ_2, and ϑ_1 drawn in Figure 3-6.

$(\vartheta_{1,I}, \vartheta_{2,I}, \vartheta_{3,,I})$ $(\vartheta_{1,I}, \vartheta_{2,III}, \vartheta_{3,II})$ $(\vartheta_{1,II}, \vartheta_{2,II}, \vartheta_{3,I})$ $(\vartheta_{1,II}, \vartheta_{2,IV}, \vartheta_{3,II})$

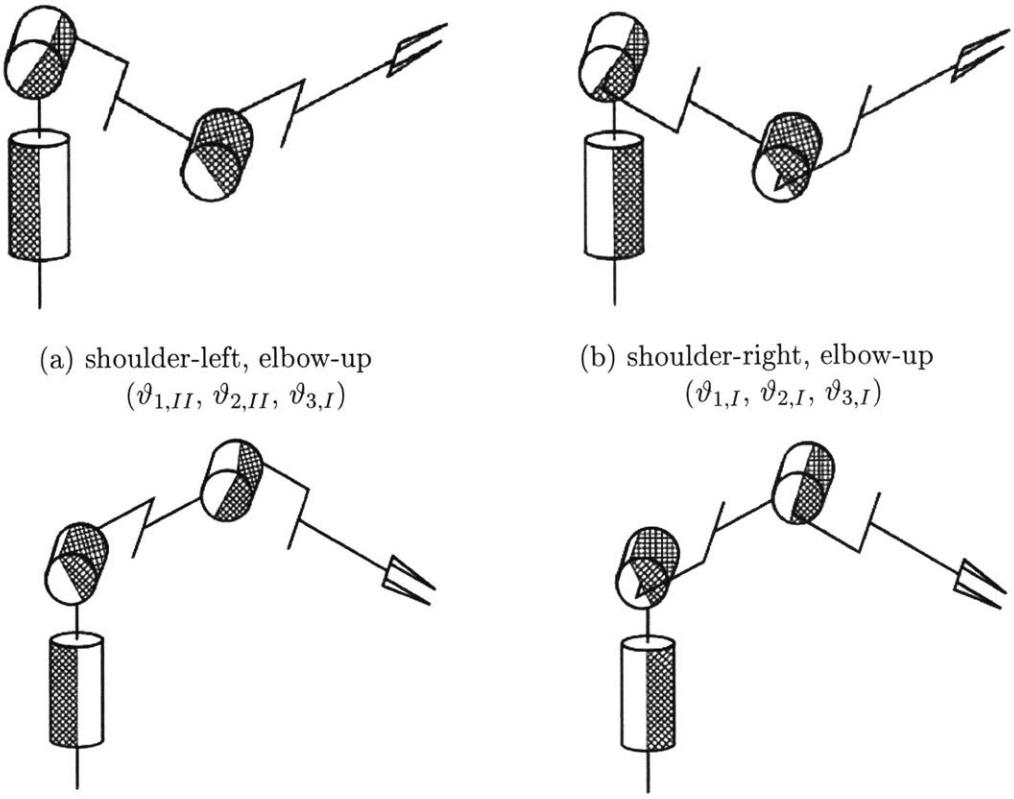

(a) shoulder-left, elbow-up
$(\vartheta_{1,II}, \vartheta_{2,II}, \vartheta_{3,I})$

(b) shoulder-right, elbow-up
$(\vartheta_{1,I}, \vartheta_{2,I}, \vartheta_{3,I})$

(c) shoulder-left, elbow-down
$(\vartheta_{1,II}, \vartheta_{2,IV}, \vartheta_{3,II})$

(d) shoulder-right, elbow-down
$(\vartheta_{1,I}, \vartheta_{2,III}, \vartheta_{3,II})$

Figure 3-6: Four possible solutions to the inverse kinematics

For MEDUSA, shoulder-left, elbow-up is the desired solution.

3. Compute $\mathbf{R}_3^0\ (\vartheta_1,\ \vartheta_2,\ \vartheta_3)$

With ϑ_1, ϑ_2, ϑ_3 the rotation matrices $\mathbf{R}_1^0(\vartheta_1)$, $\mathbf{R}_2^1(\vartheta_2)$, $\mathbf{R}_3^2(\vartheta_3)$ can be calculated, where

$$\mathbf{R}_1^0(\vartheta_1) = \begin{bmatrix} c_1 & 0 & s_1 \\ s_1 & 0 & -c_1 \\ 0 & 1 & 0 \end{bmatrix} \tag{3.25}$$

$$\mathbf{R}_2^1(\vartheta_2) = \begin{bmatrix} c_2 & -s_2 & 0 \\ s_2 & c_2 & 0 \\ 0 & 0 & 1 \end{bmatrix} \tag{3.26}$$

$$\mathbf{R}_3^2(\vartheta_3) = \begin{bmatrix} c_3 & 0 & s_3 \\ s_3 & 0 & \text{-}c_3 \\ 0 & 1 & 0 \end{bmatrix} \tag{3.27}$$

Note: $\vartheta_3 = \vartheta_3 + \pi/2$ to correctly connect the anthropomorphic arm end-frame and the spherical wrist base-frame.

Finally,

$$\mathbf{R}_3^0(\vartheta_1, \vartheta_2, \vartheta_3) = \mathbf{R}_1^0(\vartheta_1)\mathbf{R}_2^1(\vartheta_2)\mathbf{R}_3^2(\vartheta_3) \tag{3.28}$$

4. Compute $\mathbf{R}_6^3$

Since rotation matrices are orthogonal, the inverse equates to the transpose, thus $(\mathbf{R}_3^0)^T{=}(\mathbf{R}_3^0)^{-1}$ and

$$\mathbf{R}_6^3(\vartheta_4, \vartheta_5, \vartheta_6) = (\mathbf{R}_3^0)^T\mathbf{R}_e \tag{3.29}$$

5. Compute ϑ_4, ϑ_5, and ϑ_6

From Equation 3.29, the components of the rotation matrix are labeled as

$$\mathbf{R}_6^3 = \begin{bmatrix} n_x^3 & s_x^3 & a_x^3 \\ n_y^3 & s_y^3 & a_y^3 \\ n_z^3 & s_z^3 & a_z^3 \end{bmatrix} \tag{3.30}$$

For $\vartheta_5 = (0, \pi)$ corresponding to wrist-up

$$\vartheta_4 = Atan2(a_y^3, a_x^3) \tag{3.31}$$

$$\vartheta_5 = Atan2(\sqrt{(a_x^3)^2 + (a_y^3)^2}, a_z^3) \tag{3.32}$$

$$\vartheta_6 = Atan2(s_z^3, -n_z^3) \tag{3.33}$$

For $\vartheta_5 = (-\pi, 0)$ corresponding to wrist-down

$$\vartheta_4 = Atan2(-a_y^3, -a_x^3) \tag{3.34}$$

$$\vartheta_5 = Atan2(-\sqrt{(a_x^3)^2 + (a_y^3)^2}, a_z^3) \tag{3.35}$$

$$\vartheta_6 = Atan2(-s_z^3, n_z^3) \tag{3.36}$$

For MEDUSA, wrist-down is the desired solution.

3.2.3 Gantry and Peripheral Systems

Water Tank — The scan subject is immersed in a water tank at the center of the robotic arms. Due to the high manufacturing cost of large cylindrical castings, a hexagonal water tank was selected. The hexagonal tank is symmetric with 24 *in* side to side length and 18 *in* depth. allowing imaging of a healthy adult limb as dictated in the design parameters. The water tank is not affixed to the surrounding gantry and rests on a wheel pallet to permit removal of the tank from the system for draining and cleaning. Smaller/shallower water tanks can be exchanged for phantom or *ex-vivo* tissue imaging to conserve water and reduce weight during tank transfer.

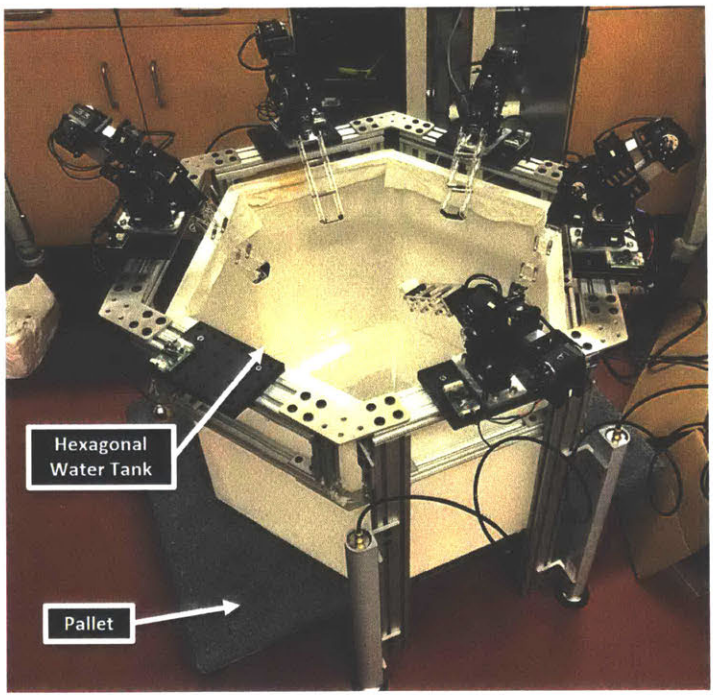

Figure 3-7: Water tank in the scanner gantry

Gantry — The six individual robotic manipulators discussed previously are mounted circumferentially around the water tank on an aluminum gantry. Shown in Figure 3-8, the gantry forms an hexagon around the water tank and the center of each side of the hexagon holds an arm (highlighted in orange). Cabling for each arm is routed through the frame to the power supply banks on the side. The full gantry is supported by 4 hydraulic linear actuators labeled in Figure 3-9 to adjust the gantry height to enable removal of the water tank at the center. The structure next to the hexagonal frame holds the supporting electronics and the hydraulic reservoir and motor.

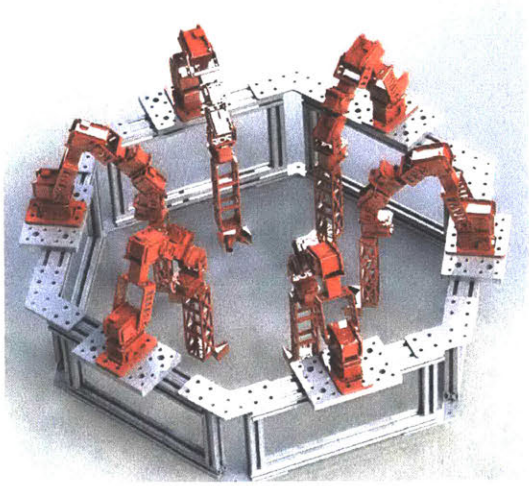

Figure 3-8: MEDUSA CAD of hexagonal frame

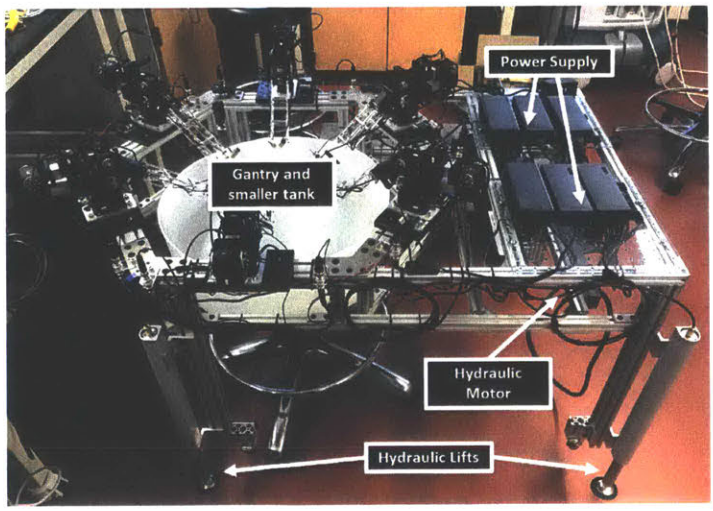

Figure 3-9: Full MEDUSA System

3.3 Data Acquisition and System Integration

3.3.1 Transducers

Transducers for MEDUSA follow designs from the previous single element system. For FWI and bone imaging, low frequency (500 kHz) were custom designed for MEDUSA. For tomographic imaging, spherically focused transducers transmit the acoustic wave while point transducers receive the propagating waves. Both transmitters (red) and receivers (blue) are shown in Figure 3-10. Unlike the previous fan beam transmitters, primarily designed for sliced imaging, MEDUSA transmitters are spherically focused to enable true 3D imaging.

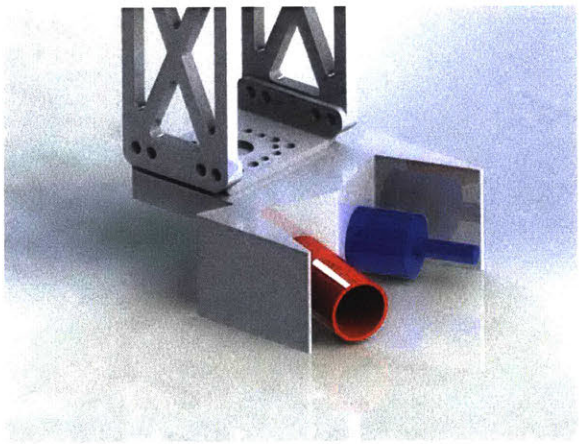

Figure 3-10: Spherically focused transmitter (red) and point receiver (blue)

With customizable end-effectors on each arm, arrays or other transducer designs can be attached and evaluated. For the scope of this these, imaging was completed using the 500 kHz transmitter and receiver set.

3.3.2 Cephasonics

A Cephasonics Cicada LX system drives the ultrasound transducers and records the measured waveforms. The system is a programmable ultrasound system with 64 transmit and receive channels and 3 way multi-plexing to drive larger arrays up to 192 elements. The system has bandwidths up to 40 *MHz* which can be leveraged to drive higher order transducer harmonics for high resolution imaging. For MEDUSA, 6 channels are active for pulse-echo imaging while 12 channels are active (6 transmit and 6 receive) for tomography. A custom 12 channel adapter board was made to connect single element transducers to the Cephasonics system. Arbitrary transmit and receive patterns can be programmed to enable mono-static (spatially co-located transmitter and receiver) and bi-static/tomographic (spatially separated transmitter and receiver) imaging. Photograph of the Cephasonics system and the custom designed transducer connector for MEDUSA is shown in Figure 3-11.

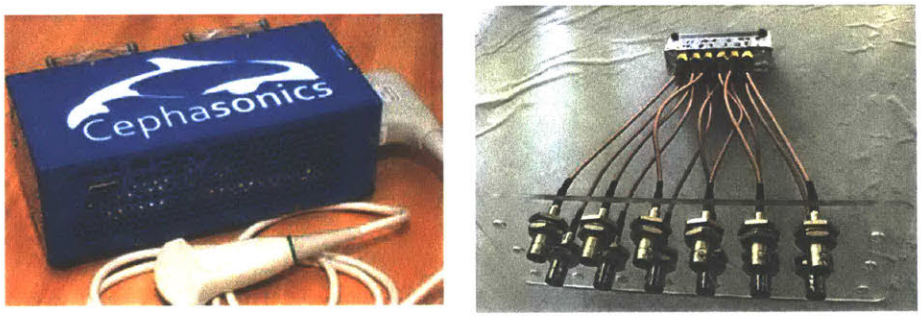

(a) Cephasonics Cicada LX

(b) Custom MEDUSA Connector

Figure 3-11: Programmable ultrasound system for MEDUSA

3.3.3 System Integration and Controls

Summarized high level system architecture is shown in Figure 3-12. The system is divided into three main levels: Imaging, Scan, and Servo. Each level is distributed to one of three physical systems: Host PC, Cephasonics, or Dynamixel controller.

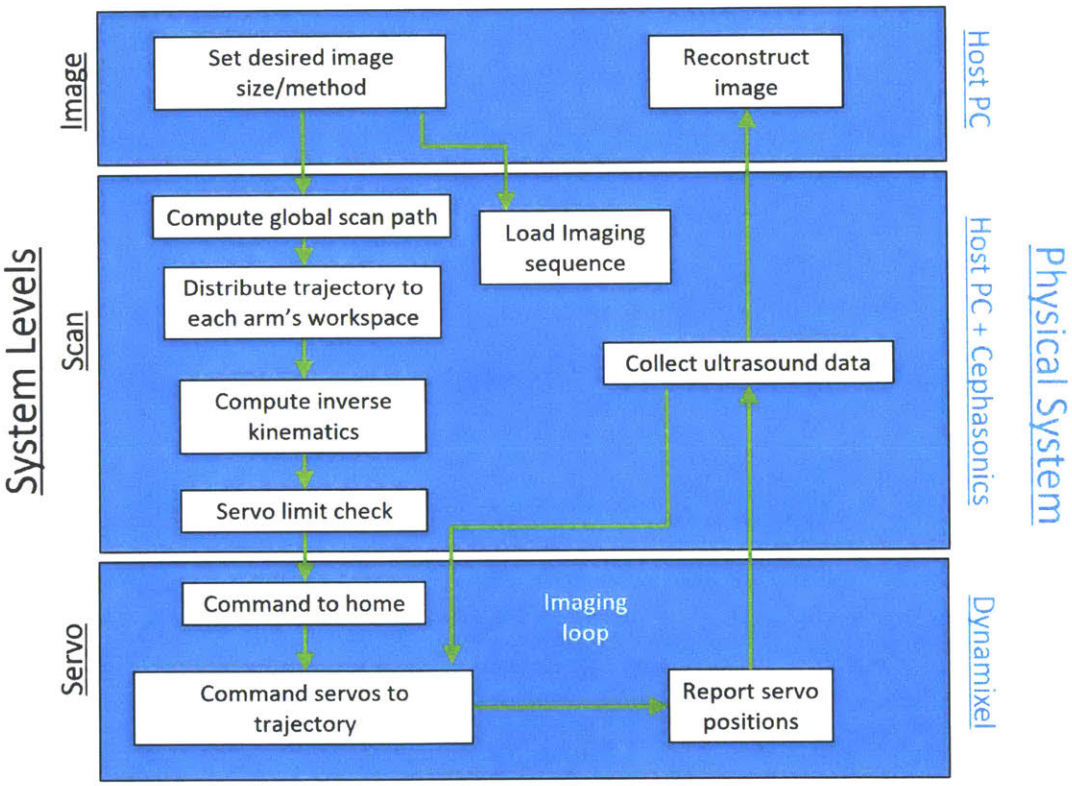

Figure 3-12: MEDUSA system block diagram

Imaging Level

The Imaging Level is the highest level in the system and directly interacts with the user on the Host PC. The user dictates the type of desired imaging method (pulse-echo, tomographic, 3D, etc) which determines transmit and receive sequences loaded to the Cephasonics and the path positions of the transducer during the scan. Once all data is collected and received from the Cephasonics, various algorithms can be implemented to reconstruct the image for viewing.

Scan Level

The Scan Level receives the desired imaging type and performs the necessary com-

putations and error checks to execute the imaging sequence. The Scan Level is distributed between the Host PC and Cephasonics for servo controls and data acquisition, respectively. Based on the desired imaging path points (labeled C in Figure 3-13) for the transducers, the spatial positioning and orientations are given as a set of (4×4) matrices in the global reference frame then distributed to each arm's workspace. Each distributed path segment initially reference the global reference frame (labeled A in Figure 3-13) at the center of system but are converted to reference each arm's base frames (labeled B in Figure 3-13) via 3D Homogeneous Transformation Matrices (HTMs). Once converted to reference the respective arm base frames, the path segments matrices are used in the inverse kinematics to compute the joint angles to satisfy scanning requirements. Once joint angles are computed, an error check verifies that all computed joint angles are within physical limits for each servo before any position commands are sent to the servo controller. A top-view and 3D view of the reference frames and example path points are shown in Figure 3-13.

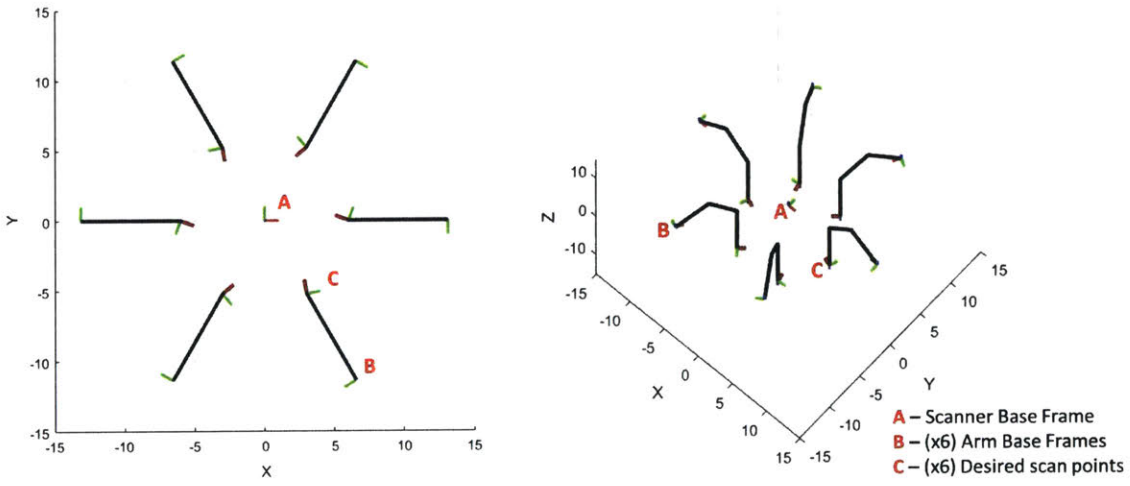

(a) Top View (b) 3D View

Figure 3-13: MEDUSA Kinematic Model

Ultrasound data acquisition sequences are pre-programmed based on desired imaging method. Pulse amplitude, transmit waveform, sampling frequency, and transmit/receive patterns are pre-programmed and loaded depending on the transducer

specifications and desired scan method. Once the ultrasound imaging sequence is loaded into Cephasonics and joint computations are verified, the Host PC commands an initialization sequence of the arms to reach "home" position then the first path point to begin imaging.

The imaging sequence communicates between the Host PC, Cephasonics, and servo controllers. For each path point, the Host PC sends new position commands to all the servo controllers. Once the new position is reached, the Host PC sends a software trigger to execute the imaging sequence on the Cephasonics to capture ultrasound data. After data capture, the Host PC records the waveforms and corresponding servo positions in memory then proceeds to the next position command and new data capture. Upon reaching the last path point and data capture, all ultrasound data is compiled along with the measured servo positions and saved to file on the Host PC.

Servo Level

The Servo Level is the lowest level in the system, existing solely on the individual servo controllers within each joint. Each Dynamixel servo controller is programmable in position control mode, velocity control mode, or open loop pulse-width modulation. Since transducer positioning feedback is critical for imaging in MEDUSA, all joints are operating in position control mode. Trajectory and PID parameters are tuned experimentally to maximize scan speed while minimizing jerk during travel from path point to path point. Since each Dynamixel has 193:1 (MX-28AT) or 200:1 (MX-64AT) gearing on the output, inertial disturbances felt by the control loop are reduced by by the gear ratio squared. In this control scheme, dynamic effects from moving inertial masses are treated as disturbances on each servo's position control loop. Gain values on each servo control loop are tuned to maximize disturbance rejection.

3.4 Mechanical Calibration

Positioning calibration for MEDUSA was completed using individual joint servo feedback and imaging of calibration objects of known size and geometry.

3.4.1 Arm Repeatability

Repeatability for MEDUSA was evaluated using reference trajectories typical of a MEDUSA scan. Servos received the same scan path commands for 27 iterations and the encoder values during each scan were recorded. The maximum and minimum recorded deviations are tabulated in Table 3.3. Servos are numbered sequentially from the base to the end-effector from 1 to 36, repeated on each arm. All servos had repeatability below 1° as measured by each joint encoder. By feeding the measured encoder values through the forward kinematics, the end-point repeatability for each MEDUSA arm is tabulated in Table 3.4. End point repeatability for all MEDUSA arms is below 3 *mm*, sufficient for imaging at the 500 *kHz* acoustic frequency.

S#	Re.(°)	S#	Re.(°)	S#	Re.(°)	S#	Re.(°)	S#	Re.(°)	S#	Re.(°)
1	±0.07	7	±0.07	13	±0.07	19	±0.09	25	±0.10	31	±0.16
2	±0.35	8	±0.34	14	±0.35	20	±0.30	26	±0.44	32	±0.28
3	±0.89	9	±0.07	15	±0.09	21	±0.22	27	±0.22	33	±0.26
4	±0.13	10	±0.07	16	±0.06	22	±0.06	28	±0.06	34	±0.06
5	±0.12	11	±0.06	17	±0.09	23	±0.18	29	±0.22	35	±0.26
6	±0.07	12	±0.06	18	±0.07	24	±0.09	30	±0.09	36	±0.12

Table 3.3: Servo joint repeatability

Arm Number	X *mm*	Y *mm*	Z *mm*
1 (S# 1-6)	±2.0	±.80	±0.9
2 (S# 7-12)	±2.2	±1.8	±1.8
3 (S# 13-18)	±2.1	±2.0	±1.5
4 (S# 19-24)	±1.8	±0.8	±0.1
5 (S# 25-30)	±1.9	±0.7	±0.8
6 (S# 31-36)	±1.8	±0.9	±0.8

Table 3.4: Servo end-point repeatability

3.4.2 Imaging Accuracy

The same reference trajectory for repeatability testing was used to pulse-echo image a 0.73 mm diameter steel wire placed inside the tank.

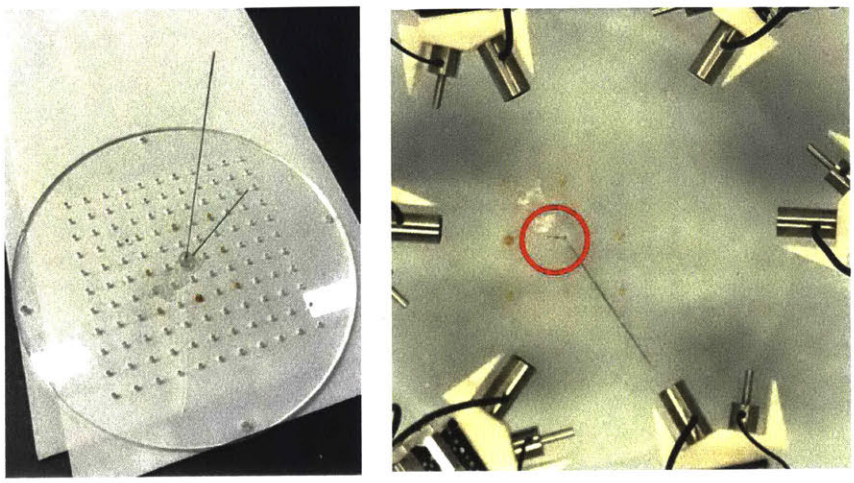

(a) Calibration steel wire (b) Wire during calibration

Figure 3-14: Acoustic calibration using wire target

If all arm end point positions are accurate in the system global reference frame, image reconstruction using the recorded joint positions should reconstruct a point source within the image domain. However, using the measured positions, the resulting pulse-echo image presents significant errors. An incoherent point source is seen in the reconstructed image in Figure 3-15, where a single point is expected.

Since the unrepeatable mechanical errors presented in Section 3.4.1 should be sufficient for imaging, there are repeatable errors in the system that can be calibrated and corrected prior to image reconstruction. Repeatable errors are likely due to system errors on: servo joint assembly, position and orientation mounting of each base servo, physical transducer geometry, and electronic delays in acoustic transmission and measurement. Given the system complexity and the large set of parameters to calibrate, a data driven calibration scheme was developed to identify the necessary calibration parameters.

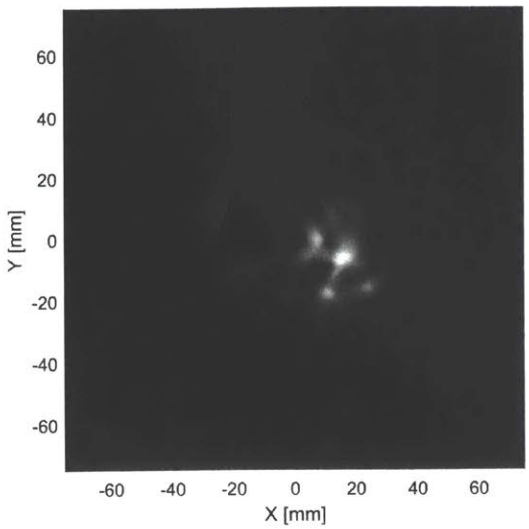

Figure 3-15: Pulse-echo reconstruction of the calibration wire

3.5 Data Driven Calibration

Incorporating all mechanical and electronic sources, there are over 100 parameters to calibrated for MEDUSA. Exhaustively calibrating each parameter individually would be intractable and infeasible due to the non-linear transformations between the input and output kinematic relations. Similar to typical methods used in robotics such as touching off calibration objects or imaging of reference checkerboards, similar parameter optimization techniques can be applied in MEDUSA using ultrasound data [2]. Data driven calibration in MEDUSA uses an optimization scheme that minimizes error between expected images versus measured images on calibration objects of known size the geometry (wires). The optimization uses measured ultrasound travel time data to update the kinematic models to correctly reconstruct calibration objects.

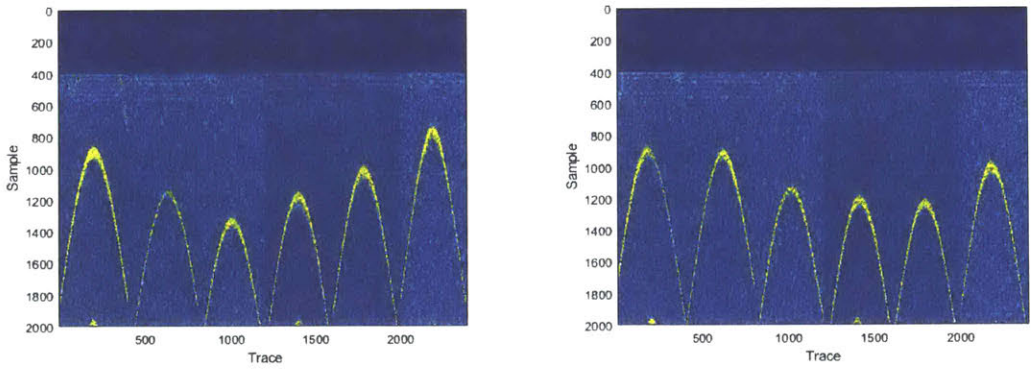

(a) Wire data #9 (b) Wire data #20

Figure 3-16: Raw channel data from two wire calibrations

To reduce system complexity, imaging was restricted to a horizontal plane and the elbow joint was locked during imaging. Each arm traces a circle centered around the respective base servo while the transducer is oriented facing the center of the tank. This reduces the total number of parameters to 36 (6 on each arm). A single steel wire was used again as the calibration target. The wire was placed at 27 random locations within the tank and a pulse-echo scan using the same scan trajectory was completed for each wire position. Within each scan, the acoustic travel time of the echo corresponds to the distance of the wire from the transducer. As the transducer

moves during each scan, the echo travel time from the wire will change. Figure 3-16 shows the raw data from two different scans with the wire moved to different positions between scans. When reconstructed in the global reference frame, each scan should reconstruct a single point. With multiple scans using the same trajectory but different wire positions, the optimization scheme poses the question: what must the calibrated parameters in the forward model be such that all computed transducer positions from the forward kinematics reconstruct a point for every wire scan?

The optimization scheme is summarized in the Hill Climber algorithm in Algorithm 1. The optimization model $\mathbf{m}_0$ initially assumes that all wires are at the center of the tank. The forward kinematics computes the transducer positions using initial guesses of the calibration parameters based on physical models. Distance between the assumed wire positions and each computed transducer position are compared against the measured travel distance of ultrasound echos. Differences between the model distances and the echo travel distances are summed as the score term l_* being minimized in the optimization. Updates for the calibration parameters are computed as model perturbations and are selected based on reduction of the error term for each proposed perturbation.

Algorithm 1 Hill Climber

Initialize starting model: $\mathbf{m}_0$
Select proposal covariance (step-size): $\mathbf{C}$
for $i = 1$ to maximum iterations **do**
  $\mathbf{n} \leftarrow \text{Normal}(0, \mathbf{C})$ proposed model perturbation
  $\mathbf{m}_* \leftarrow \mathbf{m}_{i-1} + \mathbf{n}$
  $l_* \leftarrow L(\mathbf{m}_*)$ proposed model score
  if $l_* > l_{i-1}$ **then**
    $\mathbf{m}_i \leftarrow \mathbf{m}_*$
  else
    $\mathbf{m}_i \leftarrow \mathbf{m}_{i-1}$
  end if
end for

With calibrated parameters, the forward kinematics computes the corrected transducer positions. Wire calibration images then correctly reproduces a point. As seen in Figure 3-17a and 3-17b, the previously incoherent point source from a wire scan is

corrected into a single point. Superimposing all 27 reconstructed wire images using the calibrated parameters in the forward kinematics shows correctly reconstructed point sources for all wire positions. Points on the extremity are less coherent due to the wire being on the edge of the scan aperture and echoes are weaker for more distant transducer positions.

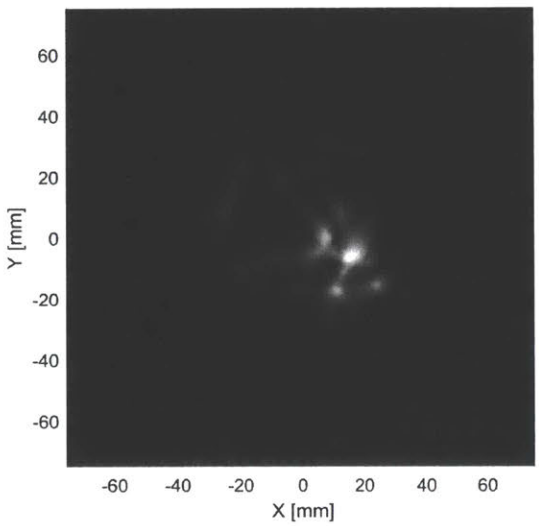

(a) Wire pre-calibration

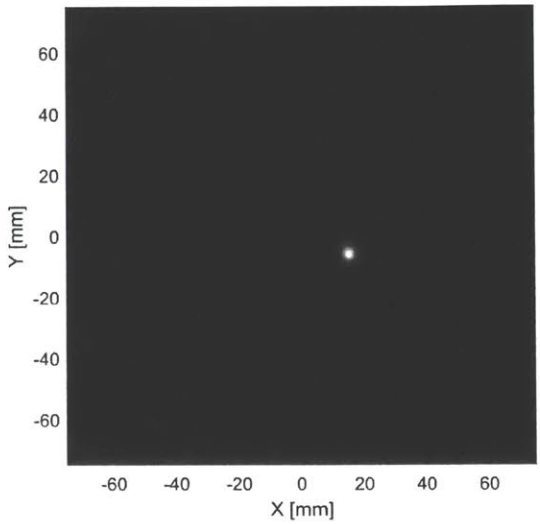

(b) Wire post-calibration

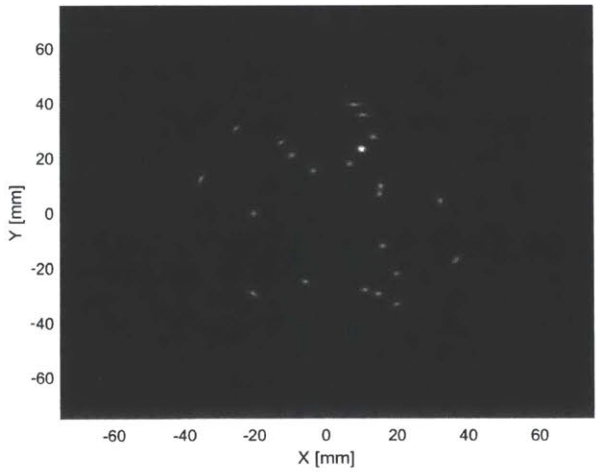

(c) Multiple calibration wires superimposed

Figure 3-17: Calibrated wire images

3.6 Acoustic Safety Calibration

All feasible acoustic transducers for use in MEDUSA were calibrated to ensure safety for human subject imaging. Maximum possible acoustic outputs for each transducer was measured with a hydrophone (ONDA HGL-0200) calibration apparatus shown in Figure 3-18.

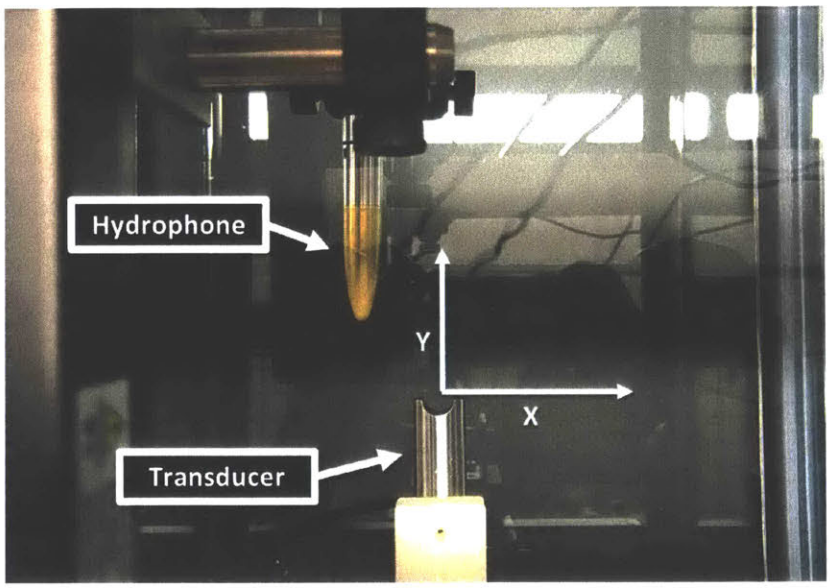

Figure 3-18: Scanning setup for acoustic safety calibrations

The hydrophone has calibrated sensitivity from 0.25 to 20 *MHz*. XY positioning of the hydrophone using two linear translation stages mapped the wavefield of the 0.5, 1, 2.25, and 5 *MHz* single element transducers at maximum transmit power, in addition to the Cephasonics linear array. The linear array was focused at 2 *cm* with all elements active at maximum transmit power to quantify maximum possible acoustic exposure; all other transmit settings on the linear array will have lower acoustic power. Positioning resolution of 1 *mm* was used for coarse mapping of the wavefield and fine resolution mapping with 0.25 *mm* was used around the focal point to measure the maximum acoustic output. Pulses received at each position by the hydrophone was time integrated to compute the derated spatial-peak temporal-average intensity ($I_{spta.3}$) at each spatial position. Measured wavefields are shown in Figure 3-19 with log plots to view the wavefield in 3D isometric view. All measured fields were within

the acoustic safety limits of 720 mW/cm^2 for peripheral vessel ultrasound exposure as dictated by the FDA [87].

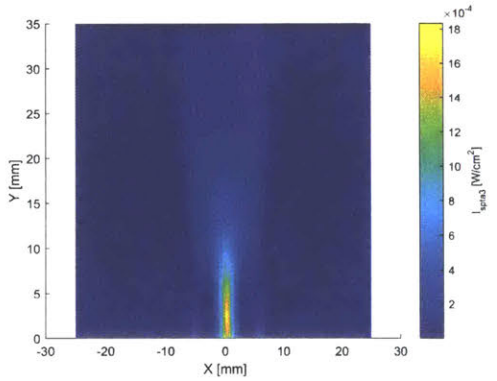

(a) 500 kHz (top)

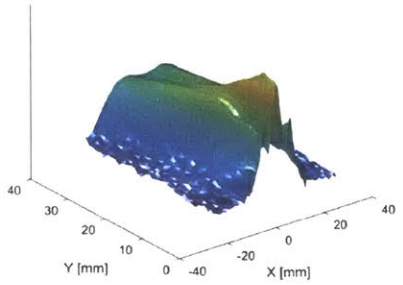

(b) 500 kHz (iso)

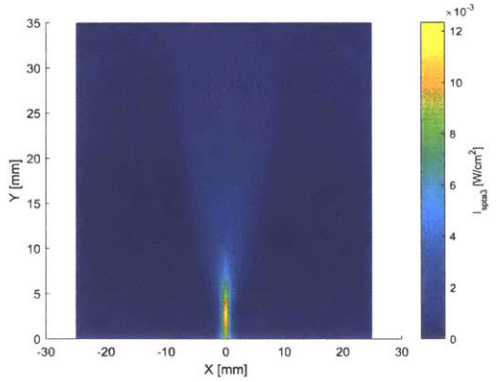

(c) 1 MHz (top)

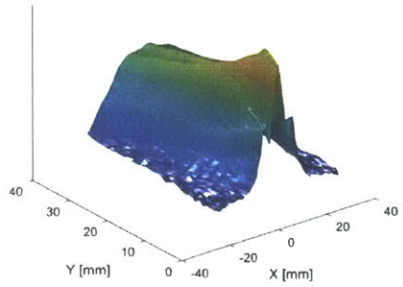

(d) 1 MHz (iso)

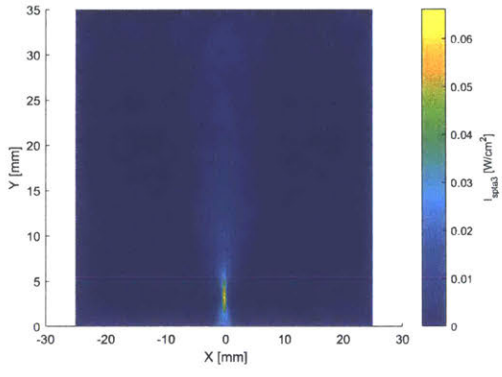

(e) 2.25 MHz (top)

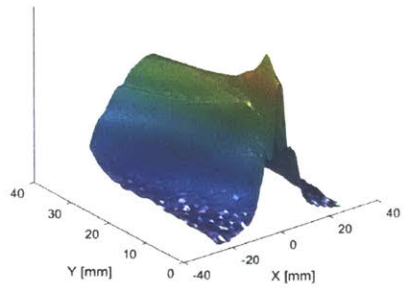

(f) 2.25 MHz (iso)

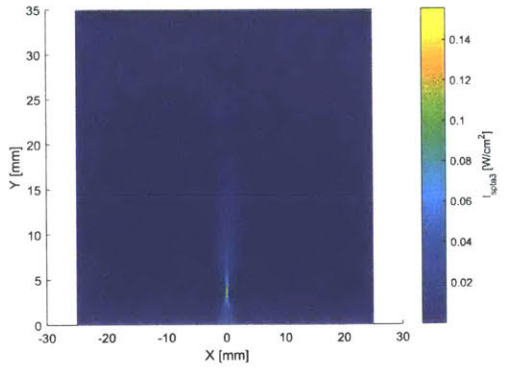

(g) 5 *MHz* (top)

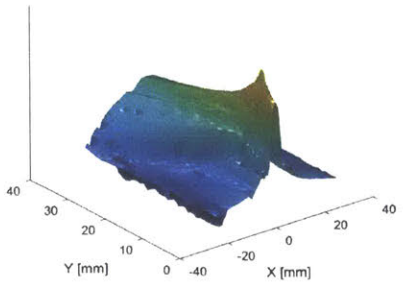

(h) 5 *MHz* (iso)

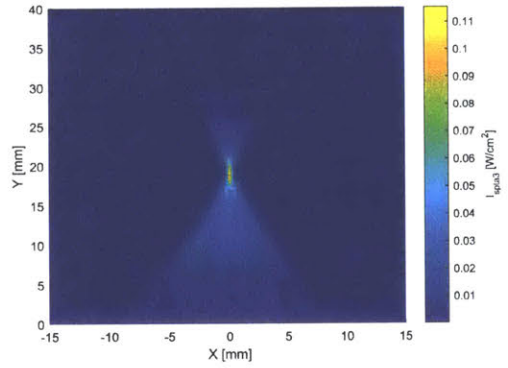

(i) Focused Linear Cephasonics Array 5 *MHz* (top)

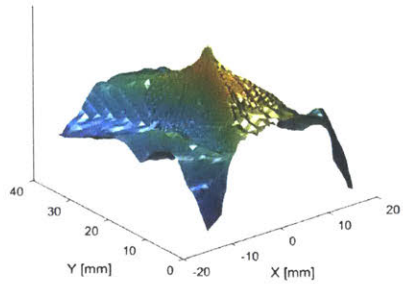

(j) Focused Linear Cephasonics Array 5 *MHz* (iso)

Figure 3-19: Acoustic safety calibrations

3.7 Imaging

With the mechanical system parameters calibrated, mono-static, bi-static, and tomographic imaging was completed on various objects using MEDUSA. In mono-static (pulse-echo) imaging, the ultrasound transmitter and receiver are spatially co-located; typically the same physical transducer. In bi-static imaging, the transmitter and receiver are spatially separated. Bi-static imaging better captures reflections from specular surfaces such as bone, where reflected waves do not necessarily return to the transmitter location. By having multiple transducers, pulse-echo imaging in MEDUSA captures bi-static data from one transducer to every other transducer, producing 6 times the amount of data in comparison to pulse-echo imaging on the previous single element system. Tomographic imaging on MEDUSA is similar to tomographic imaging on the previous single element system. The transmitter is fixed while receivers are moving on the opposing side. With multiple arms, the receiver aperture is broken into segments distributed to the workspace of each arm. Imaging results using each scan method on various objects are presented in the following subsections.

Representative of bone in sound speed, a 1 *in* diameter nylon rod was imaged in the tank using the calibrated trajectory. Subject forearms were also imaged in the tank following the same procedure. For each mono-static and bi-static scan, 1200 total transducer positions were used to circumferentially scan each subject. At each scan position, the transmitting transducer captures a pulse-echo line (mono-static) while the other 5 transducers captures the refracted waves (bi-static). 20 averaging instances was used at each scan position to reduce electrical noise due to pulse-width-modulation (PWM) in the servomotors. All transducers were operating at 500 *kHz*. The transmit signal consists of a 3 cycle sine wave, time gated by a Tukey (tapered cosine) window with r=0.6 to limit side-lobes. The sampling frequency for the analog to digital converter in the Cephasonics was set to 10 *MHz*; the analog anti-aliasing filter was set to 3 *MHz*; the analog highpass filter was set to 0.1 *MHz* to remove low frequency noise and DC bias. Sampled waveforms were filtered in post-processing with

a band-pass filter covering frequencies between 200 kHz and 800 kHz. Depending on the desired reconstruction method, the data is sorted for mono-static or bi-static migrations. Reconstructed images for the nylon rod and forearm are shown in the following subsections.

3.7.1 Mono-Static (Pulse-Echo) Imaging

For pulse-echo imaging, only mono-static data from the transmitting transducer was used for reconstruction. Photograph of the nylon rod and the subject forearm are shown in Figure 3-20a and 3-20c, respectively.

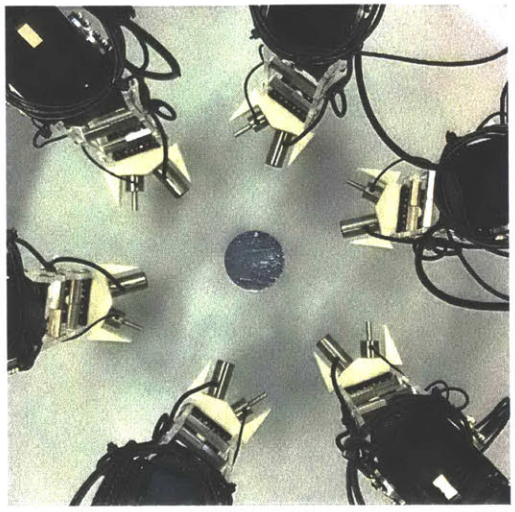

(a) Nylon rod scan

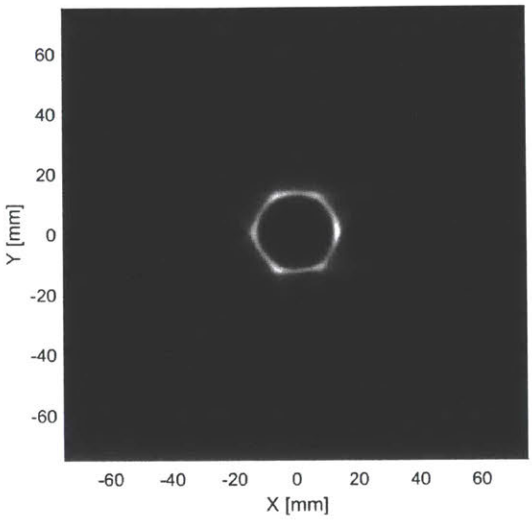

(b) Mono-static rod image

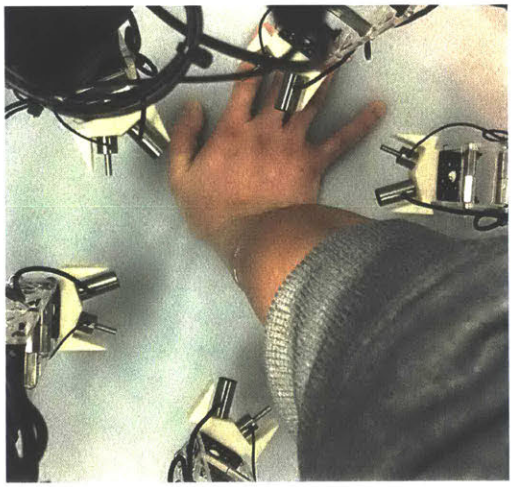

(c) Forearm scan

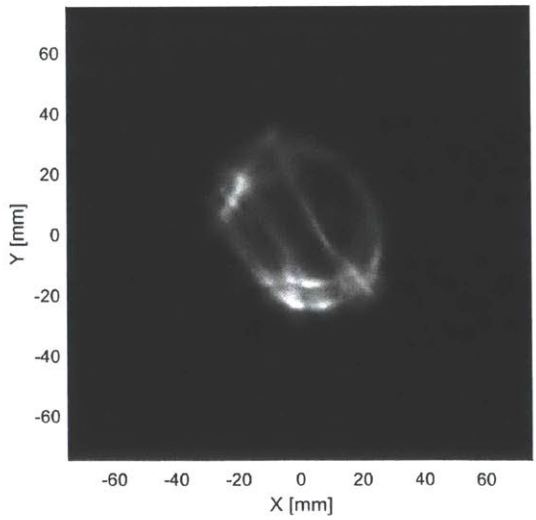

(d) Mono-static forearm image

Figure 3-20: MEDUSA mono-static scans

Migrated image of the nylon rod looks hexagonal instead of circular due to the specularity of the rod. Similar artifacts are present in the forearm image due to the bone, obscuring features in the soft-tissue regions.

3.7.2 Bi-Static Imaging

Bi-static imaging uses both mono-static and the refracted data collected on the other transducers. With 6 transducers, MEDUSA can collect bi-static data simultaneously with mono-static data. Bi-static migrations improves imaging for specular objects such as the nylon rod and bones. Migration reconstructions using bi-static data of previous scans shown in Figure 3-20 is shown in Figure 3-21.

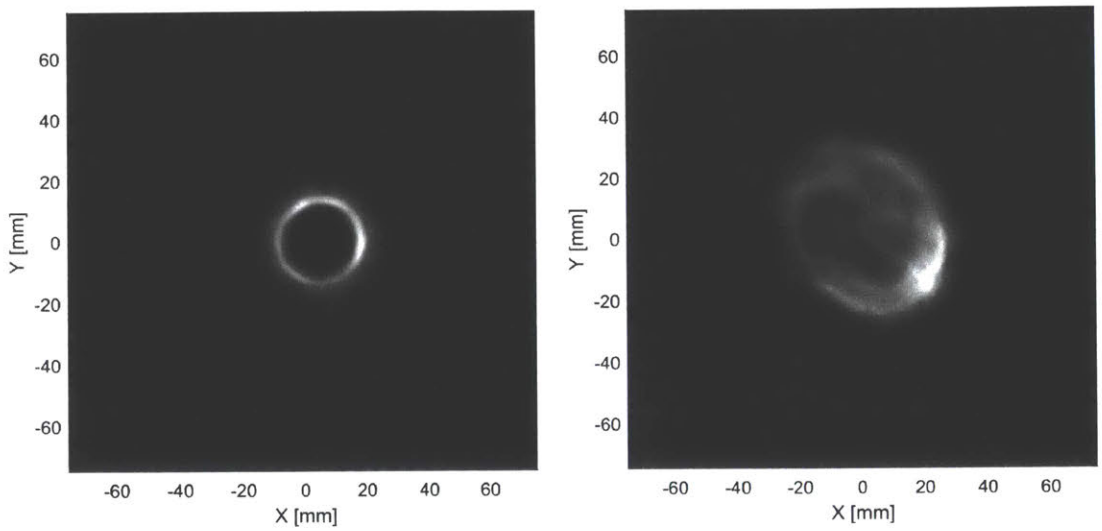

(a) Bi-static rod image

(b) Bi-static forearm image

Figure 3-21: MEDUSA bi-static images

Reconstruction using bi-static data improves boundary features. The rod is circular, without the hexagonal geometry of the mono-static image and the bone boundaries are refined on the forearm with less artifacts surrounding the region. Bone boundaries between the radius and ulna are obscured and is likely due to one bone obscuring the reflected wave from the other. Furthermore, muscle features are clearer in the bi-static image. Overall, the image quality is improved by using bi-static imaging at 500 kHz, a capability previously absent in the single element system.

3.7.3 Tomographic Imaging

Preliminary tomographic data acquisitions using MEDUSA is currently being evaluated. Acoustic transmits from spherically focused transducers were captured by the point transducers (both shown in Figure 3-10). For transmit, 18 instances surround the scan subject at 6 evenly spaced angular positions (0° 60° 120° 180° 240° 300°). At each position, the transmitter's heading is rotated between -10° 0° and 10° to increase the total transmit beam-width for improved transmit coverage. For each of the 18 transmit instances, 1000 receive instances were captured, each receive instance used 20 averages to improve the signal-to-noise ratio. Transducer trajectories follow the previously calibrated pulse-echo trajectories with 1 transducer fixed as the transmitter. Tomographic scans on tissue mimicking objects without hard inclusions (hot dogs, fruits/vegetables) have been completed. FWI presented in Chapter 2 was adapted to the MEDUSA scan geometry, inversion results for the hot dog is shown in Figure 3-22, color bar units are in m/s.

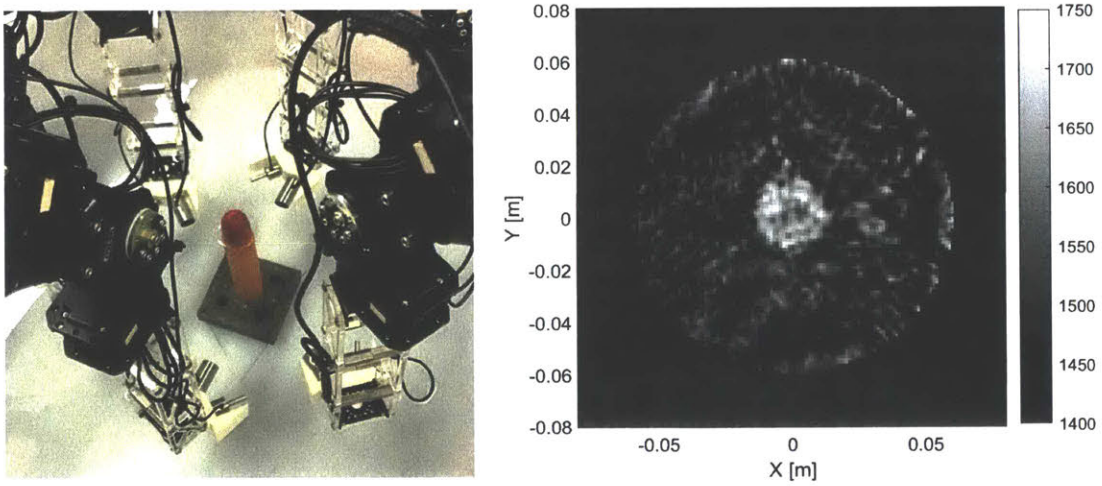

(a) Tomographic scan

(b) FWI Inversion

Figure 3-22: MEDUSA tomographic scans

FWI inversions successfully recovers the sound speed of the hot dog as 1700-1750 m/s which is near the measured value of 1740 m/s (measured via through transmission). Spatially, FWI shows a $\sim$2 cm diameter region of higher sound speed which matches the measured 2.07 cm diameter of the hot dog sample. FWI results

verifies MEDUSA capabilities for quantitative imaging. With further improvements in data acquisition rate, *in-vivo* quantitative imaging of human subjects using FWI could be achieved.

Due to the averaging due to electrical noise, the total time for the tomographic scan was 40 minutes which is above the 10 minute total scan time requirement in the functional requirements. Relative to the single element system, total tomographic imaging time on MEDUSA is still comparable. However, MEDUSA scans can be completed with a single operator with minimal supervision. Improvements in scan speed can be made by adaptively imaging the subject by avoiding transmit/receive positions that do not further constrain the inversion problem. Identifying critical features and deriving the optimized scan methods from prior models is similar to current robotics research in path planning but has not been explored in medical imaging. Furthermore, small arrays could replace the single elements currently used on each MEDUSA arm to reduce noise and further decrease scan times. Mono/Bi-static imaging and FWI inversions demonstrate that MEDUSA has sufficient mechanical performance capabilities for geometric and quantitative imaging. FWI should be adapted for MEDUSA to quantify soft-tissue and bone speed of sound in human subjects.

3.8 Summary

MEDUSA improves on the single element system by adding more transducers and enabling full free space positioning of each transducer. The robotic positioning system integrated with a programmable ultrasound system allows new acquisition geometries to be evaluated. MEDUSA system calibrations ensure accurate transducer positioning and safe acoustic exposure for human subject testing.

Calibration of mechanical parameters using data driven optimization techniques corrected the forward kinematic model to generate accurate end-point positions for image reconstruction. Using the corrected forward kinematics, MEDUSA has sufficient positioning accuracy for pulse-echo and tomographic imaging. By having multiple transducers, MEDUSA collects bi-static data that improves reconstruction of

specular reflections typical of imaging in bone. Image reconstruction using bi-static data improves continuity of specular boundaries seen from bone surface reflections. In tomographic scanning, MEDUSA captures similar data sets compared to the previous single element system with improved automation and capture rates. Further improvements in scan rate can be explored by attaching an ultrasound array on each MEDUSA arm.

Beyond what is presented in this chapter, there are multiple untapped capabilities of MEDUSA that could be explored in the future. With full 6 degrees of freedom positioning flexibility on all transmitters and receivers, MEDUSA could adaptively image a target and minimize the number of data capture instances while preserving image quality after reconstruction. Presently, data acquisition techniques exhaustively images a target without intelligent focus on particular regions of interest. If features can be actively identified during data acquisition, MEDUSA could adapt subsequent data acquisitions to more efficiently image specific regions of interest. This adaptive imaging method is typically used in camera based imaging and has not been explored in ultrasound imaging. Quantifying ultrasound image quality and guiding subsequent data acquisitions to reduce the total uncertainty in the region of interest is largely unexplored field in medical imaging and is a unique capability of MEDUSA for future research.

Chapter 4

LUS - Phenomenology

Full non-contact laser ultrasound (LUS) imaging has several distinct advantages over current medical ultrasound (US) technologies: elimination of coupling mediums (gel/water), operator-independent image quality, improved repeatability, and volumetric imaging. Current light-based ultrasound utilizing tissue penetrating photoacoustics (PA) generally uses traditional piezoelectric transducers in contact with the imaged tissue or carries an optical fiber detector close to the imaging site for detection. Unlike PA, LUS specifically restricts optical to acoustic energy transduction at the tissue surface, maximizing the generated acoustic source amplitude. In combination with optical interferometry, any exposed tissue surface is a viable acoustic source and detector. LUS operates analogous to conventional ultrasound but using light instead of piezoelectric elements. This thesis presents full non-contact LUS results, imaging subjects at $\sim$5 *cm* depths and at meter scale standoff from the target surface. Experimental results demonstrating volumetric images and first LUS images on human subjects are presented, all at eye and skin safe optical exposure levels. Progression of LUS imaging from tissue-mimicking phantoms, excised animal tissue, to humans in-vivo are presented, with validation from conventional ultrasound images. LUS system design insights and results presented in this thesis inspire further LUS development and is a significant step toward clinical implementation of LUS.

4.1 The Photoacoustic Effect

The first reported instance of the photoacoustic (PA) effect date back to 1880 by Alexander Graham Bell [88]. Bell reported that sound waves can be produced when a solid sample is illuminated. Bell correctly surmised that the acoustic wave is produced by a thermo-mechanical effect when the optical energy is absorbed by the sample; he later demonstrated this effect in gases and liquids at varying wavelengths of light. Bell initially proposed the used of PA for spectral identification but the idea was abandoned due to the lack of acoustic sensors at the time other than human hearing. PA would not see application until nearly a century later with the development of high powered optical sources and highly sensitive acoustic transducers [89].

4.2 Photoacoustic Imaging vs. Laser Ultrasound

PA development for medical imaging was rather limited until the recent few decades [88, 90–92]. PA methods utilizing conversion of optical energy to acoustic energy via thermo-elastic expansion of the tissue offers a pathway toward non-contact and coupling agent free ultrasound imaging [93, 94]. PA is currently an active research area and commercial implementations have been recently developed [91, 92, 95, 96]. Multi-dimensional embodiments of PA using multi-wavelength, multi-point, and multi-contrast have been utilized to image length-scales spanning microns to centimeters [91, 92, 95, 97]. Generally, PA imaging systems are based on optical excitation of acoustic sources within the tissue and traditional piezoelectric detection of acoustic waves outside the tissue. Nanosecond pulsed lasers irradiating biological tissue generate acoustic impulses via optical absorption and induce thermo-elastic stress and relaxation within the tissue [70,98]. In PA, wavelengths that penetrate into the tissue are used and generate acoustic waves beneath the tissue surface [91, 92, 95, 97]. By tuning the optical wavelength, varying photosensitive absorbers in biological tissue can be selectively imaged [97]. To increase image quality or imaging depth, optical contrast agents such as nanoparticles or dyes can also be injected [95, 99, 100]. Since

PA signal generation is target specific, the spatial location of the optical to acoustic conversion point within the tissue can only be localized *a posteriori*. Depending on the irradiating optical beam, time inversion of multiple recorded acoustic signals may be necessary to localize the source position to reconstruct a PA image [101–103].

PA imaging depth and resolution are specific to the imaged object and application - dictated by the interaction of the specific light source and the tissue of interest; thus, optical parameters such as wavelength, power, geometric focus, and repetition rate are critical in PA system design [70]. Depending on the imaging application and optical components involved, PA image depths can range from microns to centimeters, with resolution ranging from sub-microns to millimeters [91,92,95,99]. For detection, the majority of PA implementations utilize piezoelectric elements placed in contact with the tissue surface with ultrasound gel or coupled through water [91, 92, 95, 97]. Few optical receivers for US detection have been evaluated on engineered tissue samples and show promise for implementation in a fully optical PA system; but optical detection of ultrasound on humans in-vivo has not been previously demonstrated [103–106].

In contrast to current PA systems, LUS specifically converts optical energy to acoustic energy at the body/skin surface, minimizing the effects of optical attenuation in tissue while maximizing acoustic energy output and ultrasound imaging depth. PA sources suffer from the high optical attenuation of biological tissue as the light travels through the tissue before conversion into an acoustic wave at the optical absorber [94]. By restricting PA conversion to the tissue surface, LUS sources eliminates optical attenuation within the tissue, maximizing the quantity of optical energy that is converted to acoustic energy. Since the acoustic attenuation of biological tissue is two orders of magnitude smaller than the optical attenuation, acoustic propagation within the tissue is more efficient than optical propagation, enabling deeper anatomical imaging with LUS.

Furthermore, the spatial location of the LUS source in the tissue can be known *a priori*, removing the need for multi-point detection and time inversion algorithms to localize the optical source position and amplitude. In combination with inter-

ferometric optical detection, LUS can replicate conventional probe-based ultrasound imaging without any patient contact. Optical detection also offers increased sensitivity, broader bandwidth, more compact packaging, and true non-contact measurements [107–114]. Since PA conversion varies depending on the illuminated tissue and is subject to patient safety limits (for human imaging), development of a fully non-contact LUS system for clinical anatomical imaging requires design analysis of light and human tissue interactions, to attain centimeter scale imaging depths at eye and skin safe optical exposure levels. With appropriate optical design and tuning, LUS is able to convert any tissue surface into an ultrasonic source and detector. LUS is analogous to conventional ultrasound with each piezoelectric element replaced by an optical source/detector point. Free-space positioning of the optical source and detector points enables volumetric LUS imaging without use of large and costly piezoelectric arrays.

4.3 Laser Ultrasound Source Physics

To generate LUS source signals suitable for ultrasound imaging, **optical**, **thermal**, and **acoustic** conditions must be satisfied. The generated LUS source must be restricted to the tissue surface and the acoustic wavelength should be in the *MHz* range for medical imaging. An overview of the full non-contact LUS is shown in Figure 4-1.

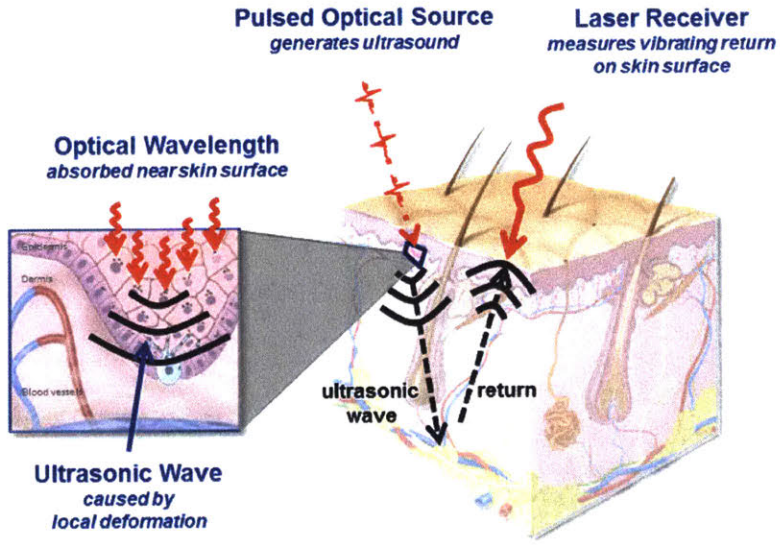

Figure 4-1: Schematic overview of non-contact laser ultrasound

Optical Condition — The optical condition stated in Equation 4.1 dictates the optical penetration depth of the light into the target. For a given optical intensity U_0 (W/m^2) impinging on the target, optical intensity at depth z (m) below the surface is given by U (W/m^2). The optical scattering coefficient μ_s (m^{-1}) within the tissue and the optical absorption coefficient μ_s (m^{-1}) summed dictate the exponential decay rate of the light intensity in the subject. In practice, the two optical coefficient are often measured as a lumped parameter and reported as one value [115]. Furthermore, the inverse of the summed optical coefficient is termed the characteristic penetration depth l (m) of the LUS source shown in Equation 4.2.

$$U = U_0 e^{-z(\mu_s + \mu_a)} \tag{4.1}$$

$$l = (\mu_s + \mu_a)^{-1} \tag{4.2}$$

Optical wavelengths greater than 1400 nm absorbed in biological tissue corresponds to a characteristic depth $l < 1$ mm. The depth l in conjunction with the impinging laser spot diameter a can be viewed as an equivalent acoustic element of the same geometric dimensions, meaning the LUS heated region can be approximated as disk transducer with diameter a at the tissue surface. For $l < 1$ mm, the corresponding acoustic frequency is on the MHz scale, appropriate for medical imaging [116, 117].

Thermal Condition — The thermal condition compares the heat conduction within the material to the heating rate due to the optical source. By analyzing the heat equation, the relation in Equation 4.3 can be derived.

$$\tau \ll l_{min}^2 \rho C_p / \kappa \tag{4.3}$$

where l_{min} (m) is the smaller of l or a, ρ (kg/m^3) is material density, C_p is the specific heat $(J/kg\text{-}K)$, κ $(W/m\text{-}K)$ is the thermal conductivity, and τ (s) is the laser pulse length.

This thermal condition means that the time action of the heating source must be significantly shorter than the heat conduction away from region, confining the energy within th heated region. This allows for the assumption of instantaneous heating in the tissue and confines the timescale of the optical source to be on the ns scale. The instantaneous heating generates the mechanical action and the resultant localized stress for producing an acoustic source.

Acoustic Condition — The acoustic condition is a restriction on dissipation of mechanical energy. Equation 4.4 describes the "stress confinement" condition within the tissue to trap the mechanical energy at the heated region.

$$\tau \ll l_{min}/c \tag{4.4}$$

where c (m/s) is the speed of sound in the material.

Physically, Equation 4.4 states that the rate of mechanical energy dissipation away from the heated region must be smaller than the rate of thermal mechanical expansion of the heated region. For biological tissue, speed of sound is around 1500 m/s. For a given heated region ($<$1 mm), the optical source must be shorter than 600 μs.

If all conditions are satisfied, the frequency domain expression shown in Equation 4.5 can be written to describe an LUS wave in pure water with a smooth surface generated by an rectangular optical pulse. The inverse Fourier transform of Equation 4.5 yields the time domain LUS waveform.

$$P_s(\omega) = \frac{iU_0\beta a^2}{2C_p}\frac{e^{ikR}}{R}\frac{\mu_a k cos(\theta)}{\mu_a^2 + k^2 cos^2(\theta)}e^{-\frac{a^2k^2sin(\theta)}{4}} \tag{4.5}$$

where ω is the radian frequency, i is the imaginary unit, R (m) is the range from the source to a spatial point, β (K^{-1})is the coefficient of thermal expansion, θ is the angle from the source to the spatial point, and k is the acoustic wave number defined as $k = 2\pi/\lambda$, where λ is the acoustic wavelength.

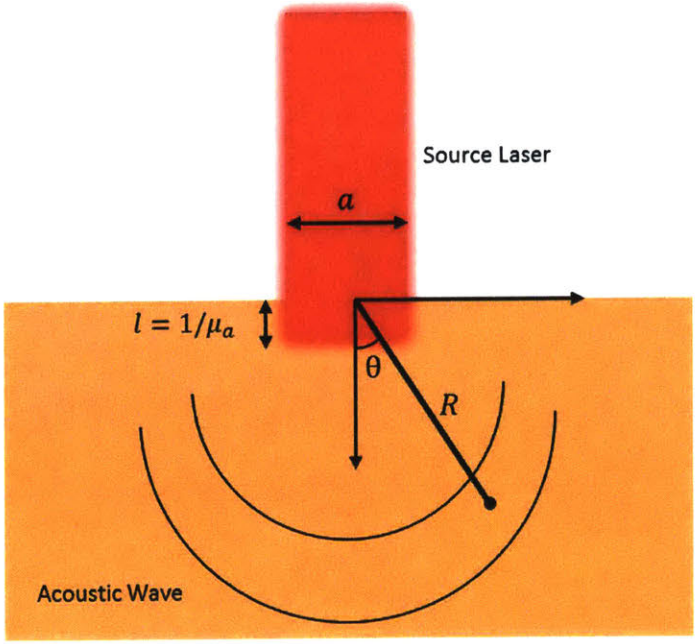

Figure 4-2: Diagram of Equation 4.5

In aggregate, optical and thermodynamic terms define the LUS waveform and spa-

tial terms define the wavefield. For biological tissue, Equation 4.5 is valid for optical wavelengths between 800-2000 *nm*. The majority of the physical terms in Equation 4.5 are parameters intrinsic to the irradiated object, which are fully defined by its material properties. More precisely, the only tunable LUS design parameters from Equation 4.5 are U_0, a, and μ_a . Optical intensity U_0 for a given spot size a is regulated by the ANSI safety limits depending on the tissue type and irradiating optical wavelength [118]. Furthermore, for each material, the optical absorption coefficient μ_a is also a function of the irradiating optical wavelength. Thus, the proper selection of the optical source wavelength is the critical parameter for LUS system design.

Looking closer at Equation 4.5, assuming broad-side transmission ($\theta = 0$), Equation 4.6 can be extracted.

$$EF = \frac{\mu_a k}{\mu_a^2 + k^2} \tag{4.6}$$

where EF is a unitless efficiency factor that describes the optical to acoustic conversion efficiency, scaling the amplitude of the LUS source as a function of acoustic frequency. Within the term, the optical absorption term μ_a modulates the source spectrum and has a significant impact on the conversion efficiency. Equation 4.6 is maximized when $\mu_a = k$. Physically, this means the characteristic optical penetration depth l into the tissue should match (with a factor of 2π) the acoustic wavelength being generated, since $l = 1/\mu_a$ and $k = 2\pi/\lambda$.

4.3.1 Roughness and Attenuation

Surface Roughness — In practice, LUS sources on biological tissue will be negatively impacted by the surface roughness of the skin surface. LUS waveform generated on a rough surface with Gaussian distribution of roughness heights is given by Equation 4.7 [70].

$$P_r(\omega) = P_s(\omega)e^{-\frac{\sigma^2 k^2 cos^2(\theta)}{2}} \tag{4.7}$$

where σ (m) is the mean square height of the roughness.

LUS signal degredation can be significant due to increased surface roughness. For optical and acoustic parameter typical of biological tissue, a surface roughness with σ =0.001 m results in a 5 dB attenuation at 2.5 MHz [79].

Acoustic Attenuation — In biological tissue, acoustic attenuation α is dependent on the tissue type and the wavelength of the acoustic wave. Acoustic attenuation is due to heating and scattering within the tissue and range from 0.5-2 *dB/cm-MHz* for humans and 2-3 *dB/cm-MHz* for bovine tissue [119,120]. Equation 4.8, describes the exponential decay of an acoustic wave due to acoustic attenuation.

$$A(z,\omega) = A_0 10^{-\frac{\alpha z \omega}{40\pi}} \tag{4.8}$$

where A_0 (Pa) is the initial pressure amplitude.

Equation 4.8 limits the maximum imaging depth in tissue for any acoustic imaging method and is not limited to converted optical sources. Typical medical ultrasound is also restricted by Equation 4.8. High frequency piezoelectric transducers are severely attenuated in biological tissue, limiting maximum imaging depth in high frequency ultrasound imaging.

4.4 Optical Wavelength Selection for LUS Sources

Selection of optical wavelengths for LUS sources must maximize the amplitude of the converted acoustic wave at the specified acoustic frequency while maintaining eye and skin optical exposure levels for human subjects. For medical ultrasound imaging, typical acoustic frequencies ranging from 1-10 MHz are used, depending on the imaged tissue feature. As stated previously wavelength between 800-2000 nm satisfy the optical conditions to generate an LUS source in biological tissue. In this infrared (IR) spectral region, light induced thermal effects should be dominated by optical absorption of water in the tissue. The optical absorption of water between 800-2000 nm is shown in Figure 4-3a. The efficiency factor from Equation 4.6 is computed using the optical absorption of water between 800-2000 nm and the acoustic frequency of the LUS source up to 5 MHz. The normalized efficiency factor is shown in Figure 4-3b.

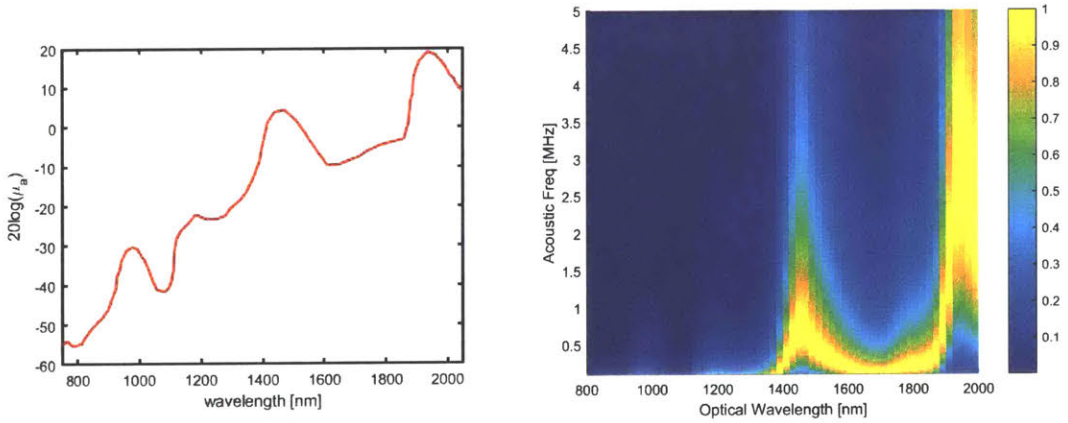

(a) Optical absorption of water

(b) LUS efficiency factor

Figure 4-3: Water optical absorption and LUS efficiency factor

Based on Figure 4-3b, optical wavelengths near 1500 nm efficiently generates an acoustic source centered at 1 MHz while optical wavelengths near 2000 nm efficiently generates an acoustic source centered at 3 MHz. Both generates sources should be relatively broadband before correction by the roughness and attenuation factors described previously. These predictions are based on the theoretical model for an Gaussian optical source on a water half-plane [70], to validate performance

in real biological tissue, LUS sources generated by a tunable multi-wavelength laser were measured on various *ex-vivo* animal tissues (bovine, porcine, and chicken).

4.4.1 Optical Absorption in Biological Tissue

A schematic of the measuring setup is shown in Figure 4-4. A Continuum 9030 Panther (30 *Hz*, 9 *ns* pulse length) tunable optical parametric oscillator (OPO) laser operating at discrete optical wavelengths from 800-2000 *nm* was the generation laser for evaluating LUS sources on biological tissue. Optical beam from the OPO was directed through an 3 *mm* diameter iris to maintain consistent spot size between all wavelength measurements. For each optical wavelength, an optical power meter measured the total irradiating power hitting the tissue sample after passing through the iris. A contact piezoelectric transducer was placed under the tissue sample to measure the generated LUS source. The measuring transducer had a 5 *MHz* center frequency and usable bandwidth between 0.5 and 8 *MHz*; the diameter was 3 *mm*, corresponding to a far field distance of 3 *cm*. All tissue samples were thicker than 3.5 *cm* to avoid near field effects. The transducer and sample were placed on a x-y translation stage to center the transducer in the irradiating optical beam. An Olympus 5077 PR pulser-receiver with 50 *dB* gain and 10 *MHz* low-pass filter amplified the measured signal from the transducer. Waveforms were digitized and recorded on a Tekronix TDS 2024B oscilloscope with 200 *MHz* bandwidth.

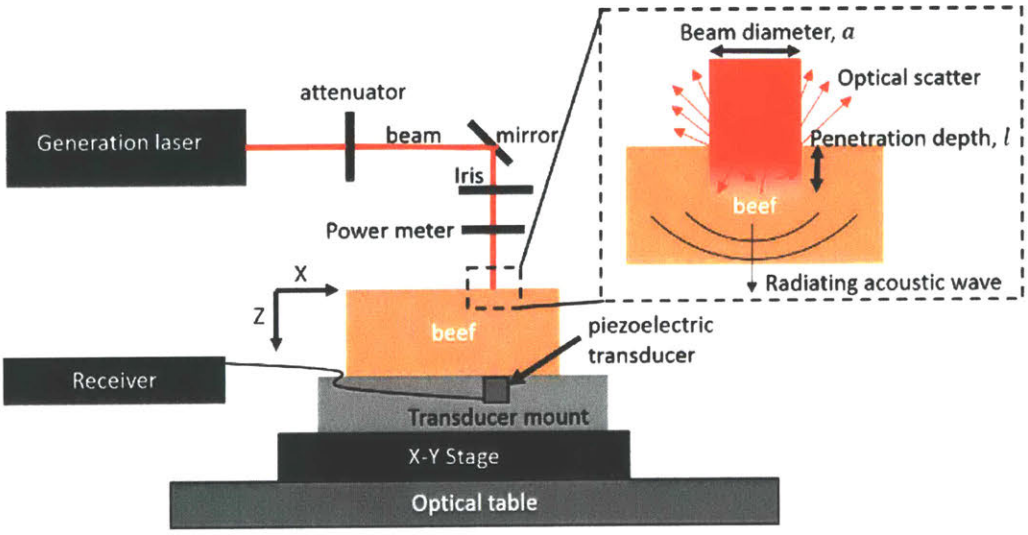

Figure 4-4: Experimental schematic for measuring LUS source amplitude for various optical wavelengths in excised animal tissue

Bovine, porcine, and chicken tissue were measured using the setup in Figure 4-4.

Tissue were obtained from the local grocery store and tissue use was approved by the MIT Committee on Animal Care in protocol number E17-09-0320. Bovine tissue only contain muscle and fat while porcine and chicken tissue included the skin layer. The source OPO laser was swept wavelengths between 800-2000 nm at 50 nm increments. The optical power at the tissue surface was kept at 7.5 mW (verified by the power meter) with the 3 mm diameter spot size through the iris, maintaining a fluence of of 3.54 mJ/cm^2. 25 waveforms were recorded at each wavelength, tests with insufficient signal to noise ratio were omitted from the data set. Energy for the generated LUS source were computed by integrating the measured waveforms with compensation by the conversion efficiency term discussed in Equation 4.5. The energy spectrum with and without compensation are presented in Figure 4-5, plotted against the optical absorption of water.

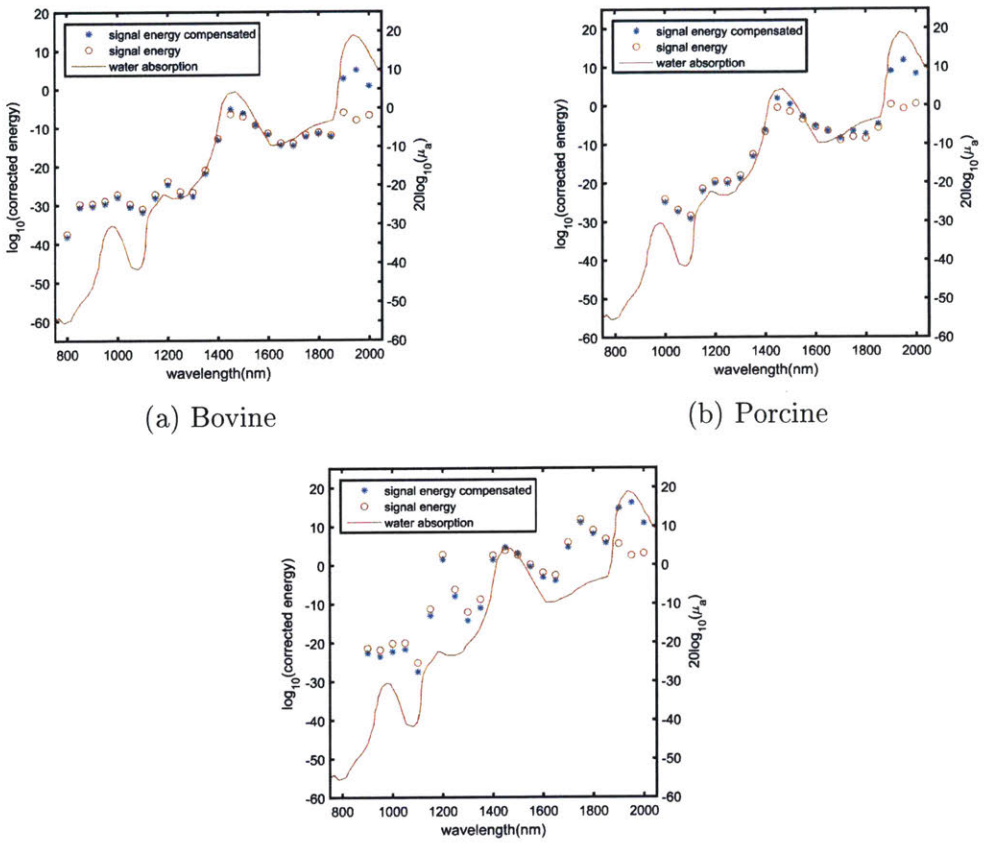

(a) Bovine

(b) Porcine

(c) Chicken

Figure 4-5: LUS signal energy as a function of optical wavelength in various excised animal tissue

As predicted, the LUS signal energy closely follows the absorption spectrum of water in the IR region. The bovine and porcine samples more closely follow the water absorption spectrum compared to the chicken sample and may be attributed to differences in mammalian versus avian tissue. All samples closely follow the high absorption peak of water near 1550 *nm* and is a promising candidate for LUS imaging. The absorption peak at 2000 *nm* is also a likely candidate with comparable LUS signal energy. However, optical safety limits must be considered for LUS imaging in human subjects. The allowable maximum permissible exposure (MPE) for eye and skin safety for optical wavelengths between 800-2000 *nm* and a 9 *ns* time scale pulse is plotted in Figure 4-6a [118]. The efficiency factor from Equation 4.6 scaled by the MPE is shown in Figure 4-6b.

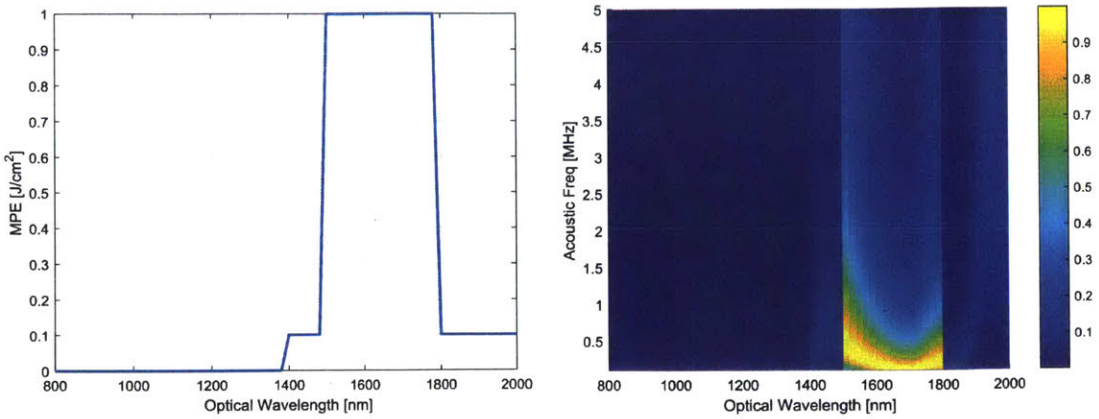

(a) MPE limits for human safety (b) Scaled LUS efficiency factor

Figure 4-6: Human safety limits and scaled conversion efficiency

The MPE as dictated by the ANSI Z136.1 standard is an order of magnitude lower for 2000 *nm* than 1550 *nm*. Despite comparable waveforms, 1550 *nm* is the better candidate for applying LUS imaging for humans subjects.

For 1550 *nm*, the theoretical versus measured LUS waveform and spectrum are presented in Figure 4-7 for bovine tissue. The theoretical model predicts a wide bandwidth LUS sources but the surface roughness factor and frequency dependent acoustic attenuation must be considered. With roughness and attenuation corrections, the expected bandwidth drops significantly. For validation, the bandwidth corrected theoretical model matches the measured LUS waveform at 1550 *nm*.

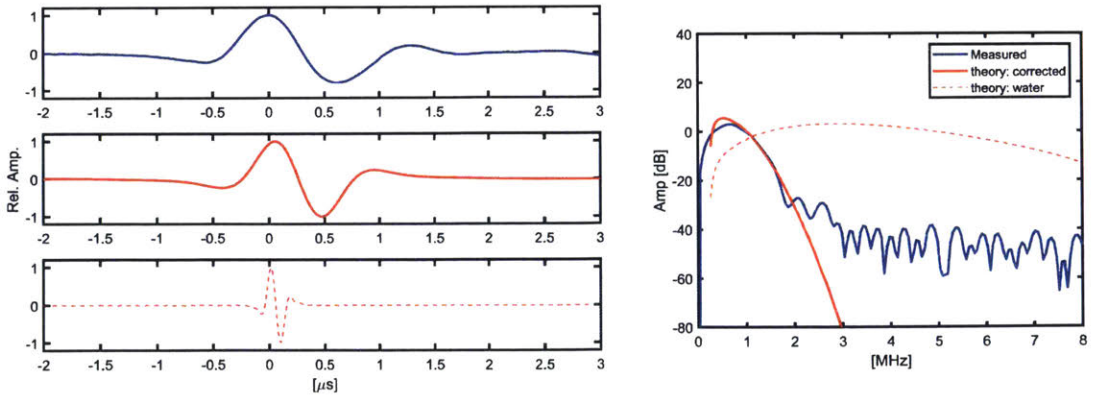

Figure 4-7: Measured LUS waveform on bovine tissue using a 1550 *nm* optical source with comparison to theoretical models with and without roughness and attenuation corrections.

For completeness, LUS waveforms at each optical absorption peak (950, 1550, and 2000 nm) along with the respective energy spectrums for each tissue type are shown in Figure 4-8.

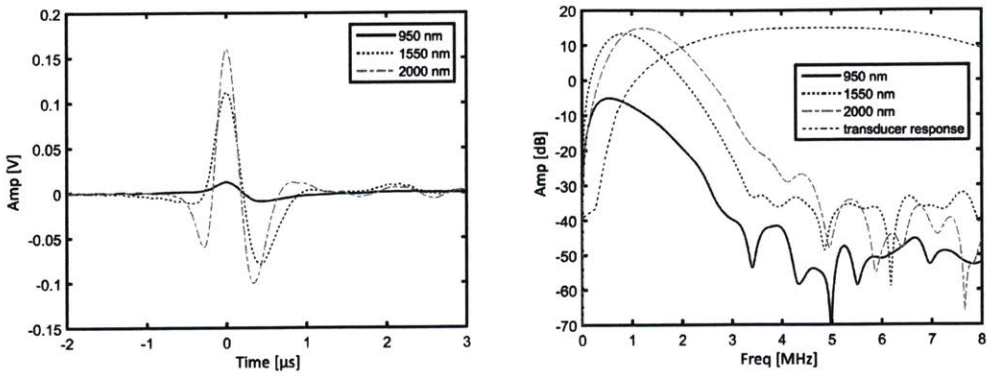

(a) LUS waveforms and spectrum on bovine tissue

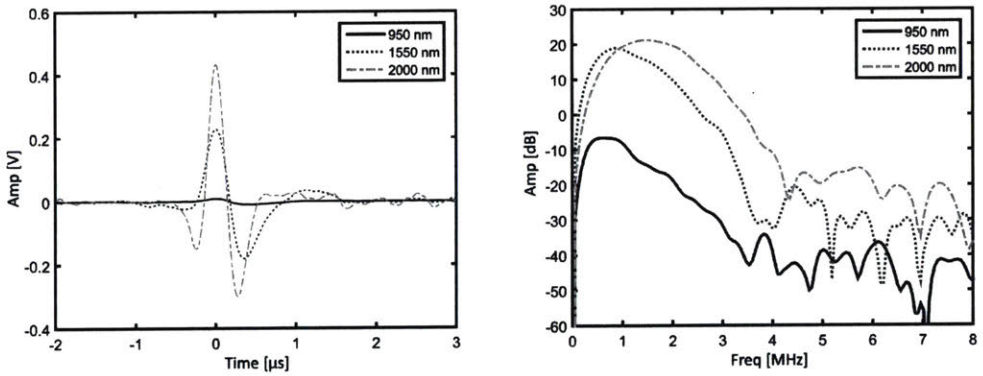

(b) LUS waveforms and spectrum on porcine tissue

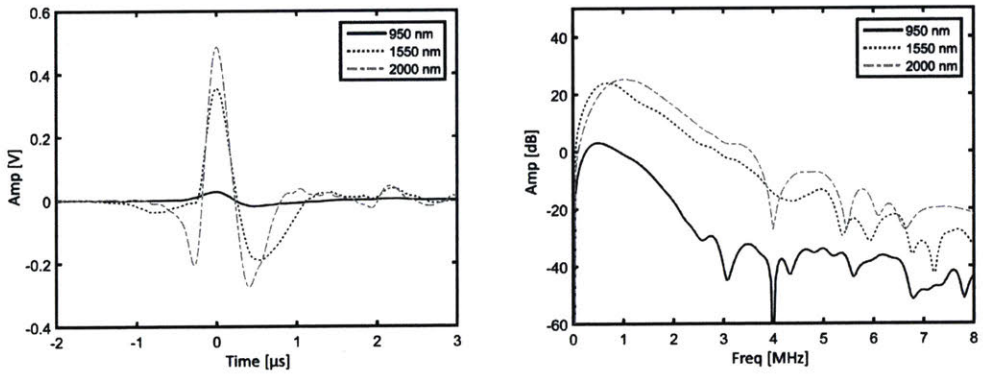

(c) LUS waveforms and spectrum on chicken tissue

Figure 4-8: Measured LUS waveforms and spectrums on bovine, porcine, and chicken tissues at 950, 1550, 2000 nm optical wavelengths

4.5 Optical Detection of Ultrasound

In contrast, optical detection of acoustic waves using interferometry is dictated by the amount of returning light from the tissue surface rather than the amount of light absorbed in the tissue. Quantity of returning light is dictated by the tissue reflectance characteristics and the irradiance of the interferometric light source. As exemplified in Figure 4-9, the returning light from a surface can be specular, diffuse, or a combination.

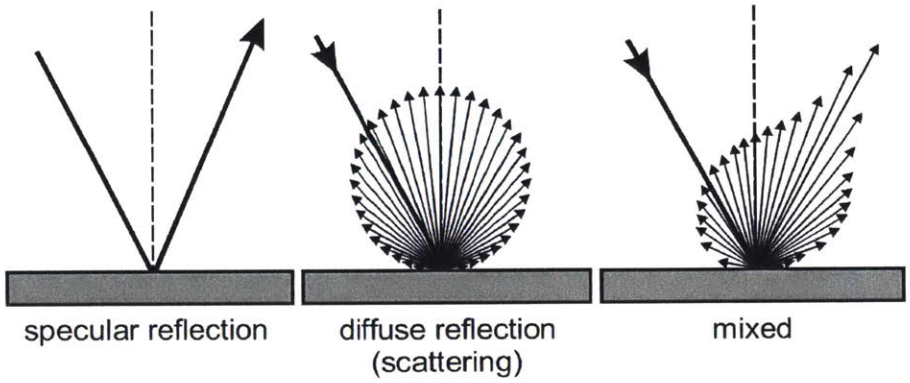

Figure 4-9: Optical reflections from a surface.

Retroreflective materials can be used to boost optical reflectance of the target surface and increase detection sensitivity; but should be avoided for LUS since currently available retroreflectors would impede the LUS optical source. For biological tissue, reflectance is wavelength dependent and the permissible irradiance is subject to ANSI MPE limits for human subjects. Assuming similar photodetector responsivity across the spectrum, wavelength selection should maximize reflected light while remaining under the MPE limits. Tissue reflectance is approximately the inverse of the tissue absorbance [121,122]. Measured optical reflectance values on humans for wavelengths 400-2000 nm reported from literature are shown in Figure 4-10a along with the ANSI MPE limits.

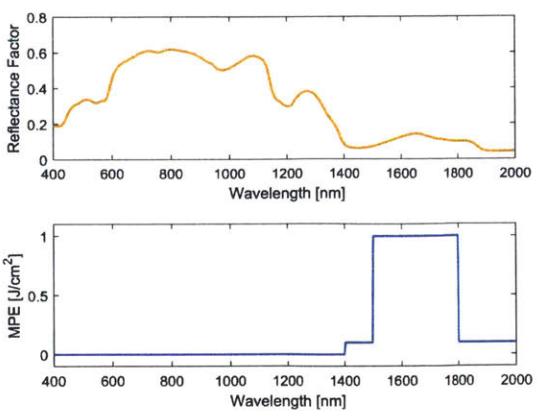

(a) Optical reflectance factor on human skin (top) and MPE limits (bottom).

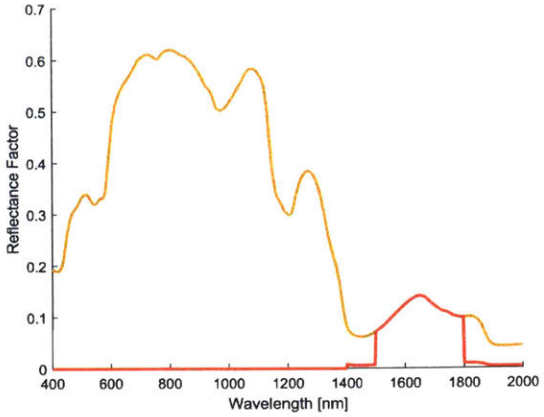

(b) Optical reflectance scaled by MPE limits (red)

Figure 4-10: Skin reflectance compared to MPE limits on skin

While wavelengths between 500 nm to 1200 nm offer the highest optical reflection factor, the ocular MPE for the region is three orders of magnitude lower than that of the far-infrared [118,121,122]. Combining MPE limitations and optical reflectance factors, shown in Figure 4-10b. If a skin surface is irradiated at the maximum MPE limits for every spectral region, the maximum quantity of returning light to a detector is still in the far-infrared. For anatomical ultrasound imaging, acoustic time signals are hundreds of microseconds. At this time scale, the highest MPE is 1 J/cm^2 for wavelengths between 1500 nm to 1800 nm where ocular and skin MPE limits are identical. Although LUS imaging only targets the skin, ocular MPE was considered for patient safety and minimizing the need for additional safety features in the clinical setting. Disregarding eye safety would mandate eye protection, complete enclosure, or specialized clinical facilities solely for LUS imaging. Despite the high optical absorption, the spectral region between 1500-1800 nm is still the ideal spectral region which maximizes reflected light from the tissue while balancing system complexity and patient safety.

4.6 Summary

In summary, the photoacoustic (PA) phenomenon is due to the conversion of optical to acoustic energy within the irradiated subject due to the optical absorption. By tuning the optical wavelength, PA sources can be generated at various depths within the subject depending on which region of the subject is absorptive to the irradiating light. Differentiating LUS from conventional PA in medical imaging, LUS specifically limits optical to acoustic conversion to the tissue surface whereas PA penetrates into the tissue to image other photo-absorptive targets such as blood vessels. PA is limited in imaging depth due to high optical attenuation in biological tissue. In comparison, acoustic attenuation in tissue is two orders of magnitude lower than the optical attenuation. By restricting the source to the tissue surface, LUS solely relies on acoustic propagation within the tissue, allowing deeper imaging depths than typical PA.

Efficient conversion of optical to acoustic energy in biological tissue is dominated by the irradiating optical wavelength. Selection of the proper wavelength for imaging is critical for both the optical LUS source and detector. Optical wavelength between 800-2000 nm satisfy conditions to generate an LUS source in biological tissue. Within these wavelengths, optical absorption should be predominately due to the absorption characteristics of water. Selection for peaks in the water optical absorption spectrum should yield the highest efficiency LUS source in biological tissue. Experimental LUS waveforms on bovine, porcine, and chicken confirm agreement between theoretical and measured LUS sources. Of the measured wavelengths, 1550 nm is the ideal candidate for LUS imaging for the high amplitude converted LUS source as well as having the highest allowable optical exposure limits dictated by ANSI. For detection, $\sim$1500 nm is also the ideal wavelength due to the high allowable optical exposure limits, despite having lower reflectance values than other spectral regions. Balancing safety and performance, wavelengths near 1500 nm are ideal for both LUS source generation as well as detection. Fortunately, 1550 nm is a prevalent wavelength used in the telecommunication industry, enabling rapid LUS development using commercially

available components.

Chapter 5

LUS - System Design and Imaging

Following identification of ~1500 *nm* as the ideal wavelength for LUS, optical components were selected and evaluated on tissue mimicking phantoms, *ex-vivo* animal tissue, and human volunteers. A imaging setup using linear translation stages and steering mirrors was built to facilitate scanning of the optical source and detector for 2D or 3D imaging. Approval was obtained from the MIT Committee on the Use of Humans as Experimental Subjects (COUHES) and all optical outputs were independently verified to be eye and skin safe prior to human imaging. Reconstructed LUS images were verified by a conventional clinical ultrasound imager (GE Logiq E9) to validate features detected in the LUS image. LUS imaging results validate the feasibility of LUS to detect similar tissue features visible in conventional ultrasound systems. Demonstrated LUS capabilities are promising and motivate future LUS development toward clinical implementation.

5.1 Optical Source and Detector

With the commercial availability of ~1550 *nm* optical components and systems, evaluation of the proposed LUS design could be completed using presently available technology. A 1540 *nm* passively Q-switched pulsed laser (Optitask OT-37) with 10 *Hz* repetition rate and measured 2.3 *mJ* pulse energy was selected for LUS source generation. A commercially available class-2 laser Doppler Vibrometer (Polytec RSV-150)

with measured continuous wave power of 9.8 mW at 1550 nm and a green tracking laser ($<1mW$) was selected for optical detection of ultrasonic signals. Bandwidth of the LDV is 2.5 MHz with 49 $mm/s/V$ sensitivity. The corresponding optical source irradiance is 0.024 J/cm^2 and the optical receiver irradiance is 0.1 W/cm^2. Both lasers are within the respective pulsed and continuous MPE limits at the IR spectrum for eye and skin safety. Significant margin of safety is available to engineer custom LUS solutions with higher power and faster repetition rate but is out of the scope of the human LUS feasibility study presented here. The selected optical source and detector are shown in Figure 5-1.

(a) OT-37 LUS source

(b) RSV-150 LUS Detector

Figure 5-1: Optical source and detector selected for LUS imaging

5.2 LUS Scans

For each slice or volumetric image, the optical source and detection points were collocated and sequentially scanned on the sample surface linearly or rastered, respectively. Optical steering and collocation were completed using either fast steering mirrors (Optics in Motion LLC, OIM102.3) or linear stages (Sigma Koki Co, SGSP26-200 stage, SHOT-702 motion controller). Spatial sampling frequency in each instance satisfies the Nyquist limits for the expected 1.5 MHz maximum acoustic frequency to prevent grating lobe interference. A scan length of 5 cm at 0.5 mm pitch was completed for each linear imaging instance. Aperture length for LUS was the same

as the conventional ultrasound probe used for verification. For volumetric LUS imaging, a phantom was scanned with a 4 cm by 8 cm mesh grid with 0.5 mm pitch. At each sampling point, 40 time traces were taken for post-processing and image reconstruction. Data acquisition from the LDV was recorded on a digital oscilloscope (National Instruments, NI PXIe-5170R, 14-bits, 250 MHz max bandwidth) nested in a NI PXIe-1073 chassis. Schematic of the LUS imaging system is shown in Figure 5-2a and photograph of the experimental setup is shown in Figure 5-2b.

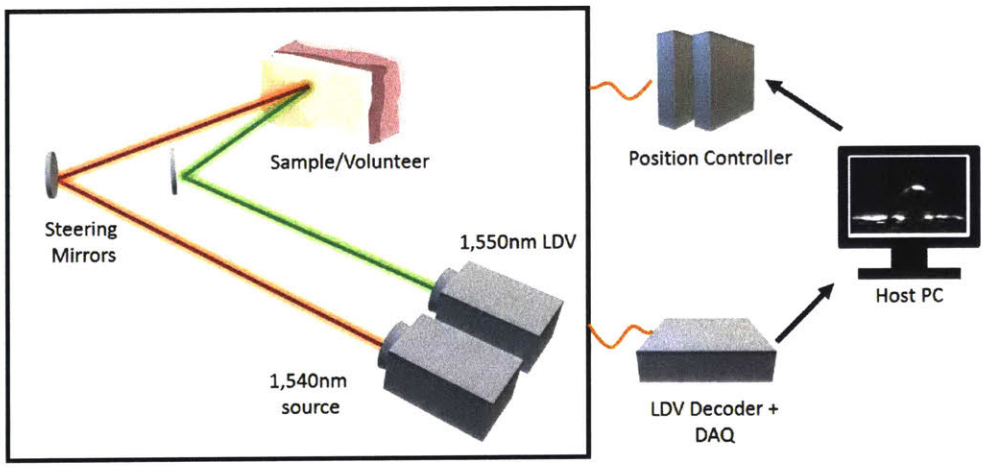

(a) Schematic of the LUS System

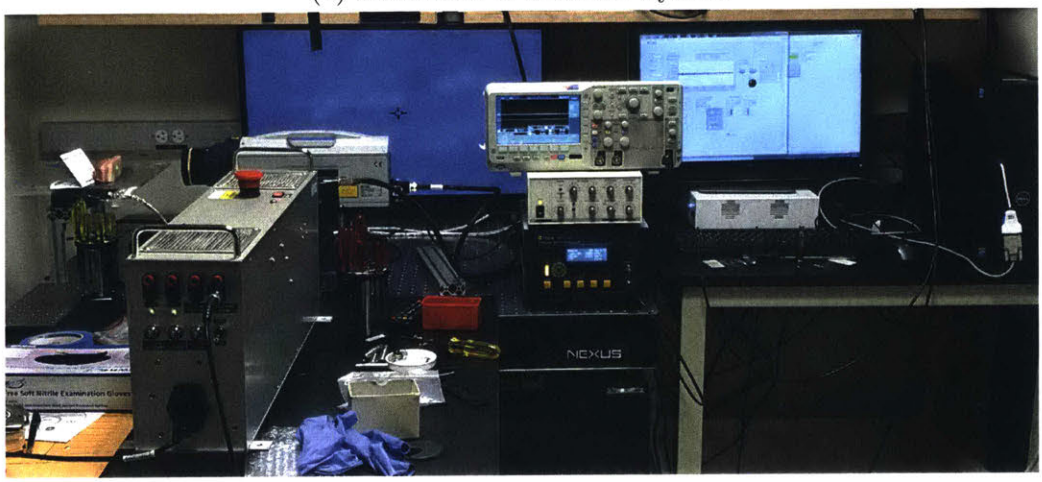

(b) Experimental LUS System

Figure 5-2: LUS system schematic and experimental setup. The optical source and detectors are on the left. The control and data acquisitions systems are shown in the center and right side. Displays show current view of the LDV on the left and collected waveforms on the right.

5.2.1 Conventional Ultrasound Validation

A standard clinical system, GE Logiq E9, with a 9 *MHz* linear probe provided verification of the LUS images using conventional ultrasound methods. The acquisition process with the conventional system consisted of applying ultrasound gel (Aquasonics 100) to the probe and acquiring B-mode ultrasound images at the same location as the LUS scan. Though the conventional ultrasound system operates at significantly higher frequency and leverages beamforming, gross comparisons of large soft/hard tissue features such as fascia, arteries, muscles, tendons, and bones are still possible between LUS and conventional ultrasound. The B-mode ultrasound serves as a clinical standard to verify the tissue features detected using LUS.

5.3 Image Reconstruction

Post data acquisition, the raw traces are post-processed using averaging with a trace coherence factor in Equation 5.1. A Synthetic Aperture Focusing Technique (SAFT) algorithm (Equation 5.2 - 5.4) with a spatial coherence factor - to minimize side-lobe artifacts - reconstructed images for each LUS dataset [123–128].

For each pair of transmit and receive position n, the 50 data traces (A-lines) are collected and compiled into to a single trace using the trace coherence factor Equation 5.1.

$$\hat{t}_n = \bar{T}_n \frac{\left(\sum_{q=1}^{Q} t_q\right)^2}{Q \sum_{q=1}^{Q} t_q^2} \tag{5.1}$$

where $\hat{t}_n$ is the processed trace, $\bar{T}_n$ is the mean of all A-lines at position n, q is the index of an A-line, Q is the total number of A-lines, and t_q is the A-line with index q. $\hat{T}$ data matrix is then formed from compiling all traces from $n = 1$ to $n = N$.

Image formation using SAFT is described by Equation 5.2

$$I_{i,j} = (CF_{i,j}) \sum_{n=1}^{N} \hat{T} \ (dv_{n,i,j}, n) \tag{5.2}$$

where $CF_{i,j}$ is the spatial coherence factor given in Equation 5.4, $I_{i,j}$ is the image

pixel value at row and column index $(i,\ j)$, $dv_{n,i,j}$ is the imaging delay given in Equation 5.3, N is the total number of traces transmit receive pairs.

Imaging delay is given by

$$dv_{n,i,j} = \left[\frac{f_s}{c} \left(\sqrt{(x_{i,j} - xs_n)^2 + (y_{i,j} - ys_n)^2} + \sqrt{(x_{i,j} - xr_n)^2 + (y_{i,j} - yr_n)^2} \right) \right] \tag{5.3}$$

where f_s (Hz) is the sampling frequency. c (m/s) is the speed of sound, xs_n and xr_n are x-position of the transmitter and receiver respectively, ys_n and yr_n are y-position of the transmitter and receiver respectively, and $x_{i,j}$ and $y_{i,j}$ are x and y-positions of the image pixel.

The spatial coherence factor $CF_{i,j}$ is similar to the trace coherence factor in formulation but is computing the coherency between overlapping signals at each image pixel location $I_{i,j}$ rather than at each time instance in trace t_n. $CF_{i,j}$ is given by

$$CF_{i,j} = \frac{\left(\sum_{n=1}^{N} \hat{T}\ (dv_{n,i,j}, n) \right)^2}{N \sum_{n=1}^{N} \hat{T}^{\ 2} (dv_{n,i,j}, n)} \tag{5.4}$$

5.4 Phantom Imaging

The LUS system was initially evaluated on tissue mimicking phantoms and *ex-vivo* porcine tissue prior to experimentation on human volunteers. Tissue mimicking gelatin-water phantoms with various inclusions were constructed. The high water content of gelatin phantoms replicates the optical absorption characteristics of biological tissue in the infrared (IR) spectrum. Metallic spheres, rods, disks, and square shaped inclusions are embedded in the phantoms to evaluate the LUS system imaging capabilities. The optical source and detection point positions are mechanically calibrated, controlled, and collocated using steering mirrors or linear-stages. Free-space control of the source and detection positions enables both 2D and 3D imaging of any arbitrary surface. Time-series output of the LDV is recorded through a digital oscilloscope connected to the host computer.

5.4.1 Phantom Composition

LUS phantoms consist of porcine gelatin (6% by weight, Sigma-Aldrich, gel strength 300, Type A) dissolved into deionized water at 85 °C. To match typical tissue sound speeds, 1-propanol (2% by weight, Alfa Aesar, A19902) was dissolved into the gelatin mixture. The solution was cooled to 45 °C prior to pouring into molds with the desired inclusions. The solution was degassed in the molds and left to solidify at room temperature. All phantoms were sealed and stored at 4 °C and used in experiments within one week of construction to avoid sound speed changes due to water loss over time. Photograph of the phantom used for 2D and 3D imaging is shown in Figure 5-3b.

5.4.2 LUS Phantom Images

As shown in Figure 5-3, image reconstruction of LUS line scans and raster scans using SAFT in conjunction with a coherence factor reconstructed both 2D and 3D images of the gelatin phantoms. By inspection, LUS image features are identical to those shown in the photograph (Figure 5-3b/5-3d). The LUS system was also able to

generate 3D volumetric images by raster scanning the LUS source and detector on the on the phantom surface (Figure 5-3c). Prior LUS research has imaged phantoms with embedded objects/tissue but relied on added retroreflective material on the phantom surface to enhance optical reflectivity for the optical detector [103,129]. By specifically selecting wavelengths near 1500 nm, various targets could be imaged without any surface treatment while maintaining eye and skin safety for human imaging.

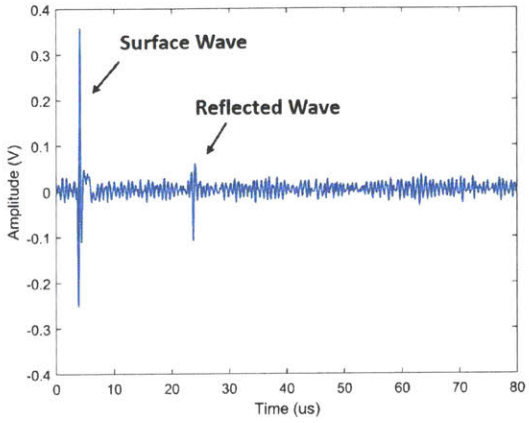

(a) Single LUS waveform

(b) LUS phantom

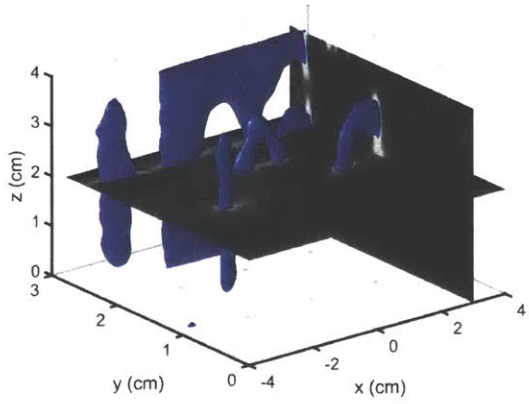

(c) 3D LUS volume with segmented reflection surfaces

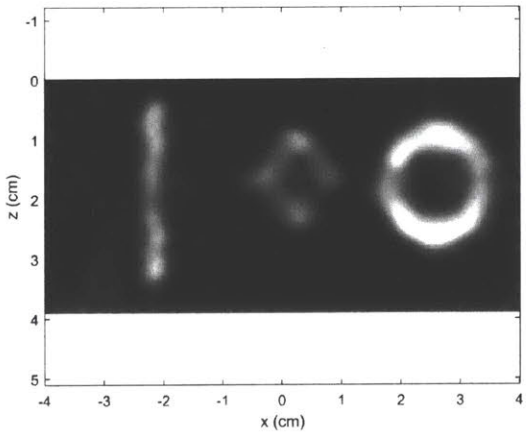

(d) Frontal projection of the 3D LUS volume

Figure 5-3: LUS image results demonstrating 3D imaging capabilities of LUS over a 2D surface scan on a gelatin phantom with multiple inclusions.

From prior literature, a LUS source in water should be broadband and the spatial beam pattern should be similar to that of a point or disk source, depending on the size of the impinging laser spot [70, 98]. However, biological tissue char-

acteristics such as optical/acoustic attenuation, surface roughness, and absorbance restrict the detectable LUS source bandwidth to be 1.5 MHz or below [70, 129, 130]. While gelatin-based PA phantoms can mimic the bulk characteristics of LUS sources in water, phantoms replicating exact optical characteristics of skin in conjunction with surface optical characteristics are still unavailable. While phantom LUS imaging demonstrates the volumetric and the non-contact features of LUS, direct LUS imaging of analogous animal tissue or humans provides a more representative and encompassing evaluation of LUS system capabilities.

5.5 *Ex-Vivo* Tissue Imaging

Excised porcine abdominal tissue was imaged in the LUS system. Using porcine tissue as a human analogue in biomedical research is well established, including for use in toxicology, immunology, wound healing, and radiation [131,132]. Porcine skin is similar to human skin in both anatomical structure and optical composition [133]. Porcine abdominal tissue was obtained from the local market without specialized preparations to include natural skin variations. For each sample, the epidermis, dermis, subcutaneous fat, and muscle layers are clearly visible. The strips were approximately 5 *cm* thick and cut to 25 *cm* lengths prior to LUS imaging. Use of animal tissue was approved by the MIT Committee on Animal Care protocol number E17-09-0320. Similar to phantom imaging, LUS line scans were completed on each sample. Reconstructed LUS images with verification from conventional ultrasound are shown in Figure 5-4c and Figure 5-4d, respectively. No damage or marking was visible on any tissue surfaces post LUS experiments.

Reconstructed LUS image confirms that LUS is sensitive to soft-tissue features at eye and skin safe optical exposure levels. In the LUS image (Figure 5-4c), highly reflective air-tissue interfaces are visible at 4.5 *cm*, while weakly reflective soft-tissue boundaries such as skin-fat and fat-muscle interfaces are also present. The subcutaneous fat layer and multiple muscle-fat boundaries are clearly present in the LUS image. Conventional ultrasound imaging (Figure 5-4d) and visual inspection (Figure 5-4b) verified all boundaries and features detected in the LUS images. Dominant soft-tissue boundaries are present in both LUS and conventional ultrasound images at 1 *cm*, 2 *cm*, and 3.5 *cm*. In particular, the contour of the first reflecting muscle-fat layer at 1 *cm* matches in both the LUS and conventional image. Deeper layers in the LUS images show an increase in artifacts around the boundaries and is likely due to the lack of elevation focusing for LUS imaging; whereas, the conventional ultrasound probe is focused in plane to minimize out of plane reflections. More acoustic speckle is present within the top 2 *cm* of tissue in the conventional ultrasound image but is absent in the LUS image, likely due to the lower LUS imaging frequency, bandwidth,

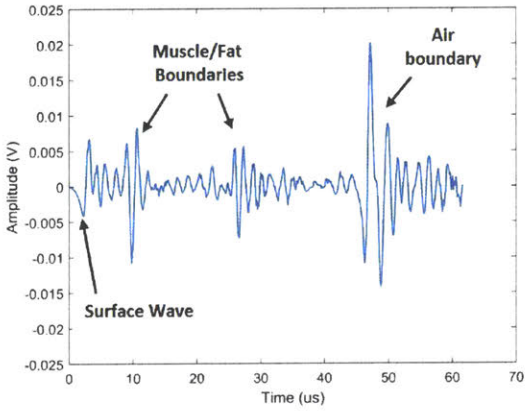

(a) Single LUS waveform

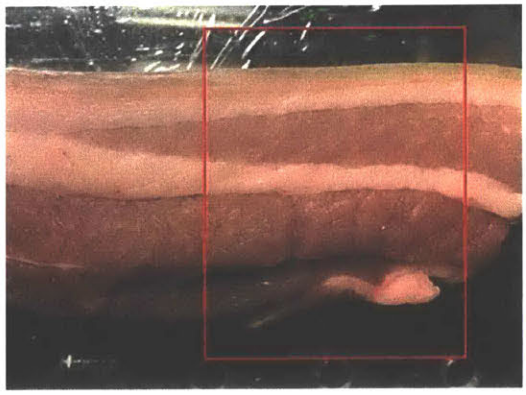

(b) Porcine Tissue

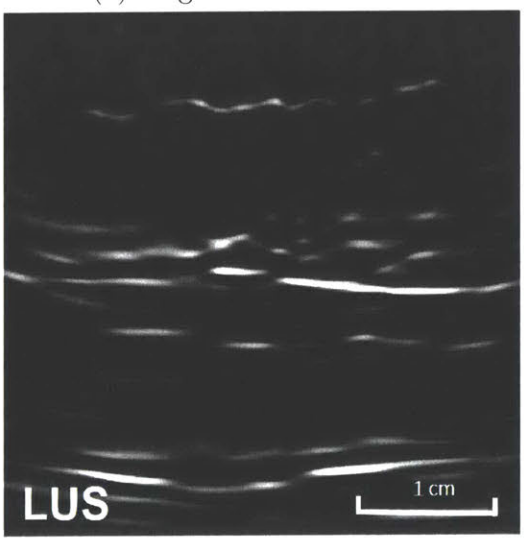

(c) LUS Image

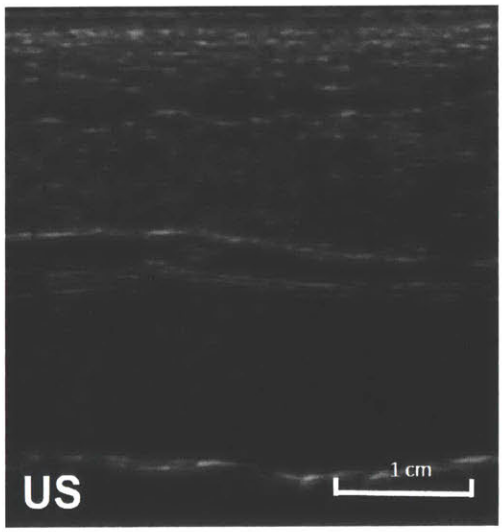

(d) Conventional US Image

Figure 5-4: LUS image slice on porcine tissue to evaluate LUS performance on more optically representative tissue against conventional ultrasound imaging.

and lateral resolution. At this point, an exact comparison of conventional ultrasound to LUS images is not possible due to differences in acoustic beamforming, number of transducer elements, and acoustic source characteristics; however, we can conclude that non-contact LUS imaging of biological tissue has adequate sensitivity for soft-tissue anatomical imaging and is feasible within a patient safe optical exposure regime.

5.6 Human LUS Imaging

All human LUS experiments were completed with approval from MIT Committee on the Use of Humans as Experimental Subjects (Protocol # 1702850719R001). As an extra precaution, all laser component optical outputs were measured using an optical power meter (Ophir Nova II). All personal identifiers were removed from the LUS and conventional US data to preserve volunteer anonymity. Each imaging instance covered a $\sim$5 cm line across a volunteer's forearm with conventional ultrasound imaging completed at the same location immediately following LUS imaging. The forearm was selected for ease of accessibility by the LUS system and significant collections of soft and hard tissue features.

Four volunteers' forearms were imaged using the LUS system. Both source and detection lasers optical outputs are manufacturer rated eye and skin safe but were independently verified. Laser safety glasses were still available if requested by any volunteer. The pulsed laser source and CW detector were verified to be 2.3 mJ per pulse at 10 Hz and 9.8 mW, respectively. Calculated following the ANSI standard, the corresponding source and detector irradiances are 0.024 J/cm^2 and 0.1 W/cm^2, both within eye and skin MPE limits. Consent from each volunteer was obtained prior to LUS and conventional ultrasound imaging. Similar to previous experiments, conventional ultrasound imaging using the GE Logiq E9 system followed each LUS imaging session for feature verification. LUS and conventional scans were completed on the inside and backside of volunteers' forearms. No volunteer reported any sensation, discomfort, or tissue change during or following any LUS imaging session. Imaging results are shown in Figure 5-5.

Within the reconstructed LUS image shown in Figure 5-5c, tissue features such as muscle fascia boundaries and the bone surface are clearly detected. In Figure 5-5c, the muscle fascia boundary is present from 0.5 cm to 1 cm, and the surface of the ulna from 2 cm to 2.5 cm. Similar to Figure 5-4c, deeper layers in the human LUS image presents with more artifacts around the boundaries due to the lack of elevation (in-plane) focusing commonly implemented in conventional ultrasound probes.

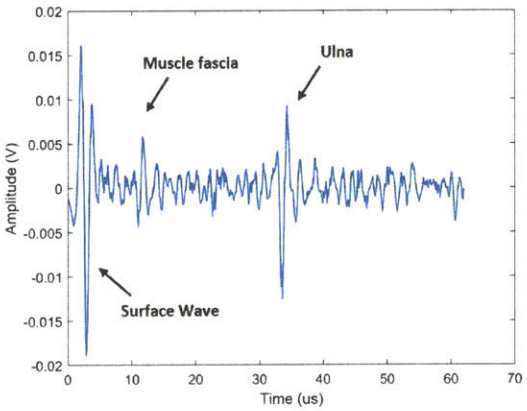

(a) Single LUS waveform

(b) Subject Forearm

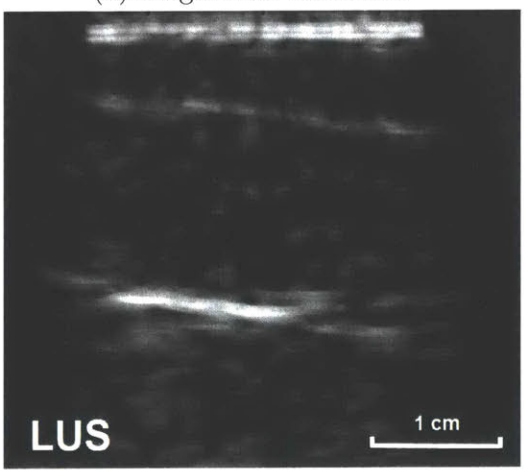

(c) LUS Image

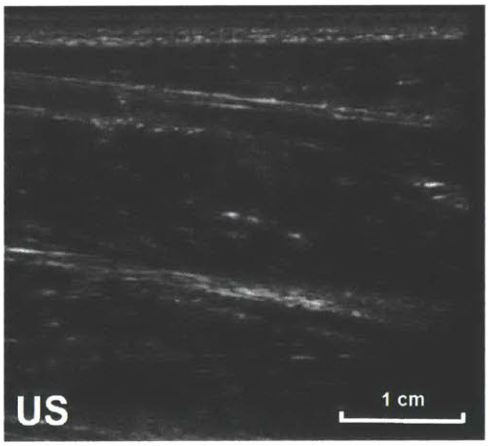

(d) Conventional US Image

Figure 5-5: LUS images demonstrating LUS capabilities for *in-vivo* human imaging at eye and skin safe optical exposure levels with comparison to conventional ultrasound

In contrast, the human LUS image (Figure 5-5c) has more artifacts than the porcine LUS image (Figure 5-4c) and is likely due to patient motion during imaging or optical reflection variations with on the skin surface. In the current LUS embodiment, LUS data acquisition speed is limited by the repetition rate and power of currently available optical sources and receivers. For a clinical implementation of LUS, higher repetition rate and multi-point optical sources and detectors will reduce LUS imaging time and minimize patient motion during imaging. From the current human LUS results, acoustic reflections from both soft-tissue and hard-tissue boundaries strongly suggest that a LUS source in combination with interferometric detection has sufficient sensitivity for *in-vivo* human soft and hard tissue imaging at safe optical exposure levels.

5.7 Summary

In comparison to PA systems, LUS imaging is more directly comparable to conventional ultrasound imaging. In PA, the acoustic source is below the skin surface. In LUS, the acoustic source is at the skin surface. Current PA systems are well suited for shallow absorptive features such as blood vessels. LUS minimizes optical attenuation in tissue - maximizing acoustic energy generation - and is able to image deeper anatomical features by solely relying on acoustic propagation within the tissue, analogous to conventional ultrasound. In conjunction with non-contact optical detection, conventional piezoelectric arrays can be eliminated. The LUS results on phantoms, animal tissue, and humans presented in this thesis demonstrate the capability of a non-contact fully optical LUS imaging system. First *in-vivo* human subject results using LUS is a significant step toward proving the clinical feasibility of LUS. Components of LUS technology have been explored in prior research but full demonstration of LUS on humans has not previously been presented. By careful analysis of the light and tissue interactions, this thesis demonstrates LUS capabilities for *in-vivo* human imaging at eye and skin safe levels, without using surface treatment to enhance optical detection sensitivity or the source characteristics.

The human LUS images (Figure 5-5c - 5-5d) illustrate the use of LUS for *in-vivo* anatomical imaging, verified by a conventional ultrasound imager. Direct image comparison of nascent LUS technology against well-established medical ultrasound is rather premature. Conventional ultrasound images presented here used a 9 *MHz* center frequency transducer with beamforming and is expectedly higher image quality and resolution than that of LUS images. Nevertheless, similar structures and dimensions are consistently observed in both methods and we can verify that LUS on humans is feasible and is sensitive to the same features present in conventional ultrasound. In addition, this thesis identifies the necessary design guidelines and enabling technologies to allow human operation at eye and skin safe levels. LUS images presented are comparable to ultrasound images at incipient stages of ultrasound imaging decades ago [4]. As discussed in the following chapter, recent technological advances in laser technology, silicon photonics, and hydrogels may greatly benefit further LUS development. While further work remains prior to commercialization and clinical use, the core enabling technologies of LUS are available and the presented LUS images should motivate future research and development. With these promising results, one can envision a fully optical, non-ionizing, and non-contact ultrasound system capable of repeatable and large volume imaging.

Chapter 6

LUS - Road Map for the Future

Qualitatively comparing LUS images to conventional ultrasound images, smaller sub-millimeter features seen in the conventional ultrasound image are lost in the LUS image due to limitations in LUS resolution. Currently, LUS lateral resolution is limited due to single-point optical measurements versus multi-point transmit and receive beamforming in the conventional clinical imager. The depth resolution is limited due to bandwidth limitations of LUS sources in biological tissue. Nevertheless, LUS images are comparable to images produced at the emergent stages of conventional medical ultrasound in the 1960's [4]. Similar to the evolution of conventional ultrasound, technological progress in related fields can and will improve LUS image quality over time. As discussed in this chapter, present LUS challenges can be mitigated by improvement of current of laser technology, minor treatment of the tissue surface, and implementation of chip-scale laser technology.

6.1 LUS Improvements using Current Technology

Adaptation of currently available technology specifically for LUS could improve LUS system capabilities. For example, use of an amplitude modulated source laser, 3D profiling/tracking of the surface geometry, and minor surface treatment of the tissue will enhance multiple facets of LUS.

Amplitude Modulated Lasers — A pulsed laser source interacting with water produces a broadband acoustic source but is bandwidth limited when used on biological tissue [70, 129]. However, specific acoustic frequency bands could be amplified by time modulating the optical source amplitude at the desired acoustic frequency [70]. Implementing a fast amplitude modulated optical source could improve LUS imaging depth, bandwidth, and resolution; in addition, conventional ultrasound techniques to amplify acoustic signal-to-noise ratio such as pulse compression, matched filtering, and source encoding can be leveraged.

Spot Tracking — For accurate image reconstruction of large volumes, 3D characterization of the tissue surface geometry could assist in localization of source positions. LUS optical transmit and detection occur at the tissue surface, spatial location of the source and receiver are both subject to variations in tissue surface geometry. For a sufficiently small imaging aperture on a region of the body with minimal curvature, as presented in Chapter 5, the surface geometry can be approximated as planar, but larger volume LUS imaging - where the tissue surface is noticeably curved - will require active spatial localization of the LUS source and detector position or prior characterization of the body surface geometry. With multi-point optical transmit and detection, characterization of surface geometry will be critical toward enabling acoustic beamforming in LUS. Adaptation of computer vision techniques such as 3D imaging and tracking technologies could make large volume LUS imaging feasible. Optical tracking of the source and detector is also required if patient motion is significant during data acquisition. With sufficiently fast data acquisition, LUS systems could behave like a body volume camera, capable of simultaneous 3D imaging of both the external and internal tissues.

Surface Treatment — As mentioned previously, LUS system performance is subject to the optical and acoustic properties of the tissue surface. Biological tissue characteristics directly dictate optical to acoustic conversion efficiency, source frequency, detection sensitivity, and MPE safety limits. The maximum allowable optical irradiance on a patient is bounded by the MPE limits; however, minor treatment of the tissue surface could bypass these limitations. Enhanced optical reflection is com-

monly achieved with retroreflective beads or tapes [103,129]. However, retroreflective tape or dust on the tissue surface can significantly alter or block the LUS source and may be hazardous for human use due to possible respiratory irritation. Gel or gel pads embedded with optical reflectors could be used to enhance optical detection without interference to the optical source; bulk water content of the gel preserves the LUS source characteristics in the IR spectrum while embedded reflectors enhance the optical return and detection sensitivity. Gel or gel pads routinely used for ultrasound imaging can be augmented for LUS imaging. A thin layer on the skin could enhance the optical performance while protecting the skin surface from higher power IR laser irradiance. The surface treatment layer could expand the LUS source bandwidth, improve optical detection sensitivity with higher surface reflectance, and permit higher optical exposure limits. However, irradiance exceeding eye and skin MPE limits on the treatment surface layer will require additional safety measures such as laser enclosures or mandatory eye protection, depending on the tissue region of interest. In comparison, radio frequency (RF) coils and contrast agents are commonly used for MRI and CT, respectively; use of a minor surface treatment layer could greatly improve LUS image quality without adding significant system complications. Flexible hydrogels could also be easily augmented for LUS; the bulk water content of hydrogels mixed with retro-reflective particles could amplify both LUS source and detector behavior [134].

6.2 Future Enabling LUS Technologies

Validation of LUS sensitivity to soft-tissue features using a single optical source and detector point is a significant demonstration of clinical viability. Both LUS and PA are limited by currently available laser technology [91, 92, 95, 105, 135, 136]. Future development of LUS should focus on parallelizing optical sources and receivers to implement transmit and receive beamforming techniques that enable conventional ultrasound imaging. Since spatial locations of LUS sources can be known *a priori*, unlike penetrating PA sources, transmit beamforming can only be implemented in LUS.

Multi-channel optical sources and detectors for LUS imaging will dramatically improve both LUS image quality and acquisition speed. Development of high-repetition and high-energy lasers will improve signal-to-noise ratio and reduce data acquisition time. The silicon photonics industry, fueled by the sensors required for autonomous car operations, has developed chip-scale, solid-state, steerable laser technology applicable for both PA and LUS imaging [137–142]. Since the ideal operating range for LUS is near $\sim$1500 nm; recent communication and silicon photonics innovations may directly impact LUS system development.

6.3 Outlook of LUS

Based on the encouraging results, LUS inspires confidence for further research and development. Human LUS images verify the feasibility of the LUS technique for *in-vivo* anatomical imaging without compromising patient safety. LUS is sensitive to both hard and soft anatomical features similar to conventional ultrasound but is fully non-contact. Real-time remote sensing of biological tissue would find broadly applicability in non-intrusive patient monitoring, contact sensitive imaging (elastography, musculoskeletal disease tracking), and intraoperative applications. Current embodiments of LUS for research are generally single point transmission and detection due to high cost and complexity. Clinical iterations of LUS will require multi-point optical transmission and detection to amplify acoustic source amplitudes and reduce data acquisition time. Analogous challenges existed in the nascent stages of conventional ultrasound imaging. Scaling from mechanically scanned single element systems to highly parallelized real-time clinical imagers took decades of research and development. A similar pathway is likely for LUS - parallelization of single- to multi-point laser technology. Initial human results are encouraging; rapid advances in related industrial sectors will establish the necessary technologies to enable clinical implementation of LUS.

6.4 Timeline of US Development vs. LUS

In retrospect, the development of medical ultrasound is remarkably similar to current development of optical ultrasound. A timeline of medical ultrasound development alongside optical ultrasound development is shown in Table 6.1.

Imaging using acoustic propagation was first proposed in 1700s by Robert Hooke but was not applicable as a imaging method until the discovery of piezo-electricity. Similarly, the photoacoustic effect was reported in 1880 by Alexander Graham Bell but was not applicable until the advent of high power laser sources [88]. In the nascent stages of medical ultrasound in 1950's, single piezoelectric transducers were mechanically scanned to capture sub skin surface tissue features. Commercial imaging using ultrasound arrays did not appear until 1980s, following the rapid development of transistor technology and accurate manufacturing of piezoelectric arrays [4]. Piezoelectric arrays revolutionized ultrasound imaging by enabling multi-element transmit and receive beamforming. Computational advances in video processing, digital memory, and amplifier technology following exponential growth of integrated circuitry, produced real-time 3D ultrasound imagery in the 2000's. A similar path is likely ahead for LUS. Interestingly, both conventional medical ultrasound and photoacoustics were initially used for fault detection in non-destructive testing prior to development for human imaging [4]. As mentioned in the previous section, parallelization, miniaturization, and cost reduction of lasers will be the enabling technology to advance LUS toward clinical implementation. As of now, LUS is a mechanically scanned single point transmit and receive system comparable to early stage ultrasound systems. Demonstration of LUS on human subjects presented in this thesis is the first critical step in establishing LUS as a feasible imaging technique for future development.

Year	Conventional Ultrasound	Optical Ultrasound	Year
1700	Robert Hooke proposes using sound for diagnostics in the body	Discovery of by Alexander Graham Bell and the photophone	1880
1880	Piezo-electricity discovery by Curie brothers	Gas concentration detection using photoacoustics	1938
1907	Triode amplifier tube invented	Invention of lasers	1960
1940	F. Firestone uses ultrasound for NDT	Photoacoustic induced elastic waves measured in the eye of a rabbit	1964
1953	Heart motions detected using ultrasound	Michaelson laser interferometer used for vibration detection	1966
1948	Integrated circuits by Jack Kilby	Practical fiber optics and fiber optic hydrophone	1977
1960	First B-mode image with 1 ton diasonograph machine using articulating arms ("Dinasaurograph")	Ex-vivo photoacoustic tissue characterization using 5.655 GHz radar transmitter	1980
1965	Real-time US imaging with mechanical scanners	Optical detection of ultrasound on rough surfaces	1991
1966	First doppler image	*in-vivo* photoacoustic A-scan on a human finger	1993
1971	Linear arrays	Photoacoustic tomography	1990's
1980	Commercial phased arrays	Silicon photonics	2004
1981	HP70020A clinical scanner	Non-contact imaging of chicken chorioallantoic membrane	2012
1986	Titanic found with sonar	Nanophotonic phased array	2013
1990's	Miniaturization and portability	On-chip heterodyne interferometer	2015
2003	Real-time 3D imaging		
2015	Philips Lumify portable imager		
2018	Portable CMUT arrays (Butterfly iQ)		

Table 6.1: Comparison of LUS development to conventional ultrasound

Chapter 7

Conclusion and Future Work

7.1 Conclusion

This thesis presented two distinct methods for non-contact ultrasound: immersion and optical. Immersion ultrasound uses a fixed gantry with water immersion to separate the acoustic transducer from the patient. By providing a fixed gantry, a known reference frame can be established, enabling quantitative imaging methods such as ultrasound tomography (UST) by measuring propagation through the subject of interest. The main challenge in immersion ultrasound is accounting for the presence of bone. Conventional methods for soft-tissue imaging is ill conditioned for bone imaging. In particular, the high impedance mismatch between soft-tissue and bone generates strong specular reflections and gives rise to complex propagation modes. Novel imaging systems and techniques developed in this thesis enables evaluation of new algorithms specific to bone imaging. Echo flow migration (EFM) recovers dynamic range comparable to those of clinical ultrasound systems by distinguishing the direction of arrival of each detected echo. Full waveform inversion (FWI) quantifies speed of sound in soft-tissue and bone by iteratively optimizing a simulated model versus the measured waveforms. Imaging results on simulated, phantom, and tissue data, for both EFM and FWI verifies the feasibility of using ultrasound for imaging and quantification of soft-tissue with bone. The mechanical systems developed in this thesis, enables flexible and iterative development of new algorithms in the immersion

ultrasound framework. New techniques can be cost-effectively developed and tested on real measurement data using the platforms designed in this thesis. The MEDUSA system presented here enables full flexibility in transducer positioning and data acquisition, a unique capability not feasible in ring or conical array systems. Further development of immersion ultrasound will enable repeatable, volumetric, and quantitative imaging of proximal limbs, applicable for prosthetic fitting, muscle monitoring, and bone density tracking.

Given the accelerating advances in photonics, conventional ultrasound will likely incorporate more optical techniques for imaging. Full optical non-contact ultrasound fully eliminates the acoustic coupling medium and patient contact. The laser ultrasound (LUS) technique presented in this thesis builds upon conventional photoacoustics but establishes a different paradigm by specifically limiting the optical to acoustic conversion to the tissue surface rather than penetrating into the tissue. By restricting penetration, the generated acoustic energy is maximized and the spatial location of the acoustic source can be known *a priori*. Not known in penetrating photoacoustics, prior spatial knowledge of the LUS source may enable transmit beamforming in the future with parallelized optical arrays. In combination with optical interferometry, LUS is analogous to conventional ultrasound but is light driven and completely non-contact. This thesis analyzed the mechanism by which LUS sources are generated in biological tissue and identifies the critical design parameters to maximize optical to acoustic conversion efficiency while maintaining eye and skin safety for human imaging. Ideal optical wavelengths were specified for both transmission and detection of ultrasound on biological tissue. A full non-contact LUS system was evaluated on tissue mimicking phantoms, excised animal tissue, and *in-vivo* human subjects. Verified by conventional ultrasound imaging, LUS images confirm that the technique is sensitive to both soft and hard-tissue features in excised animal tissue as well as human subjects. Human LUS images presented in this thesis marks the first instance of *in-vivo* optical ultrasound imaging on a human subject and establishes the feasibility of LUS as an imaging technique and motivates further clinical development.

7.2 Contributions

- **Bone Ultrasound:**

    1. Defined system design and trade-offs for geometric and quantitative ultrasound imaging of bone
    2. Developed and demonstrated adaptive beamforming reconstruction (EFM) method for geometric imaging of tissue with bone
    3. Demonstrated quantitative imagine of tissue with bone using FWI
    4. Designed and built a fully flexible ultrasound tomography system (MEDUSA) for iterative algorithm development on real data

- **Laser Ultrasound:**

    1. Identified critical process parameters and trade-offs for LUS imaging at eye and skin safe optical levels
    2. Elucidated tissue and light interactions to maximize acoustic output in biological tissue
    3. First full non-contact LUS image on humans verifying sensitivity to soft and hard-tissue features
    4. Set technology road map for future LUS development for clinical implementation

7.3 Future Work

7.3.1 Immersion Ultrasound

Further development in the immersion ultrasound framework will refine algorithms and data acquisition techniques necessary for robust, quantitative, and volumetric imaging of human limbs. Clinical application of immersion ultrasound for bone imaging hinges on increasing imaging speed and accurate reconstruction/quantification of

tissue morphology in *in-vivo* human subjects. Imaging techniques presented in this thesis are applicable for human subject imaging. With engineering improvements in the electronics and supporting hardware, MEDUSA has the potential to scan human subjects and evaluate algorithm performance in real human data. Techniques such as adaptive sampling should be evaluated to reduce scan time and tailor data acquisition strategies to specific regions/parameters of interest. Once the necessary imaging technique and algorithm has been informed by MEDUSA for a particular clinical application, specific clinical embodiments of immersion ultrasound systems can be engineered. Depending on the tissue size and parameters of interest (finger, arm, leg), the appropriate design trade-offs can be evaluated following the design method presented in this thesis.

Reflection tomography is of particular interest to the author for tissue imaging with bone. While high reflectivity and attenuation of bone is a significant challenge for acoustic imaging, bone is also an ideal acoustic mirror for reflection tomography. As presented in Chapter 2, reflection tomography using an engineered acoustic mirror has shown promising results with reduced system complexity. Reversing the challenges associated with bone, the bone boundary could be leveraged as an acoustic mirror to quantity soft-tissue properties above the bone boundary. Long bones are easily accessible in humans and could be used to implement reflection tomography with minimal change to existing ultrasound hardware.

7.3.2 Laser Ultrasound

The future of optical based ultrasound is dependent on development of low-cost parallelized optical transmitters and receivers. As discussed in Chapter 6, advances in silicon photonics can be translated to LUS development due to the similarity in optical wavelengths at $\sim$1500 *nm*. With existing technology, surface treatment techniques by infusing retro-reflective particles into flexible hydrogels will likely amplify optical transmission and detection of ultrasound sufficiently for broader acoustic bandwidths and improved optical detection sensitivity. Since retro-reflective particles impede the optical source, specific density of retro-reflective particles within the hydrogel must

be quantified. Design of retro-reflector infused hydrogels must balance conversion of the optical source with reflection of the detection laser; a multi-layer hydrogel where transmission and detection layers are differentiated could be a feasible solution. As mentioned previously, robust 3D spatial tracking of the optical transmission and detection laser must also be implemented for large volume LUS imaging. This thesis establishes the feasibility of LUS as a technique for *in-vivo* human imaging using existing optical systems. Scaling LUS further, custom optical systems should be engineered specifically for LUS imaging.

Bibliography

[1] C. Hansen, N. Hiittebrauker, A. Schasse, W. Wilkening, H. Ermert, M. Hollenhorst, L. Heuser, and G. Schulte-Altedomeburg, "Ultrasound breast imaging using full angle spatial compounding: in-vivo results," *Proceedings - IEEE Ultrasonics Symposium*, pp. 54–57, 2008.

[2] B. Siciliano, *Robotics : modelling, planning and control.* Springer, 2009.

[3] BCC Research Staff, "Medical Imaging: A BCC Research Outlook," Tech. Rep., 2019.

[4] T. L. Szabo, *Diagnostic Ultrasound Imaging: Inside Out*, 2004.

[5] I. Papanicolas, L. R. Woskie, and A. K. Jha, "Health Care Spending in the United States and Other High-Income Countries," *JAMA*, vol. 319, no. 10, p. 1024, mar 2018.

[6] L. Parker, L. N. Nazarian, J. A. Carrino, W. B. Morrison, G. Grimaldi, A. J. Frangos, D. C. Levin, and V. M. Rao, "Musculoskeletal Imaging: Medicare Use, Costs, and Potential for Cost Substitution," *Journal of the American College of Radiology*, vol. 5, no. 3, pp. 182–188, mar 2008.

[7] C. M. Girgis, N. Mokbel, and D. J. DiGirolamo, "Therapies for Musculoskeletal Disease: Can we Treat Two Birds with One Stone?" *Current Osteoporosis Reports*, vol. 12, no. 2, pp. 142–153, jun 2014.

[8] N. J. Bureau and D. Ziegler, "Economics of Musculoskeletal Ultrasound." *Current radiology reports*, vol. 4, no. 8, p. 44, aug 2016.

[9] Society of Diagnostic Medical Sonography, "Industry Standards for the Prevention of Work-Related Musculoskeletal Disorders in Sonography: Consensus Conference on Work-Related Musculoskeletal Disorders in Sonography," *Journal of Diagnostic Medical Sonography*, vol. 27, no. 1, pp. 14–18, jan 2011.

[10] M. W. Gilbertson and B. W. Anthony, "An ergonomic, instrumented ultrasound probe for 6-axis force/torque measurement," *Proceedings of the Annual International Conference of the IEEE Engineering in Medicine and Biology Society, EMBS*, pp. 140–143, 2013.

[11] U.S. Bureau of Labor Statistics, "Diagnostic Medical Sonographers and Cardiovascular Technologists and Technicians, Including Vascular Technologists : Occupational Outlook Handbook: : U.S. Bureau of Labor Statistics."

[12] S. C. Roll, K. D. Evans, C. D. Hutmire, and J. P. Baker, "An analysis of occupational factors related to shoulder discomfort in diagnostic medical sonographers and vascular technologists," *Work*, vol. 42, no. 3, pp. 355–365, jan 2012.

[13] J. P. Baker and C. T. Coffin, "The Importance of an Ergonomic Workstation to Practicing Sonographers," *Journal of Ultrasound in Medicine*, vol. 32, no. 8, pp. 1363–1375, aug 2013.

[14] C. Ismail, J. Zabal, H. J. Hernandez, P. Woletz, H. Manning, C. Teixeira, L. DiPietro, M. R. Blackman, and M. O. Harris-Love, "Diagnostic ultrasound estimates of muscle mass and muscle quality discriminate between women with and without sarcopenia," *Frontiers in Physiology*, vol. 6, no. OCT, pp. 1–10, 2015.

[15] M. O. Harris-Love, R. Monfaredi, C. Ismail, M. R. Blackman, and K. Cleary, "Quantitative Ultrasound: Measurement Considerations for the Assessment of Muscular Dystrophy and Sarcopenia," *Frontiers in Aging Neuroscience*, vol. 6, no. July, pp. 1–4, 2014.

[16] M. O. Harris-Love, C. Ismail, R. Monfaredi, H. J. Hernandez, D. Pennington, P. Woletz, V. McIntosh, B. Adams, and M. R. Blackman, "Interrater reliability of quantitative ultrasound using force feedback among examiners with varied levels of experience," *PeerJ*, vol. 4, p. e2146, 2016.

[17] M. W. Gilbertson, "Electromechanical Systems to Enhance the Usability and Diagnostic Capabilities of Ultrasound Imaging," Ph.D. dissertation, MIT, 2014.

[18] R. Correa-de Araujo, M. O. Harris-Love, I. Miljkovic, M. S. Fragala, B. W. Anthony, and T. M. Manini, "The Need for Standardized Assessment of Muscle Quality in Skeletal Muscle Function Deficit and Other Aging-Related Muscle Dysfunctions: A Symposium Report," *Frontiers in Physiology*, vol. 8, p. 87, feb 2017.

[19] H. Ishida and S. Watanabe, "Influence of Inward Pressure of the Transducer on Lateral Abdominal Muscle Thickness During Ultrasound Imaging," *Journal of Orthopaedic & Sports Physical Therapy*, vol. 42, no. 9, pp. 815–818, 2012.

[20] T. Syversveen, K. Midtvedt, A. E. Berstad, K. Brabrand, E. H. Strøm, and A. Abildgaard, "Tissue elasticity estimated by acoustic radiation force impulse quantification depends on the applied transducer force: an experimental study in kidney transplant patients," *European Radiology*, vol. 22, no. 10, pp. 2130–2137, oct 2012.

[21] A. C. L. Lam, S. W. A. Pang, A. T. Ahuja, and K. S. S. Bhatia, "The influence of precompression on elasticity of thyroid nodules estimated by ultrasound shear wave elastography," *European Radiology*, vol. 26, no. 8, pp. 2845–2852, aug 2016.

[22] L. Porra, H. Swan, and C. Ho, "The effect of applied transducer force on acoustic radiation force impulse quantification within the left lobe of the liver," *Australasian Journal of Ultrasound in Medicine*, vol. 18, no. 3, pp. 100–106, aug 2015.

[23] P. Mirk, N. Magnavita, L. Masini, M. Bazzocchi, and A. Fileni, "Frequency of musculoskeletal symptoms in diagnostic medical sonographers. Results of a pilot survey." *La Radiologia medica*, 1999.

[24] S. A. Zakerian, M. Abbaszadeh, L. Janani, Z. Kazemi, and M. H. Safarain, "The prevalence of musculoskeletal disorders among ultrasound specialists and identifying their work-related risk factors," 2017.

[25] K. Evans, S. Roll, and J. Baker, "Work-Related Musculoskeletal Disorders (WRMSD) Among Registered Diagnostic Medical Sonographers and Vascular Technologists," *Journal of Diagnostic Medical Sonography*, vol. 25, no. 6, pp. 287–299, nov 2009.

[26] S. Y. Sun and B. W. Anthony, "Freehand 3D ultrasound volume imaging using a miniature-mobile 6-DOF camera tracking system," in *Proceedings - International Symposium on Biomedical Imaging*, 2012, pp. 1084–1087.

[27] S.-Y. Sun, B. W. Anthony, and M. W. Gilbertson, "Trajectory-based deformation correction in ultrasound images," *SPIE Medical Imaging*, pp. 76 290A–76 290A–9, 2010.

[28] S. Y. Sun, M. Gilbertson, and B. W. Anthony, "Computer-guided ultrasound probe realignment by optical tracking," in *Proceedings - International Symposium on Biomedical Imaging*, 2013, pp. 21–24.

[29] M. Hollenhorst, C. Hansen, N. Huttebrauker, A. Schasse, L. Heuser, H. Ermert, and G. Schulte-Altedorneburg, "Ultrasound computed tomography in breast imaging: First clinical results of a custom-made scanner," *Ultraschall in der Medizin*, vol. 31, no. 6, pp. 604–609, 2010.

[30] N. Ruiter, R. Stotzka, and T. Müller, "State of the art and challenges in Ultrasound computer tomography," in *pROC: embec*, vol. 11, no. 1, 2005, pp. 3–6.

[31] R. Stotzka, J. Wuerfel, T. O. Mueller, and H. Gemmeke, "Medical imaging by ultrasound computer tomography," in *Proc of SPIE*, vol. 4687, 2002, pp. 110–119.

[32] M. Birk, E. Kretzek, P. Figuli, M. Weber, J. Becker, and N. Ruiter, "High-Speed Medical Imaging in 3D Ultrasound Computer Tomography," *IEEE Transactions on Parallel and Distributed Systems*, vol. PP, no. 99, pp. 1–1, 2015.

[33] H. Gemmeke and N. V. Ruiter, "3D ultrasound computer tomography for medical imaging," *Nuclear Instruments and Methods in Physics Research, Section A: Accelerators, Spectrometers, Detectors and Associated Equipment*, vol. 580, no. 2, pp. 1057–1065, 2007.

[34] R. G. Pratt, L. Huang, N. Duric, and P. Littrup, "Sound-speed and attenuation imaging of breast tissue using waveform tomography of transmission ultrasound data," *Medical Imaging 2007: Physics of Medical Imaging*, vol. 6510, pp. 1–12, 2007.

[35] C. Li, N. Duric, P. Littrup, and L. Huang, "In vivo Breast Sound-Speed Imaging with Ultrasound Tomography," *Ultrasound in Medicine and Biology*, vol. 35, no. 10, pp. 1615–1628, 2009.

[36] N. Duric, P. Littrup, A. Babkin, D. Chambers, S. Azevedo, R. Pevzner, M. Tokarev, E. Holsapple, O. Rama, and R. Duncan, "Development of ultrasound tomography for breast imaging: technical assessment." *Medical physics*, vol. 32, no. 5, pp. 1375–86, 2005.

[37] N. Duric, P. Littrup, L. Poulo, A. Babkin, R. Pevzner, E. Holsapple, O. Rama, and C. Glide, "Detection of breast cancer with ultrasound tomography: first results with the Computed Ultrasound Risk Evaluation (CURE) prototype." *Medical physics*, vol. 34, no. 2, pp. 773–785, 2007.

[38] B. Ranger, P. J. Littrup, N. Duric, P. Chandiwala-Mody, C. Li, S. Schmidt, and J. Lupinacci, "Breast ultrasound tomography versus MRI for clinical display of anatomy and tumor rendering: Preliminary results," *American Journal of Roentgenology*, vol. 198, no. 1, pp. 233–239, 2012.

[39] B. Ranger, P. Littrup, N. Duric, C. Li, S. Schmidt, J. Lupinacci, L. Myc, A. Szczepanski, O. Rama, and L. Bey-Knight, "Breast imaging with ultrasound tomography: a comparative study with MRI," *Proceedings of SPIE*, vol. 7629, pp. 762 906–1–762 906–9, 2010.

[40] T. Hopp, L. Šroba, M. Zapf, R. Dapp, E. Kretzek, H. Gemmeke, and N. V. Ruiter, "Breast Imaging with 3D Ultrasound Computer Tomography: Results of a First In-vivo Study in Comparison to MRI Images." Springer, Cham, 2014, pp. 72–79.

[41] Q. H. Huang, Y. P. Zheng, M. H. Lu, and Z. R. Chi, "Development of a portable 3D ultrasound imaging system for musculoskeletal tissues," *Ultrasonics*, vol. 43, no. 3, pp. 153–163, 2005.

[42] L. He, P. Delzell, and J. Schils, "Comparison of MRI Findings After Musculoskeletal Ultrasound: An Opportunity to Reduce Redundant Imaging," *Journal of the American College of Radiology*, vol. 15, no. 8, pp. 1116–1119, aug 2018.

[43] P. Laugier, B. Fournier, and G. Berger, "Ultrasound parametric imaging of the calcaneus: In vivo results with a new device," *Calcified Tissue International*, vol. 58, no. 5, pp. 326–331, 1996.

[44] P. Laugier, G. Haiat, and G. Haïat, *Bone Quantitative Ultrasound.* Springer, 2011.

[45] P. Laugier, I. Paramétrique, and U. M. R. Cnrs, "Acoustics ' 08 Paris Bones in the light of ultrasound," pp. 1–7, 2008.

[46] T. Douglas, S. Solomonidis, W. Sandham, and W. Spence, "Ultrasound imaging in lower limb prosthetics," *IEEE Transactions on Neural Systems and Rehabilitation Engineering*, vol. 10, no. 1, pp. 11–21, 2002.

[47] B. J. Ranger, "Ultrasonic imaging methods for quantitative musculoskeletal tissue assessment and improved prosthetic interface design," Ph.D. dissertation, Massachusetts Institute of Technology, 2018.

[48] C. Langton, S. Palmer, and R. Porter, "The measurement of broadband ultrasonic attenuation in cancellous bone," *Engineering in medicine*, vol. 13, no. 2, pp. 89–91, 1984.

[49] M. Jaworski, M. Lebiedowski, R. S. Lorenc, and J. Trempe, "Ultrasound bone measurement in pediatric subjects," *Calcified Tissue International*, vol. 56, no. 5, pp. 368–371, 1995.

[50] M. K. H. Malo, J. T??yr??s, J. P. Karjalainen, H. Isaksson, O. Riekkinen, and J. S. Jurvelin, "Ultrasound backscatter measurements of intact human proximal femurs-Relationships of ultrasound parameters with tissue structure and mineral density," *Bone*, vol. 64, pp. 240–245, 2014.

[51] C. C. Gluer, C. Y. Wu, M. Jergas, S. A. Goldstein, and H. K. Genant, "Three quantitative ultrasound parameters reflect bone structure," *Calcified Tissue International*, vol. 55, no. 1, pp. 46–52, 1994.

[52] F. Padilla, F. Jenson, V. Bousson, F. Peyrin, and P. Laugier, "Relationships of trabecular bone structure with quantitative ultrasound parameters: In vitro study on human proximal femur using transmission and backscatter measurements," *Bone*, vol. 42, no. 6, pp. 1193–1202, 2008.

[53] K. a. Wear, S. Nagaraja, M. L. Dreher, and S. L. Gibson, "Relationships of quantitative ultrasound parameters with cancellous bone microstructure in human calcaneus in vitro," *The Journal of the Acoustical Society of America*, vol. 131, no. 2, p. 1605, 2012.

[54] A. J. Foldes, A. Rimon, D. D. Keinan, and M. M. Popovtzer, "Quantitative ultrasound of the tibia: A novel approach for assessment of bone status," *Bone*, vol. 17, no. 4, pp. 363–367, 1995.

[55] Q. Grimal, J. Grondin, S. Guerard, R. Barkmann, K. Engelke, C. C. Gluer, and P. Laugier, "Quantitative ultrasound of cortical bone in the femoral neck predicts femur strength: Results of a pilot study," *Journal of Bone and Mineral Research*, vol. 28, no. 2, pp. 302–312, 2013.

[56] C. F. Njeh, T. Fuerst, E. Diessel, and H. K. Genant, "Is quantitative ultrasound dependent on bone structure? A reflection," *Osteoporosis International*, vol. 12, no. 1, pp. 1–15, 2001.

[57] R. Barkmann, P. Laugier, U. Moser, S. Dencks, M. Klausner, F. Padilla, G. Haiat, M. Heller, and C.-C. Glüer, "In vivo measurements of ultrasound transmission through the human proximal femur." *Ultrasound in medicine & biology*, vol. 34, no. 7, pp. 1186–90, 2008.

[58] P. Laugier, P. Droin, a. M. Laval-Jeantet, and G. Berger, "In vitro assessment of the relationship between acoustic properties and bone mass density of the calcaneus by comparison of ultrasound parametric imaging and quantitative computed tomography." *Bone*, vol. 20, no. 2, pp. 157–65, 1997.

[59] R. Barkmann, P. Laugier, U. Moser, S. Dencks, F. Padilla, G. Haiat, M. Heller, and C. C. Gluer, "A method for the estimation of femoral bone mineral density from variables of ultrasound transmission through the human femur," *Bone*, vol. 40, no. 1, pp. 37–44, 2007.

[60] P. L. Enright, "The six-minute walk test." *Respiratory care*, vol. 48, no. 8, pp. 783–785, 2003.

[61] S. Pillen, I. M. P. Arts, and M. J. Zwarts, "Muscle ultrasound in neuromuscular disorders," *Muscle and Nerve*, vol. 37, no. 6, pp. 679–693, 2008.

[62] A. F. Mak, M. Zhang, and D. A. Boone, "State-of-the-art research in lower-limb prosthetic biomechanics-socket interface: a review." *Journal of rehabilitation research and development*, vol. 38, no. 2, pp. 161–74, jan 2001.

[63] A. K. Topper and G. R. Fernie, "Computer-aided design and computer-aided manufacturing (CAD/CAM) in prosthetics." *Clinical orthopaedics and related research*, no. 256, pp. 39–43, jul 1990.

[64] P. He, K. Xue, Y. Fan, and Y. Wang, "Test of a vertical scan mode in 3-D imaging of residual limbs using ultrasound." *Journal of rehabilitation research and development*, vol. 36, no. 2, pp. 86–93, 1999.

[65] B. J. Ranger, M. Feigin, X. Zhang, A. Mireault, R. Raskar, H. M. Herr, and B. W. Anthony, "3D optical imagery for motion compensation in a limb ultrasound system," in *Medical Imaging 2016: Ultrasonic Imaging and Tomography*, vol. 9790, 2016, p. 97900R.

[66] P. He, K. Xue, and P. Murka, "3-D imaging of residual limbs using ultrasound." *Journal of rehabilitation research and development*, vol. 34, no. 3, pp. 269–278, 1997.

[67] Office of the Surgeon General (US), "Bone Health and Osteoporosis: A Report of the Surgeon General," Office of the Surgeon General (US), Tech. Rep., 2004.

[68] I. Siegel, G. T. Anast, and T. J. Fields, "The determination of fracture healing by measurement of sound velocity across the fracture site." *Surgery, gynecology & obstetrics*, vol. 107, no. 3, pp. 327–32, sep 1958.

[69] K. Bushby, R. Finkel, D. J. Birnkrant, L. E. Case, P. R. Clemens, L. Cripe, A. Kaul, K. Kinnett, C. McDonald, S. Pandya, J. Poysky, F. Shapiro, J. Tomezsko, and C. Constantin, "Diagnosis and management of Duchenne muscular dystrophy, part 1: diagnosis, and pharmacological and psychosocial management," *The Lancet Neurology*, vol. 9, no. 1, pp. 77–93, 2010.

[70] L. Lyamshev, *Radiation acoustics*. CRC Press, 2004, vol. 162, no. 4.

[71] R. C. Waag and R. J. Fedewa, "A ring transducer system for medical ultrasound research," *IEEE Transactions on Ultrasonics, Ferroelectrics, and Frequency Control*, vol. 53, no. 10, pp. 1707–1718, 2006.

[72] M. Birk, M. Zapf, M. Balzer, N. Ruiter, and J. Becker, "A comprehensive comparison of GPU- and FPGA-based acceleration of reflection image reconstruction for 3D ultrasound computer tomography," *Journal of Real-Time Image Processing*, vol. 9, no. 1, pp. 159–170, 2014.

[73] N. V. Ruiter, M. Zapf, T. Hopp, and H. Gemmeke, "Experimental evaluation of noise generated by grating lobes for a sparse 3D ultrasound computer tomography system," *Proc of SPIE*, vol. 8675, pp. 86 750N–86 750N–8, 2013.

[74] B. Ranger, M. Feigin, N. Pestrov, X. Zhang, V. Lempitsky, H. Herr, and B. Anthony, "Motion compensation in a tomographic ultrasound imaging system: Toward volumetric scans of a limb for prosthetic socket design," in *Proceedings of the Annual International Conference of the IEEE Engineering in Medicine and Biology Society, EMBS*, vol. 2015-Novem, 2015.

[75] X. Zhang, J. R. Fincke, and B. W. Anthony, "Single element ultrasonic imaging of limb geometry: an in-vivo study with comparison to MRI," in *Medical Imaging 2016: Ultrasonic Imaging and Tomography*, N. Duric and B. Heyde, Eds., vol. 9790. International Society for Optics and Photonics, apr 2016, p. 97901R.

[76] X. Zhang, J. Fincke, A. Kuzmin, V. Lempitsky, and B. Anthony, "A single element 3D ultrasound tomography system," in *Proceedings of the Annual International Conference of the IEEE Engineering in Medicine and Biology Society, EMBS*, vol. 2015-Novem, 2015, pp. 5541–5544.

[77] J. Canny, "A Computational Approach to Edge Detection," *IEEE Transactions on Pattern Analysis and Machine Intelligence*, vol. PAMI-8, no. 6, pp. 679–698, nov 1986.

[78] R. O. Duda and P. E. Hart, "Use of the Hough transformation to detect lines and curves in pictures," *Communications of the ACM*, vol. 15, no. 1, pp. 11–15, jan 1972.

[79] J. R. Fincke, "Non-contact quantitative imaging of limbs, bone and tissue, using ultrasound tomographic techniques," Ph.D. dissertation, 2018.

[80] B. E. Treeby, J. Jaros, A. P. Rendell, and B. T. Cox, "Modeling nonlinear ultrasound propagation in heterogeneous media with power law absorption using a k-space pseudospectral method," *The Journal of the Acoustical Society of America*, vol. 131, no. 6, pp. 4324–4336, jun 2012.

[81] B. E. Treeby and B. T. Cox, "k-Wave: MATLAB toolbox for the simulation and reconstruction of photoacoustic wave fields," *Journal of Biomedical Optics*, vol. 15, no. 2, p. 021314, 2010.

[82] M. Ackerman, "The Visible Human Project," *Proceedings of the IEEE*, vol. 86, no. 3, pp. 504–511, mar 1998.

[83] S. A. Goss, R. L. Johnston, and F. Dunn, "Compilation of empirical ultrasonic properties of mammalian tissues. II," *The Journal of the Acoustical Society of America*, vol. 68, no. 1, pp. 93–108, jul 1980.

[84] ——, "Comprehensive compilation of empirical ultrasonic properties of mammalian tissues," *The Journal of the Acoustical Society of America*, vol. 64, no. 2, pp. 423–457, aug 1978.

[85] NASA, *Human Integration Design Processes*, 2014.

[86] ——, *Human Integration Design Handbook*, 2014.

[87] U.S. Department of Health and Human Services, "Information for Manufacturers Seeking Marketing Clearance of Diagnostic Ultrasound Systems and Transducers," pp. 1–64, 2008.

[88] A. G. Bell, "On the Production and Reproduction of Sound by Light," Tech. Rep.

[89] S. Manohar and D. Razansky, "Photoacoustics: a historical review," *Advances in Optics and Photonics*, vol. 8, no. 4, p. 586, dec 2016.

[90] M. Xu and L. V. Wang, "Photoacoustic imaging in biomedicine," *Review of Scientific Instruments*, vol. 77, no. 4, pp. 1–22, 2006.

[91] L. V. Wang and J. Yao, "A practical guide to photoacoustic tomography in the life sciences," *Nature Methods*, vol. 13, no. 8, pp. 627–638, 2016.

[92] L. Wang and S. Hu, "Photoacoustic Tomography: in Vivo Imaging From Organelles To Organs," *Science*, vol. 335, no. 6075, pp. 1458–1462, 2012.

[93] B. Cox, J. G. Laufer, S. R. Arridge, and P. C. Beard, "Quantitative spectroscopic photoacoustic imaging: a review," *Journal of Biomedical Optics*, vol. 17, no. 6, p. 061202, 2012.

[94] L. V. Wang, *Photoacoustic imaging and spectroscopy*. CRC, 2009.

[95] A. Taruttis and V. Ntziachristos, "Advances in real-time multispectral optoacoustic imaging and its applications," *Nature Photonics*, vol. 9, no. 4, pp. 219–227, apr 2015.

[96] R. Haupt, C. Wynn, B. Anthony, J. Fincke, A. Samir, and X. Zhang, "Non-contact laser ultrasound concept for biomedical imaging," in *IEEE International Ultrasonics Symposium, IUS*, 2017.

[97] P. Beard, "Biomedical photoacoustic imaging," pp. 602–631, aug 2011.

[98] V. E. V. E. Gusev and A. A. A. A. Karabutov, *Laser optoacoustics*. New York: American Institute of Physics, 1993.

[99] G. Ku and L. V. Wang, "Deeply penetrating photoacoustic tomography in biological tissues enhanced with an optical contrast agent," *Optics Letters*, vol. 30, no. 5, p. 507, mar 2005.

[100] A. P. Jathoul, J. Laufer, O. Ogunlade, B. Treeby, B. Cox, E. Zhang, P. Johnson, A. R. Pizzey, B. Philip, T. Marafioti, M. F. Lythgoe, R. B. Pedley, M. A. Pule, and P. Beard, "Deep in vivo photoacoustic imaging of mammalian tissues using a tyrosinase-based genetic reporter," *Nature Photonics*, vol. 9, no. 4, pp. 239–246, apr 2015.

[101] Y. Hristova, P. Kuchment, and L. Nguyen, "Reconstruction and time reversal in thermoacoustic tomography in acoustically homogeneous and inhomogeneous media," *Inverse Problems*, vol. 24, no. 5, p. 055006, oct 2008.

[102] J. L. Johnson, J. Shragge, and K. van Wijk, "Image reconstruction of multichannel photoacoustic and laser-ultrasound data using reverse time migration," *SPIE BiOS*, vol. 9323, no. 0, pp. 932 314–932 320, 2015.

[103] ——, "Nonconfocal all-optical laser-ultrasound and photoacoustic imaging system for angle-dependent deep tissue imaging," *Journal of Biomedical Optics*, vol. 22, no. 4, p. 041014, 2017.

[104] J. L. Johnson, K. van Wijk, and M. Sabick, "Characterizing Phantom Arteries with Multi-channel Laser Ultrasonics and Photo-acoustics," *Ultrasound in Medicine and Biology*, vol. 40, no. 3, pp. 513–520, 2014.

[105] G. Paltauf, R. Nuster, M. Haltmeier, and P. Burgholzer, "Photoacoustic tomography using a Mach-Zehnder interferometer as an acoustic line detector," *Applied Optics*, vol. 46, no. 16, p. 3352, 2007.

[106] T. Stratoudaki, M. Clark, and P. D. Wilcox, "Adapting the full matrix capture and the total focusing method to laser ultrasonics for remote non destructive testing," *IEEE International Ultrasonics Symposium, IUS*, pp. 3–6, 2017.

[107] J. P. Monchalin, "Optical detection of ultrasound." *IEEE transactions on ultrasonics, ferroelectrics, and frequency control*, vol. 33, no. 5, pp. 485–499, 1986.

[108] E. Zhang, J. Laufer, and P. Beard, "Backward-mode multiwavelength photoacoustic scanner using a planar Fabry-Perot polymer film ultrasound sensor for high-resolution three-dimensional imaging of biological tissues," *Applied Optics*, vol. 47, no. 4, p. 561, 2008.

[109] B. Dong, H. Li, Z. Zhang, K. Zhang, S. Chen, C. Sun, and H. F. Zhang, "Isometric multimodal photoacoustic microscopy based on optically transparent micro-ring ultrasonic detection," *Optica*, vol. 2, no. 2, p. 169, feb 2015.

[110] S. J. Park, J. Eom, Y. H. Kim, C. S. Lee, and B. H. Lee, "Noncontact photoacoustic imaging based on all-fiber heterodyne interferometer." *Optics letters*, vol. 39, no. 16, pp. 4903–6, 2014.

[111] G. Rousseau, A. Blouin, and J.-P. Monchalin, "Non-contact photoacoustic tomography and ultrasonography for tissue imaging." *Biomedical optics express*, vol. 3, no. 1, pp. 16–25, jan 2012.

[112] A. Hochreiner, J. Bauer-Marschallinger, P. Burgholzer, B. Jakoby, and T. Berer, "Non-contact photoacoustic imaging using a fiber based interferometer with optical amplification." *Biomedical optics express*, vol. 4, no. 11, pp. 2322–31, nov 2013.

[113] G. Wissmeyer, D. Soliman, R. Shnaiderman, A. Rosenthal, and V. Ntziachristos, "All-optical optoacoustic microscope based on wideband pulse interferometry," *Optics Letters*, vol. 41, no. 9, p. 1953, may 2016.

[114] S. Ashkenazi, Y. Hou, T. Buma, and M. O'Donnell, "Optoacoustic imaging using thin polymer etalon," *Applied Physics Letters*, vol. 86, no. 13, pp. 1–3, 2005.

[115] A. R. A. R. Henderson and K. Schulmeister, *Laser Safety*, 2nd ed. London: Chapman & Hall, 2008.

[116] S. L. Jacques, "Optical properties of biological tissues: a review." *Physics in medicine and biology*, vol. 58, no. 11, pp. R37–61, 2013.

[117] T. L. Troy and S. N. Thennadil, "Optical properties of human skin in the near infrared wavelength range of 1000 to 2200 nm," *Journal of Biomedical Optics*, vol. 6, no. 2, p. 167, 2001.

[118] American National Standards Institute., Laser Institute of America., and American National Standards Institute., *American National Standard for Safe Use of Lasers*, 2007, vol. Z136.1.

[119] F. A. Duck, *Physical properties of tissue : a comprehensive reference book.* Academic Press, 1990.

[120] D. Shore, M. Woods, and C. Miles, "Attenuation of ultrasound in post rigor bovine skeletal muscle," *Ultrasonics*, vol. 24, no. 2, pp. 81–87, mar 1986.

[121] C. C. Cooksey, B. K. Tsai, and D. W. Allen, "A collection and statistical analysis of skin reflectance signatures for inherent variability over the 250 nm to 2500 nm spectral range," vol. 9082, p. 908206, 2014.

[122] C. C. Cooksey and D. W. Allen, "Reflectance measurements of human skin from the ultraviolet to the shortwave infrared (250 nm to 2500 nm)," vol. 8734, p. 87340N, 2013.

[123] S. Doctor, T. Hall, and L. Reid, "SAFT âĂŤ the evolution of a signal processing technology for ultrasonic testing," *NDT International*, vol. 19, no. 3, pp. 163–167, jun 1986.

[124] J. Opretzka, M. Vogt, and H. Ermert, "A high-frequency ultrasound imaging system combining limited-angle spatial compounding and model-based synthetic aperture focusing," *IEEE Transactions on Ultrasonics, Ferroelectrics and Frequency Control*, vol. 58, no. 7, pp. 1355–1365, jul 2011.

[125] K. Hollman, K. Rigby, and M. O'Donnell, "Coherence factor of speckle from a multi-row probe," in *1999 IEEE Ultrasonics Symposium. Proceedings. International Symposium (Cat. No.99CH37027)*, vol. 2. IEEE, pp. 1257–1260.

[126] M. A. Lediju Bell, N. Kuo, D. Y. Song, and E. M. Boctor, "Short-lag spatial coherence beamforming of photoacoustic images for enhanced visualization of prostate brachytherapy seeds," *Biomedical Optics Express*, vol. 4, no. 10, p. 1964, oct 2013.

[127] C.-K. Liao, M.-L. Li, and P.-C. Li, "Optoacoustic imaging with synthetic aperture focusing and coherence weighting," *Optics Letters*, vol. 29, no. 21, p. 2506, nov 2004.

[128] R. Mallart and M. Fink, "Adaptive focusing in scattering media through soundâĂŘspeed inhomogeneities: The van Cittert Zernike approach and focusing criterion," *The Journal of the Acoustical Society of America*, vol. 96, no. 6, pp. 3721–3732, dec 1994.

[129] J. L. Johnson, M. Merrilees, J. Shragge, and K. van Wijk, "All-optical extravascular laser-ultrasound and photoacoustic imaging of calcified atherosclerotic plaque in excised carotid artery," *Photoacoustics*, vol. 9, pp. 62–72, mar 2018.

[130] J. R. Fincke, C. M. Wynn, R. Haupt, X. Zhang, D. Rivera, and B. Anthony, "Characterization of laser ultrasound source signals in biological tissues for imaging applications," *Journal of Biomedical Optics*, vol. 24, no. 02, p. 1, 2018.

[131] A. Brożyna, K. Wasilewska, K. Węsierska, and B. W. Chwirot, "Porcine Skin as a Model System for Studies of Adverse Effects of Narrow-Band UVB Pulses on Human Skin," *Journal of Toxicology and Environmental Health, Part A*, vol. 72, no. 13, pp. 789–795, jun 2009.

[132] A. Summerfield and M. E. Ricklin, "The immunology of the porcine skin and its value as a model for human skin," *Molecular Immunology*, vol. 66, no. 1, pp. 14–21, jul 2015.

[133] R. Kong and R. Bhargava, "Characterization of porcine skin as a model for human skin studies using infrared spectroscopic imaging," *The Analyst*, vol. 136, no. 11, p. 2359, may 2011.

[134] J.-Y. Sun, X. Zhao, W. R. K. Illeperuma, O. Chaudhuri, K. H. Oh, D. J. Mooney, J. J. Vlassak, and Z. Suo, "Highly stretchable and tough hydrogels," *Nature*, vol. 489, no. 7414, pp. 133–136, sep 2012.

[135] A. Taruttis, G. M. van Dam, and V. Ntziachristos, "Mesoscopic and Macroscopic Optoacoustic Imaging of Cancer," *Cancer Research*, vol. 75, no. 8, pp. 1548–1559, apr 2015.

[136] "PA in liquids Review Lyamshev 1981.pdf."

[137] J. Sun, E. Timurdogan, A. Yaacobi, E. S. Hosseini, and M. R. Watts, "Large-scale nanophotonic phased array," *Nature*, vol. 493, no. 7431, pp. 195–199, jan 2013.

[138] Jie Sun, E. Timurdogan, A. Yaacobi, Zhan Su, E. S. Hosseini, D. B. Cole, and M. R. Watts, "Large-Scale Silicon Photonic Circuits for Optical Phased Arrays," *IEEE Journal of Selected Topics in Quantum Electronics*, vol. 20, no. 4, pp. 264–278, jul 2014.

[139] D. B. Cole, C. Sorace-Agaskar, M. Moresco, G. Leake, D. Coolbaugh, and M. R. Watts, "Integrated heterodyne interferometer with on-chip modulators and detectors," *Optics Letters*, vol. 40, no. 13, p. 3097, jul 2015.

[140] J. D. B. Bradley, E. S. Hosseini, Purnawirman, Z. Su, T. N. Adam, G. Leake, D. Coolbaugh, and M. R. Watts, "Monolithic erbium- and ytterbium-doped microring lasers on silicon chips," *Optics Express*, vol. 22, no. 10, p. 12226, may 2014.

[141] C. T. DeRose, R. D. Kekatpure, D. C. Trotter, A. Starbuck, J. R. Wendt, A. Yaacobi, M. R. Watts, U. Chettiar, N. Engheta, and P. S. Davids, "Electronically controlled optical beam-steering by an active phased array of metallic nanoantennas," *Optics Express*, vol. 21, no. 4, p. 5198, feb 2013.

[142] C. V. Poulton, A. Yaacobi, D. B. Cole, M. J. Byrd, M. Raval, D. Vermeulen, and M. R. Watts, "Coherent solid-state LIDAR with silicon photonic optical phased arrays," *Optics Letters*, vol. 42, no. 20, p. 4091, oct 2017.